



This is to certify that the

dissertation entitled

Crossflow Permeation of Viscous and
Viscoelastic Liquids Through Arrays of
Circular Cylinders
presented by

Craig A. Chmielewski

has been accepted towards fulfillment of the requirements for

Ph.D.	degree in	CHE
	acgree m	

Date 11/18/91

0-12771

LIBRARY Michigan State University

PLACE IN RETURN BOX to remove this checkout from your record. TO AVOID FINES return on or before date due.

DATE DUE	DATE DUE	DATE DUE

MSU Is An Affirmative Action/Equal Opportunity Institution ctcirc/datedus.pm3-p.

CROSSFLOW PERMEATION OF VISCOUS AND VISCOELASTIC LIQUIDS THROUGH ARRAYS OF CIRCULAR CYLINDERS

by

Craig A. Chmielewski

A DISSERTATION

Submitted to
Michigan State University
in partial fulfillment of the requirements
for the degree of

DOCTOR OF PHILOSOPHY

Department of Chemical Engineering

ABSTRACT

CROSSFLOW PERMEATION OF VISCOUS AND VISCOELASTIC LIQUIDS THROUGH ARRAYS OF CIRCULAR CYLINDERS

By

Craig A. Chmielewski

The flow of viscous and viscoelastic liquids transverse to periodic arrays of circular cylinders is studied. Two array geometries, square and hexagonal, are examined; each having a void fraction of 70 percent. Particular attention is devoted to the influence of macromolecular conformation on the enhanced pressure drop across the arrays. The flow kinematics in both arrays is elucidated by laser Doppler velocimetry and streak photography. These techniques reveal a flow transition from steady to unsteady motion at Deborah numbers corresponding to the onset of enhanced pressure drop. This result indicates that any attempt to predict the relative flow resistance increases observed with the viscoelastic fluids must describe the transition to unsteady flow.

The elastic fluids consist of four polyisobutylene (PIB) solutions; three non-shear thinning and one shear thinning. The non-shear thinning liquids are 0.2 wt. % PIB in polybutene solutions which differ only by the molecular weight of the solute. As these solutions are θ -systems, the square of the degree of polymer extensibility associated with

each of these solutions is proportional to their molecular weight. This is consistent with extensional viscosity measurements made by fiber spinning.

The initial departure from Darcy's law for the non-shear thinning solutions is an enhancement in flow resistance and occurs at Deborah numbers of 0.80 and 0.35 for the square and hexagonal arrays respectively. These onset values are independent of molecular weight. At a given Deborah number above the onset, the flow resistance is greater for higher molecular weights. Even after rescaling to obtain the same onset Deborah number for the two arrays, the relative flow resistance is higher for the hexagonal array than the square array. At large values of Deborah number the relative flow resistances in both arrays become independent of Deborah number. These asymptotic values are shown to be proportional to the molecular weight and hence to the square of the polymer extensibilities for these θ -systems.

The initial departure from Darcy's law for the shear thinning solution is a decrease in the relative flow resistance followed by an increase. This increase occurs at Deborah numbers of 4.2 and 3.0 for the square and hexagonal array respectively.

To my wife, Stephanie, with whose love and patience has made this all possible.

ACKNOWLEDGMENTS

I wish to extend special thanks to my thesis advisor, Dr. Krishnamurthy Jayaraman, for his guidance and friendship throughout my graduate study. I also would like to thank Dr. Charles A. Petty who always seemed available for an intellectual discussion. I would like to thank the other members of my committee as well, for their time and assistance: Dr. Lawrence T. Drzal, Dr. Dahsin Liu and Dr. David Yen. Further thanks need to be extended the Department of Chemical Engineering, the Composite Materials and Structures Center and the State of Michigan without whose financial support this study could not have been undertaken.

I also need to acknowledge those who have provided special assistance to specific portions of this study. These people include Drs. John Foss and Syed Ali for their technical and equipment support during the LDV studies, and Mike Rich and Brian Rook of the CMSC laboratory for their support with the composite processing equipment. Also, I would like to thank Terry Casey and Mike McLean of the D.E.R. machine shop for their assistance in the construction of the permeation cells.

Finally, I would like to thank the many friends I have made over the last few years who have made my stay at MSU so wonderful, especially Steve Reiken, Greg Kudlac, Venkatesh Rao, Brent Larson, Nancy Losure, Kevin Nichols, Mike Bly, Shri Iyer and Javad Kalantar.

TABLE OF CONTENTS

		Page
LIST OF T	'ABLES	ix
LIST OF F	IGURES	x
NOMENCI	LATURE	xvi
Chapter		
1.	INTRODUCTION	1
	1.1 Motivation	1
	1.2 Newtonian liquid flow in porous media	4
	1.3 Non-Newtonian flow in random media	6
	1.4 Corrugated tube models	7
	1.5 Planar elongation	9
	1.6 Dissertation outline	11
2.	THE EFFECT OF POLYMER EXTENSIBILITY	
	ON THE FLOW OF POLYMER SOLUTIONS	
	THROUGH CYLINDER ARRAYS	13
	2.1 Summary	13
	2.2 Introduction	14
	2.3 Experimental	16
	2.3.1 Materials	16
	2.3.2 Shear flow properties	18
	2.4 Fiber spinning	24
	2.4.1 Extensional flow apparatus	24
	2.4.2 Extensional flow results and discussion .	28
	2.5 Crossflow through cylinder arrays	35
	2.5.1 Permeation apparatus	35
	2.5.2 Flow unsteadiness	38

		Page
	2.5.3 Polymer degradation	44
	2.5.4 Permeation of Newtonian fluids	44
	2.5.5 Permeation of viscoelastic liquids	47
	2.6 Conclusions	56
3.	THE KINEMATICS OF VISCOUS AND	
	VISCOELASTIC LIQUID FLOWS WITHIN	
	ARRAYS OF CIRCULAR CYLINDERS	57
	3.1 Summary	57
	3.2 Introduction •	58
	3.3 Laser Doppler velocimetry	61
	3.3.1 Basic principles	61
	3.3.2 Experimental LDV system	67
	3.3.3 LDV measurement difficulties	69
	3.4 Experimental	71
	3.4.1 Test fluids	71
	3.4.2 Apparatus	71
	3.4.3 Streak photography	74
	3.5 Validation of experimental technique	75
	3.5.1 Stokes flow simulation	75 75
	3.5.2 Newtonian liquid flow visualization	75 75
	3.5.3 Newtonian liquid LDV measurements	73 78
	•	78 78
	3.6 Elasite liquid results and discussion	
	3.6.1 Flow visualization on the PIB/PB liquid	78
	3.6.2 LDV measurements on the PIB/PB liquid	89
	3.6.3 LDV measurements on the PIB/decalin liquid	92
	3.6.4 Discussion of flow unsteadiness	96
	3.7 Conclusions •	99
4.	THE DEGRADATION OF POLYMER	
	SOLUTIONS FLOWING THROUGH	
	ARRAYS OF CIRCULAR CYLINDERS	102
	4.1 Summary	102
	4.2 Introduction	103
	4.3 Experimental	106
	4.3.1 Materials •	106
	4.3.2 Rheological properties • · · · · · · · · · · ·	108
	4.3.3 Apparatus •	111
	4.3.4 Wall and end effects	113
	4.4 Results and discussion	

		Page
	4.4.1 Transverse permeability of Newtonian liquid	115
	4.4.2 Departure from Darcy's law for elastic liquids	117
	4.4.3 Degradation of elastic liquids	121
	4.4.4 Analysis of chain extension in arrays	125
	4.4.5 Chain extension modeling	130
	4.5 Conclusions	134
_		
5.	VISCOSITY EFFECTS IN THE	
	PROCESSING OF COMPOSITE	
	PREPREG BY HOT MELT IMPREGNATION	136
	5.1 Summary	136
	5.2 Introduction	
	5.3 Experimental	141
	5.4 Resin and mass fraction and distribution	
	5.5 Mathematical modeling	144
	5.5.1 Tow consolidation models	144
	5.5.2 Impregnation model	149
	5.5.3 Solution procedure	156
	5.6 Calculation results and discussion	158
	5.7 Conclusions	166
6.	CONCLUSIONS AND RECOMMENDATIONS	168
0.	CONCLUSIONS AND RECOMMENDATIONS	100
	6.1 Conclusions	168
	6.2 Recommendations	172
APPENDIX		174
A.	WEDGE DIE/FIBER IMPREGNATION	
	FORTRAN PROGRAM	174
	A.1 Flowchart	174
	A.2 Subprogram summary	
	A.3 Program	
		200
LIST OF RE	FERENCES	200

LIST OF TABLES

		Page
Table 2.1	Properties of the test fluids at 20 °C	17
Table 2.2	Operating parameters in fiber spinning experiments	29
Table 3.1	Components of the laser Doppler velocimetry system shown in Figure 3.1	63
Table 4.1	Properties of the fresh test fluids	109
Table 4.2	Properties of elastic liquids before and after crossflow runs in different arrays	123

LIST OF FIGURES

Figure		Page
1.1	The evolution of the viscosity and relaxation time of a 5 minute epoxy resin curing at room temperature	3
1.2	The relative extensional viscosity versus De of a FENE dumbbell liquid in a steady planar extensional flow	10
2.1 (a)	Steady shear viscosity of the PIB in PB solutions	20
2.1 (b)	Steady shear viscosity of the PIB in decalin solution	21
2.2 (a)	Relative viscosities of the PIB in PB solutions as a function of solution concentration.	22
2.2 (b)	Intrinsic viscosities of the PIB in PB solutions	23
2.3 (a)	Dynamic storage moduli of the PIB in PB solutions	25
2.3 (b)	Dynamic moduli of the PIB in decalin solution	26
2.4	Schematic of fiber spinning apparatus	27
2.5 (a)	Transient extensional viscosities as measured by fiber spinning for the PIB in PB solutions	32
2.5 (b)	Apparent Trouton ratios, accounting for the polymer contribution, based on fiber spinning measurements taken at $\dot{\epsilon} \sim 15 \text{ s}^{-1}$ for the PIB in PB solutions	33
2.6	Apparent Trouton ratios based on fiber spinning data of the PIB in decalin solution where the vlues of η are determined at $\dot{\gamma} = \sqrt{3} \dot{\epsilon}$	36
2.7	Schematic of the permeation apparatus.	37

Figure	·	Page
2.8	Schematic of the permeation cells (all dimensions in cm)	39
2.9	Geometry of the circular cylinders (radius = 0.238 cm) (a) square pitch (b) hexagonal pitch	40
2.10 (a)	Pressure traces for the 2.11 x 10 ⁶ molecular weight PIB/PB solution in the hexagonal array at De = 2.6 (Q = 81 cm ³ /s, upstream P = 29.2 x 10 ⁴ Pa, downstream P = 1.1 x 10 ⁴ Pa)	42
2.10 (b)	Pressure traces for the 2.11 x 10 ⁶ molecular weight PIB/PB solution in the square array at De = 2.6 (Q = 113 cm ³ /s, upstream P = 17.8 x 10 ⁴ Pa, downstream P = 1.7 x 10 ⁴ Pa)	43
2.11	Friction factor vs. Reynolds number of two Newtonian PB liquids compared to the theoretical prediction of Sangani and Acrivos (1982) in square and hexagonal arrays (closed symbols represent the higher molecular weight PB)	46
2.12 (a)	Friction factor vs. Reynolds number of the PIB in PB solutions flowing through the square array	48
2.12 (b)	Friction factor vs. Reynolds number of the PIB in PB solutions flowing through the hexagonal array	49
2.13 (a)	Flow resistance vs. Deborah number for the PIB in PB solutions flowing through the square array	50
2.13 (b)	Flow resistance vs. Deborah number for the PIB in PB solutions flowing through the hexagonal array.	51
2.14	The high Deborah number flow resistance asymptotes as a function of molecular weight for both the square and hexagonal pitch arrays.	53
2.15	Flow resistance vs. Deborah number for the PIB in decalin solution flowing through both the square and hexagonal array.	55

Figure		Page
3.1	Schematic of laser Doppler velocimeter system (components are identified in Table 3.1)	62
3.2	Measuring volume and fringe pattern formed by the beam intersection. The beams intersect in the x-z plane and the z axis follows the bisector of the angle of beam crossing (Dabir, 1983)	65
3.3	A typical signal from the photomultiplier (Dabir, 1983)	66
3.4	Steady shear viscosity of a 0.25 % PIB/PB solution at 25 °C	. 72
3.5	Linear viscoelastic properties of a 0.25 % PIB/PB solution at 25 °C	. 73
3.6	Geometric domains used for the Stokes flow simulations (a) square array and (b) hexagonal array	76
3.7	Streamline output from the Stokes flow simulations (a) square array and (b) hexagonal array	77
3.8	Streak photographs for a Newtonian polybutene liquid in the cylinder arrays at a void fraction of 70 percent (flow from right to left) (a) square array, Re = 0.027 and (b) hexagonal array, Re = 0.013	79
3.9 (a)	LDV measurements and the Stokes flow prediction for the inelastic Newtonian fluid in the square array along y = 1.62	. 80
3.9 (b)	LDV measurements and the Stokes flow prediction for the inelastic Newtonian fluid in the hexagonal array along y = 1.74	. 81
3.10	Streak photographs for the viscoelastic liquid in the square array having a void fraction of 70 percent (flow from right to left) (a) Re = 0.039, De = 0.16 (b) Re = 0.19, De = 0.80.	. 83
3.10 (c)	Re = 0.25, De = 1.09 (d) Re = 0.36, De = 1.44	84
	AT TIEVE ALVE TO AT VICTOR ALTER A	

Figure		Page
3.10 (e)	Re = 0.48, De = 1.91 (f) Re = 0.48, De = 1.91	85
3.11	Streak photographs for the viscoelastic liquid in the hexagonal array having a void fraction of 70 percent (flow from right to left) (a) Re = 0.015, De = 0.059 (b) Re = 0.069, De = 0.28	86
	3.11 (c)Re = 0.11, De = 0.43 (d) Re = 0.14, De = 0.56	87
3.12	Relative flow resistance of a 0.25 % PIB/PB elastic liquid in both square and hexagonal cylinder arrays	88
3.13 (a)	LDV measurements and the Stokes flow prediction for the 0.25 % PIB/PB elastic liquid in the square array along y = 1.62	90
3.13 (b)	LDV measurements and the Stokes flow prediction for the 0.25 % PIB/PB elastic liquid in the hexagonal array along y = 1.74	91
3.14	Probability distribution function of the elastic fluid's velocities measured in the hexagonal array at $x = -1.58$ and $y = 1.74$ (a) De = 0.085 (b) De = 0.36	93
3.15 (a)	LDV measurements and the Stokes flow prediction for the PIB/Decalin liquid in the square array along $y = 1.62$	94
3.15 (b)	LDV measurements and the Stokes flow prediction for the PIB/Decalin liquid in the hexagonal array along $y = 1.74$	95
3.16	Growth of the flow instability in the hexagonal array for the 0.25 % PIB/PB elastic liquid as measured by LDV at x = -1.58 and y = 1.74	100
4.1	Steady shear viscosity of the fresh test fluids	107
4.2	Dynamic moduli and steady shear viscosity of the fresh M1 fluid	110
4.3	(A) Schematic of experimental apparatus and (B) a cross-sectional view of the permeability cell (all dimensions are in centimeters)	112

Figure		Page
4.4	Cylinder array geometries: (A) rectangular pitch array; (B) triangular pitch array (radius = 0.159 cm and porosity = 0.704).	. 114
4.5	Mean pressure gradient vs. superficial velocity for the Newtonian fluid.	. 116
4.6	Friction factor vs. Reynolds number for the M1 fluid flowing through the triangular pitch array.	. 119
4.7	Friction factor vs. Reynolds number for the M1 fluid flowing through the rectangular pitch array.	. 120
4.8	Flow resistance of the M1 fluid relative to the Newtonian value vs. Deborah number	. 122
4.9	Streamlines computed by finite element simulation of Stokes flow through (A) the rectangular pitch array and (B) the triangular pitch array (i and ii denote selected streamline segments)	. 126
4.10	Velocity profiles along selected streamline segments (see Figure 4.9)	. 128
4.11	Strain rate profiles along selected streamline segments (see Figure 4.9)	. 129
4.12	Computed stretch ratio of a polymer chain along selected streamline segments: De = 0.4	. 131
4.13	Computed stretch ratio of a polymer chain along selected streamline segments: De = 1.0	. 132
5.1	Hot melt impregnation (a) schematic of the hot melt prepregger (b) schematic of the resin pot.	. 138
5.2	Resin mass fraction dependence on tow velocity and resin viscosity.	. 140

Figure		Page
5.3	Two 12k AS4 carbon fiber tows impregnated with a DGEBA/mPDA epoxy resin system under the following processing conditions: tow velocity = 18.3 cm/s (a) resin viscosity = 4.5 Pa·s (b) resin viscosity = 0.1 Pa·s.	143
5.4	An illustration of the straightening of a portion of a bent fiber isolated from a network of fibers; (a) the buckled portion of fiber under consideration in an unstressed fiber network; (b) as the fiber network is placed under tension, the fiber portion of interest takes up some of the load; (c) the result is that the fiber straightens.	. 147
5.5	Model non-linear tow consolidation behavior as a result of	
	tension on the fiber tow	. 148
5.6	Wedge die geometry.	. 150
5.7	(a) Calculated pressure profiles for several different values of the effective tensile modulus	. 159
5.7	(b) Calculated impregnation profiles for several different values of the effective tensile modulus	. 161
5.7	(c) Calculated flow rate profiles for several different values of the effective tensile modulus	. 163
5.8	(a) Calculated resin distribution in a model fiber tow	. 164
5.8	(b) Calculated resin mass fraction of a model fiber tow	. 165
5.9	Relationship between the partially impregnated resin tow tensile modulus and the resin viscosity	. 167
A.1	Schematic of the computer algorithm.	. 174

NOMENCLATURE

cylinder radius a Mark-Houwink exponent ā beam width b concentration C fringe spacing d, rate of deformation tensor D diameter D Deborah number De Deborah number defined with the packing number De* $\mathbf{D}_{\mathbf{r}}$ draw ratio beam modulus $\mathbf{E}_{\mathbf{B}}$ friction factor, focal length f force law for the FENE dumbbell f(R) applied force on beam $\mathbf{F}_{\mathbf{B}}$ F_{r} fiber tension superficial mass flux G_o

storage modulus

G'

G'' loss modulus

h_B beam width

H die shape

H_e coating thickness

k Kozeny constant

K permeability tensor

 K_{11}, K_{22}, K_{33} diagonal components of the permeability tensor

K_T transverse permeability

K' Mark-Houwink pre-exponential factor

1 cylinder array length

l_B beam length

L extensibility parameter, die length

L_{FS} liquid fiber length

M, viscosity averaged molecular weight

M_w weight averaged molecular weight

N cycles per burst

N_{Ca} Capillary number

p_a atmospheric pressure

P pressure

P_e compressive load

Q flow rate

r_f fiber radius

r,R	end-to-end distance of a polymer molecule
Re	Reynolds number
S ₁	impregnation front
82	fiber tow profile
S	effective impregnation
t	time
T	temperature
T _{rr}	rr-component of the total stress tensor
T _{zz}	zz-component of the total stress tensor
$\mathbf{u}_{\mathbf{D}}$	normal velocity component into the fiber tow
\mathbf{U}_{ullet}	fiber tow velocity
u,v	velocity
u,v V _o ,v _o	velocity superficial velocity
	•
V₀,V₀	superficial velocity
V _o ,V _o V _x	superficial velocity x-component of the velocity
V _o ,V _o V _x V _y	superficial velocity x-component of the velocity y-component of the velocity
V₀,V₀ V V V V V V V A	superficial velocity x-component of the velocity y-component of the velocity available fiber volume fraction
V _o ,V _o V _x V _y V _a V _f	x-component of the velocity y-component of the velocity available fiber volume fraction fiber volume fraction
V _o ,V _o V _x V _y V _a V _f V _{min}	superficial velocity x-component of the velocity y-component of the velocity available fiber volume fraction fiber volume fraction fiber volume fraction based on the entire die cross-sectional area
V _o ,V _o V _x V _y V _a V _f V _{min}	x-component of the velocity y-component of the velocity available fiber volume fraction fiber volume fraction fiber volume fraction based on the entire die cross-sectional area initial fiber volume fraction

y	y coordinate direction
z	z coordinate direction
	Greek Symbols
α	packing factor
Ϋ	shear rate
Υnf	resin-fiber surface tension
r	capillary pressure
£	void fraction
• €	extension rate
€B	beam strain
η	shear viscosity
η。	zero shear viscosity
$\eta_{ extsf{B}}$	extensional viscosity
${\eta_{\mathtt{B}}}^{+}$	transient extensional viscosity
$\eta_{ extsf{E}}$	average extensional viscosity
η_{s}	relative viscosity
η.	solvent shear viscosity
[η]。	intrinsic viscosity
θ	die half angle
K	half angle of laser beam crossing
K _e	spring constant (compressive loads)
κ _T	spring constant (tensile loads)

 κ_{T}

λ	laser light wavelength
λ_1	relaxation time
$ u_{\mathrm{D}}$	Doppler frequency
ν,	shift frequency
ρ	density
τ	stress
$ au_{ extsf{o}}$	characteristic stress
φ	contact angle
ω	frequency
	Special
<**>	signifies averaging of **
x*	superscript asterisk signifies x is a dimensional quantity
X.,	subscript zero signifies x is an inlet value

Chapter 1

INTRODUCTION

1.1 Motivation

The flow of rheologically complex fluids in random porous media has long been of interest to the oil industry for use in oil recovery processes. With conventional recovery methods, a large amount of oil often remains in the ground after regular production ceases, requiring other innovative techniques to extract the residual oil. These ancillary techniques fall under the heading of "tertiary oil recovery". Tertiary oil recovery processes typically involve pumping dilute polymer solutions in wells to displace inaccessible oil from porous rock. Small amounts of high molecular weight polymers are added to increase the viscosity of the displacing fluid and prevent viscous fingering during permeation. However, the fluid rheology becomes complex, complicating the recovery process at high permeation rates.

The material processing industry also has generated a need to understand the flow of viscous and viscoelastic liquids through porous media, such as fiber mats, in order to produce lower cost and higher quality composite materials. Traditionally, the challenge had been to wet out bundles of ten to twenty micron fibers with viscous epoxy resins.

More recently this problem has been expanded to wetting out fiber bundles with viscoelastic fluids. The complex rheology of high molecular weight materials and fast curing epoxy resins complicate composite manufacturing processes by introducing elastic effects. The magnitude of these effects may vary, and can be quantified by a dimensionless group named the Deborah number, De; the ratio of the characteristic fluid time scale to the flow or processing time scale. For example, impregnation and consolidation flows of rubber modified resins and thermoplastics, having time constants in the range of 0.1 to 10 seconds, achieve Deborah numbers of order one as they flow past 10 micron fibers at velocities as slow as 0.0001 to 0.01 cm/s.

Continued growth in the use of rapidly curing thermosetting systems for liquid molding operations also provides impetus for studying viscoelastic fluid effects in composite processes. Figure 1.1 shows the time evolution of the viscosity and relaxation time of a 5 minute epoxy, undergoing a thermosetting reaction at room temperature. The initial magnitude of the relaxation time is relatively low, but quickly develops so that over the last 50 percent of the epoxy's fluid life the liquid is considerably elastic. This sort of rheological complexity affects the time and pressures needed to ensure the complete saturation of a fiber preform.

Thus, complex fluid rheology must be accounted for in order to obtain a basic understanding of the flow of high molecular weight (or growing molecular weight) materials in porous media. This is particularly a concern to the composite industry, where the ability to move these advanced materials into high volume commercial use

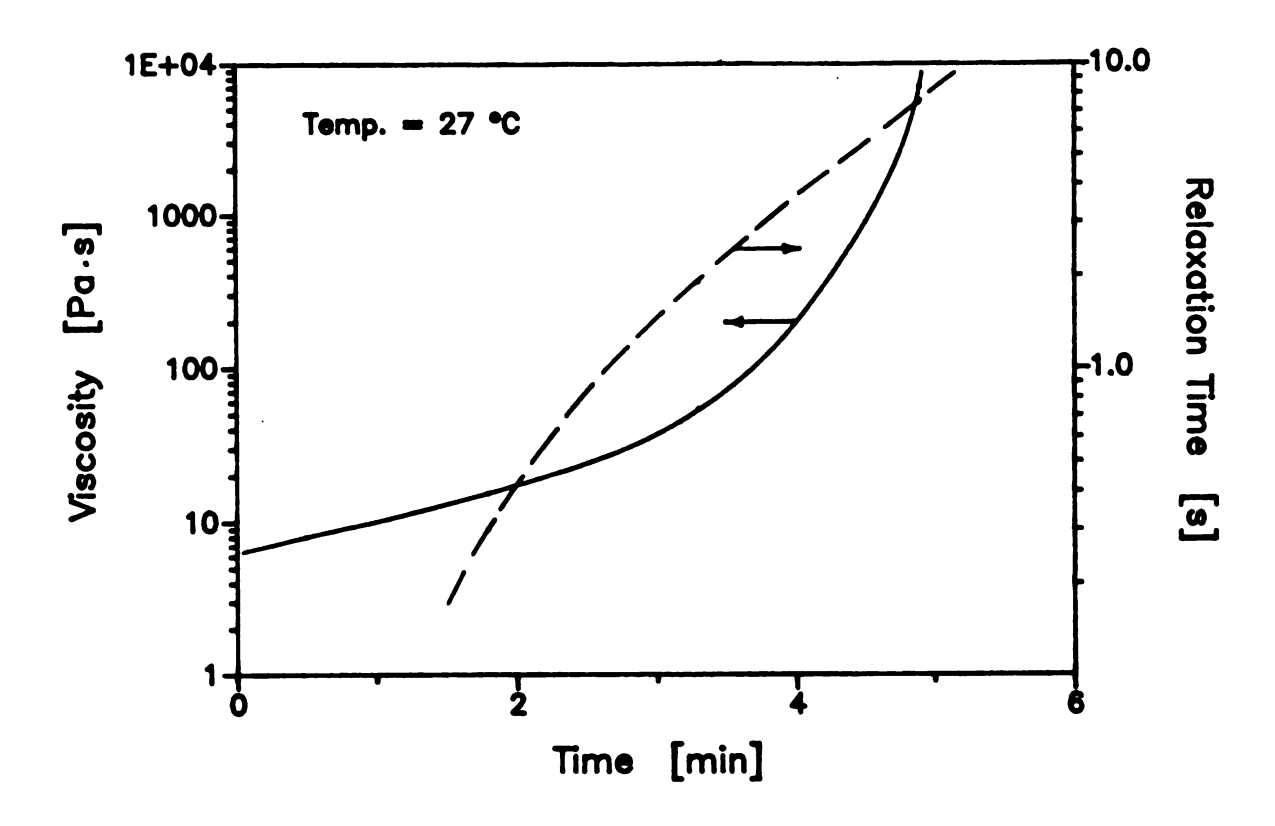


Figure 1.1 The evolution of the viscosity and relaxation time of a 5 minute epoxy resin reacting at room temperature.

depends in part on reducing processing time. A fundamental approach to the solution of this problem entails the study of the dynamics of liquids, characterized rheologically under both shear and extension, flowing through uniform arrays of circular cylinders.

1.2 Newtonian liquid flow in porous media

The earliest scientific work on low Reynolds number flows of Newtonian liquids through isotropic porous media was done by H.P.G. Darcy (1856). He found that the superficial velocity of fluid through a porous medium was proportional to the pressure gradient across the medium. This result is now known as Darcy's law, and in its general form is:

$$\mathbf{v}_o = \frac{-\mathbf{K}}{\eta} \langle \nabla P \rangle \quad . \tag{1.1}$$

Here \mathbf{v}_{o} is the superficial velocity, η is the shear viscosity, \mathbf{K} is the permeability tensor, defined solely by the geometry of the media and $\langle \nabla P \rangle$ is the mean pressure gradient in the liquid. For random media, such as packed beds of spheres, the permeability tensor is isotropic. However, for the uniform arrays of circular cylinders studied here, four components of the tensor in general are necessary to describe the permeability: \mathbf{K}_{11} , \mathbf{K}_{12} , \mathbf{K}_{22} and \mathbf{K}_{33} . In addition, for cylinder arrays with rotational symmetry, such as square and hexagonal pitches, there are only two unknown components, the transverse

and axial permeabilities.

The study of the flow resistance offered by arrays of cylinders has its origins in the design of tubular heat exchangers. The need for more efficient heat transfer equipment continues today, and has prompted the theoretical study of low Reynolds number viscous flows through periodic arrays of cylinders by Sangani and Acrivos (1982). They calculate the drag of a Newtonian liquid on cylinders arranged in square and hexagonal pitches over a wide range of loadings. For void fractions greater than 70 percent, both array geometries offer the same resistance to flow; with void fractions of 50 percent or lower, the square array offers more resistance to the flow of a Newtonian liquid.

Recently, the composite industry has motivated further study of permeation through fiber preforms. Adams et al. (1986) have developed a planar flow technique to study the permeabilities of woven fiber mats. In their experiments an epoxy resin was injected under a constant pressure into a variety of fiber mats, each having various weave patterns and ranging in void fractions from 56 to 91 percent. The epoxy was forced to flow radially in the plane of a preform, and the progress of the flow front was monitored over time. For the case of isotropic mats, the flow front was circular, indicating a radially uniform in-plane permeability which could be backed out by an unsteady material balance and Darcy's law. In the case of anisotropic mats, however, the flow front was elliptic, but also could be predicted using an unsteady material balance and Darcy's law. The in-plane permeability was not constant, however, and had to be described by a linear combination of the permeabilities measured along the principal axes of flow (the

directions of maximum and minimum flow). More recently, Adams and Rebenfeld (1991a,b) have used this same technique to study the in-plane flow through multilayer fabric assemblies, and found that the overall permeability differs from that of the individual constituent layers. Furthermore, they found that flow transverse to the plane was important in maintaining a macroscopically uniform flow front.

1.3 Non-Newtonian flow in random media

One of the earliest studies of non-Newtonian flow through porous media was that of Sadowski and Bird (1965a,b). They studied the flow of shear thinning aqueous polymer solutions through random media. These solutions were virtually inelastic; the maximum time constant being 0.07 seconds. They correlated their data by modifying Darcy's law to include the fluid's shear thinning viscous behavior. This was done by replacing the constant viscosity in Darcy's law with an appropriate generalized Newtonian fluid model - in this case the Ellis model - whose parameters were chosen by fitting the shear viscosity data. This method described the pressure drop-flow rate data well, and has been used in subsequent analyses of the permeation of weakly elastic, shear thinning liquids through random porous media (cf. Christopher and Middleman, 1965). It was not until the work of Marshall and Metzner (1967) that sufficiently high nominal bed strain rates were reached, resulting in flow resistances up to ten times the Newtonian value. These researchers argued that the enhanced pressure drop was the consequence of molecular extension due to the converging-diverging nature of the packed bed; a

feature the capillary models do not contain.

1.4 Corrugated tube models

The inadequacy of the combination Darcy law/generalized Newtonian fluid models to predict the large increases in flow resistances of polymer solutions flowing through random media has lead to new efforts to formulate models which take into account the converging-diverging nature of porous media. The model which has garnered much attention lately is the corrugated tube which is an axisymmetric tube with a sinusoidally varying radius. Over the past twenty years several experimental and numerical investigations concerning the flow of elastic liquids in corrugated tubes has been undertaken (cf. Dodson et al., 1971).

James et al. (1990) report experimental measurements of pressure drop in slow flow of an elastic liquid through a corrugated tube. Their results show little deviation from Newtonian behavior, even at De = 3, and agree very well with the numerical predictions of Pilitsis and Beris (1989) and Burdette et al. (1989). The more recent numerical work includes calculations by Pilitsis and Beris (1989), who use an upper convected Maxwell model and a pseudospectral/finite difference method, and Burdette et al. (1989), who also use an upper convected Maxwell model but an explicitly elliptic momentum equation formulation. The results of these two numerical experiments are in excellent agreement, even at De = 10, and, like the experiments, predict virtually no variation in the flow resistance from the Newtonian value. Only through the inclusion

of inertia have Pilitsis and Beris (1991) been able to predict a substantial enhancement in the flow resistance. These results, both experimental and numerical, indicate that the corrugated tube model is not adequate for describing the flow of viscoelastic fluids in porous media.

A deficiency of the corrugated tube model is its lack of stagnation points (of course, near the tube wall the fluid moves slowly as a result of the no slip condition). The term stagnation point will be used here not only to refer to a point of zero velocity, but also to a point situated in a flow region containing large extensional deformation rates. A macromolecule, flowing into the neighborhood of a stagnation point, will experience high residence times while simultaneously being stretched by the extensional flow. Hence, a stagnation point within the flow ensures the existence of the necessary criteria for a coiled macromolecule to undergo elongation: large residence times and large extension rates.

Stagnation points abound in porous media. For example, each sphere comprising the model random media of the above experiments contains two stagnation points, each located at the poles. Neglecting the complications resulting from sphere-sphere contacts, the fluid directly upstream of a sphere experiences a biaxial extension while the fluid directly downstream of a sphere undergoes uniaxial extension. A similar situation occurs in two dimensions for the flow of liquids transverse to circular cylinders. A cylinder also has two stagnation points; again each located at the poles. Because the flow is two dimensional, the fluid both upstream and downstream of the stagnation points experiences planar elongation.

1.5 Planar elongation

To demonstrate the effect an extensional flow has on flow dynamics, we shall examine the stress developed in a model viscoelastic liquid undergoing a pure elongational flow; the relevant kinematics for this study being planar elongation. The velocity components for a steady planar elongational flow are given by,

$$v_x = x \dot{\epsilon} \tag{1.2}$$

$$v_y = -y\dot{\epsilon} \quad , \tag{1.3}$$

where $\dot{\epsilon}$ is the extension rate and x and y represent perpendicular Cartesian coordinate directions. The rate of deformation tensor for this flow is represented by the matrix, **D**,

$$D = \dot{\epsilon} \begin{bmatrix} 1 & 0 \\ 0 & -1 \end{bmatrix} . \tag{1.4}$$

For this example, a dilute solution of finitely extensible non-linear elastic (FENE) dumbbells will be used as a "realistic" representation of a dilute polymer solution. In the present context, the FENE dumbbell model is realistic in the sense that the total extension of its macromolecular components, the dumbbells, is limited. This prevents the stress from becoming infinitely large in regions of high extension rates. Figure 1.2

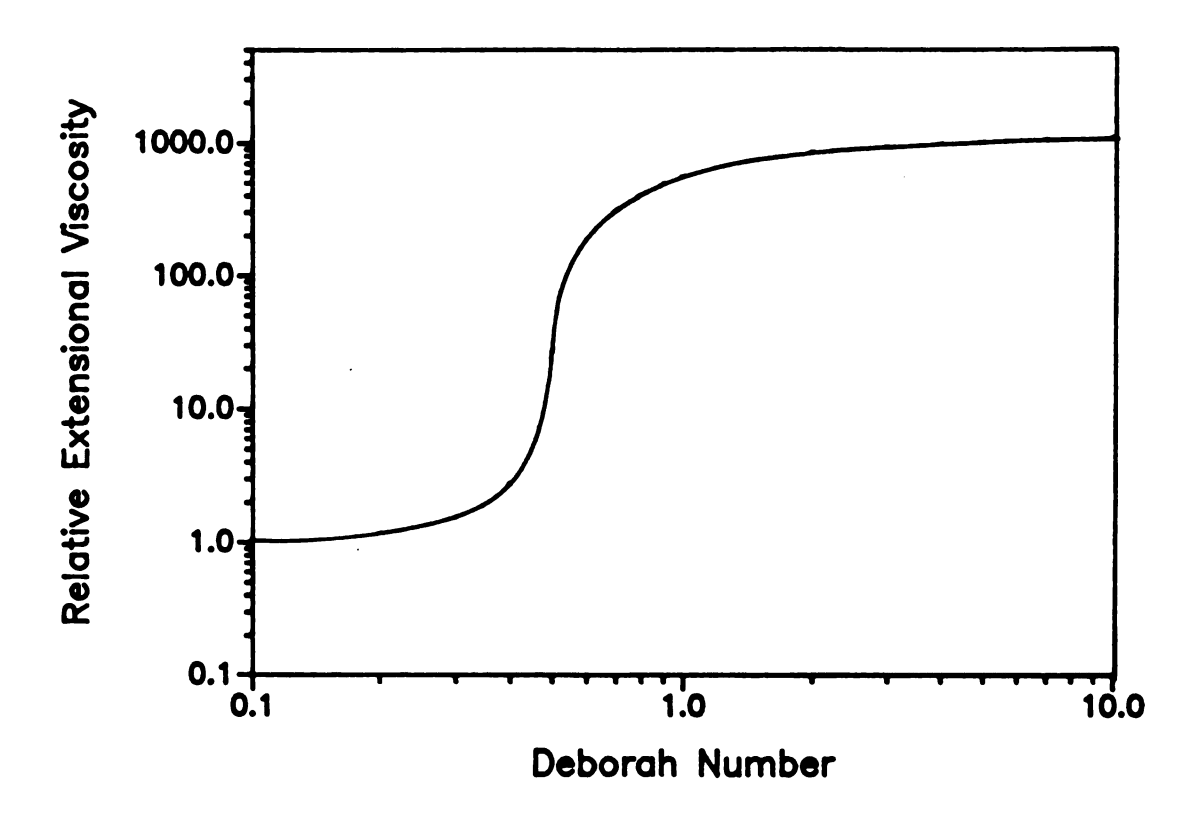


Figure 1.2 The relative extensional viscosity versus De of a FENE dumbbell liquid in a steady planar extensional flow.

shows the steady planar extensional viscosity behavior with Deborah number of Chilcott and Rallison's (1988) FENE dumbbell liquid. The important features of this model prediction are that over a very small range of Deborah numbers the extensional viscosity increases appreciably over the Newtonian value, and that for sufficiently high Deborah numbers the extensional viscosity becomes independent of the Deborah number. Based on this prediction, it is reasonable to expect that at an onset Deborah number the relative flow resistance of viscoelastic liquids, flowing through arrays of cylinders (and for that matter, through any porous media peppered with stagnation points), will increase and then eventually become independent of the Deborah number.

1.6 Dissertation outline

This study is a fundamental investigation of the flow of viscous and viscoelastic liquids through arrays of circular cylinders. Chapter two focuses on the problem of how geometry and fluid rheology affect the flow resistance through model arrays of circular cylinders. Rheologically characterized fluids in both shear and extension are used to elicit what fluid and geometric parameters are important in predicting the dynamic behavior of fluids in cylinder arrays. In chapter three laser Doppler velocimetry and streak photography are used to examine how the kinematics of the cylinder array flows are affected by the fluid rheology. Chapter four presents experimental data showing the effects of array geometry on macromolecular chain scission of a high molecular weight polymer solution flowing through rectangular array and in a hexagonal arrays. Chain

experimental observations. Finally, whereas the previous chapters consider the effect of fluid elasticity on the permeation of liquids through cylinder arrays, chapter five considers the effects of cylinder array compliance on crossflow permeation. This is done through an analysis of the hot melt impregnation process which is used in the manufacture of composite prepreg. In this chapter it is shown that fiber bundle elasticity has a profound effect on the permeation of viscous liquids into fiber arrays.

Chapter 2

THE EFFECT OF POLYMER EXTENSIBILITY ON THE FLOW OF POLYMER SOLUTIONS THROUGH CYLINDER ARRAYS

2.1 Summary

The effects of fluid rheology on low Reynolds number flows transverse to periodic arrays of circular cylinders have been investigated with several solutions of polyisobutylene. Care was taken to avoid degradation of the polymer during the measurements. These solutions were rheologically characterized in both shear and extension. Three of the solutions are dilute solutions of different molecular weight polyisobutylenes in polybutene at the same concentration. These are θ -systems at room temperature and have a constant shear viscosity over strain rates up to 10 s^{-1} . Fiber spinning of these solutions indicates that the apparent Trouton ratio at an average stretch rate of 15 s^{-1} is proportional to the molecular weight. This is consistent with predictions of FENE dumbbell models for higher elongation rates (cf. Chilcott and Rallison, 1988; Biller et al., 1986). A fourth solution of polyisobutylene in decalin was used to evaluate

the flow resistance for shear thinning solutions.

The resistance to flow of the non-shear thinning solutions in both square and hexagonal pitch arrays is above the Newtonian value at onset Deborah numbers of 0.80 and 0.35 respectively. These onset values are independent of solute molecular weight. Higher molecular weight fluids produce higher flow resistances relative to the Newtonian value for Deborah numbers greater than the onset value. At large Deborah numbers (De >> 1) the relative flow resistances in both arrays become independent of Deborah number, and scale linearly with the molecular weight. The asymptotic value of the resistance ratio is consistently higher for the hexagonal array than for the square array for the same molecular weight. This is shown to be a result of these transverse flows being dominated by planar extension at high Deborah numbers.

2.2 Introduction

It is well recognized that the dynamics of shear thinning polymer solutions may be affected by the finite extensibility of its macromolecular components (cf., Christiansen and Bird, 1977/1978). In spite of this, the effect of varying polymer extensibility on the fluid dynamics of non-shear thinning elastic liquids, the so-called Boger liquids (Boger, 1977/1978), has not adequately been explored. A reason for this may be that the polybutene based Boger liquids have been shown to behave in both shear and extension as a dilute solution of infinitely extensible, linear dumbbells at low to moderate deformation rates (see Prilutski et al., 1983 and Sridhar et al., 1986 respectively). In

strong flows, however, where the Deborah number (De) is much greater than one, this model breaks down because a linear dumbbell will extend without bound in such a flow (Rallison and Hinch, 1988). This may be one reason that numerical simulations using Oldroyd type constitutive models fail quantitatively, and sometimes even qualitatively, to account for important flow phenomena observed for Boger fluids undergoing complex flows. Only recently have researchers begun to explore other models in order to better understand the physics behind the flow properties of polymer solutions. For example, Chai and Yeow (1990) use a multiple relaxation time constitutive model (KBKZ model) to describe the flow of a Boger fluid in a gravity drawn jet. They found better agreement with experimental data using the KBKZ model than with the Oldroyd-B model.

In the present investigation the effect of varying finite extensibility of the polymer on the dynamics of complex flows of Boger liquids will be examined. This study is partially motivated by the work of Chmielewski et al. (1990a) who observed opposite trends with Deborah number in the relative drag on spheres, translating in corn syrup based polyacrylamide solutions versus polybutene based polyisobutylene solutions. This difference was attributed to differences in the extensions of the polymers from equilibrium. Polyacrylamide molecules tend to be relatively elongated in aqueous solutions at equilibrium while polyisobutylene molecules in polybutene tend to be relatively coiled at equilibrium.

In a previous investigation, Chmielewski et al. (1990b) reported that the pressure drop in flow transverse to arrays of circular cylinders is much greater for an elastic

Boger liquid than the pressure drop for Newtonian liquids of equivalent viscosity; similar to that of polymer solutions in isotropic porous media. The focus of their study, however, was on how differences in the extensional flow field between hexagonal and rectangular pitch geometries affected polymer extension, and in turn molecular chain scission.

In this work three Boger fluids are prepared with varying degrees of polymer extensibility in order to understand its effect on the flow resistance of these fluids in cylinder arrays. Two array geometries are studied, square and hexagonal, both having a void fraction of 70 percent. Unsteady extensional viscosity data, obtained by fiber spinning, is correlated with high Deborah number flow resistance asymptotes found in both array geometries via molecular finite extensibility. A fourth, more concentrated polymer solution is also examined in order to compare the effects of shear thinning on fiber spinning and cross flow resistance.

2.3 Experimental

2.3.1 Materials

Three classes of liquids were used in this study: two Newtonian liquids of widely different viscosities, three non-shear thinning, elastic liquids which differed only by their solute molecular weights, and a highly shear thinning, viscoelastic polymer solution. A comparison of some of the material properties of these fluids can be found in Table 2.1. The two Newtonian liquids were 610 and 1290 weight average molecular weight

Table 2.1 Properties of the test fluids at 20 °C.

FLUID	M _w	7 Pa∙s	λ ₁ s	ρ kg/m³
NEWTONIAN				
Polybutene, H25	610	5.08		871
Polybutene, H300 7.45 % Kerosene	1290	45.05		891
VISCOELASTIC Boger Liquids				
Solvent				
93.0 % PB, H25 7.0 % Kerosene	610	1.63		867
Solutions				
0.20 % PIB L-80	0.90x10 ⁶ *	2.46	0.057	867
0.20 % PIB L-100	1.25x10 ⁶ *	2.78	0.085	867
0.20 % PIB L-140	2.11x10 ⁶ *	3.66	0.258	867
VISCOELASTIC Shear Thinning				
Solvent				
Decalin	138.25	0.0027		883
Solution				
2 % PIB B200	4.30x10 ⁶	21.89**	8.55	880

^{*} Viscosity averaged molecular weight

^{**} Zero shear viscosity

polybutenes (PB) supplied by Amoco Chemical Company. A small amount of kerosene (7.45 %) had to be added to the higher molecular weight grade in order to reduce its viscosity to a manageable level. The three Boger solutions were all prepared by dissolving an appropriate amount of polyisobutylene (PIB), supplied by Exxon Chemical Company, into kerosene and then mixing the solution into Amoco's 610 molecular weight (MW) grade PB for a final composition by weight of 0.20 % PIB, 7.00 % kerosene and 92.80 % PB. Three PIBs, having different molecular weights, were used: (1) Exxon's Vistanex L-80 with a viscosity average molecular weight of 0.90 (± 0.15) x 10⁶, (2) Vistanex L-100 with a viscosity average molecular weight of 1.25 (± 0.19) x 10⁶ and (3) Vistanex L-140 with a viscosity average molecular weight of 2.11 (± 0.24) x 10⁶.

The shear thinning, viscoelastic liquid was a 2 % solution of PIB (BASF B200) in a cis and trans decalin mixture. This fluid was supplied by Professor Walters, and its preparation and composition were identical to the *D1* liquid used in the *Second Normal Stress Difference Project* (Walters, 1983).

2.3.2 Shear flow properties

Rheological measurements in steady and oscillatory shear were made on a Rheometrics RFS-8400 Fluids Spectrometer at rates ranging between 0.1 and 100 s⁻¹. These tests were performed using a 0.02 radian cone and a 5 cm diameter plate. Measurements made on the Newtonian and Boger liquids were performed at 10, 20 and 30 °C, while tests made on the remaining liquid were performed at 0, 20 and 40 °C. Attempts to study the PIB/decalin solution at temperatures higher than 50 °C were

unsuccessful due to enhanced solvent evaporation. Figure 2.1 (a) shows the solvent viscosity, η_s , and the steady shear viscosity, η_s , of the three PB/PIB solutions as a function of the shear rate. None of these liquids were significantly shear thinning over the range of shear rates tested. On the other hand, the shear viscosity of the PIB/decalin solution was constant only up to 0.1 s⁻¹, and then decreased with increasing shear rates (see Figure 2.1 (b)).

Intrinsic viscosity, $[\eta]_o$, measurements were made on the PB/PIB solutions to assess the thermodynamic solvent quality near 20 °C. This was accomplished by calculating the relative viscosities, η_r , of three different concentrations of each of the PB/PIB solutions. A linear extrapolation of $\ln(\eta_s)/c$ to infinite dilution was made to determine $[\eta]_o$ (see Figure 2.2 (a)). In Figure 2.2 (b) the relationship between $[\eta]_o$ and M_r is shown to follow the Mark-Houwink relation,

$$\left[\eta\right]_{o} = K' M_{v}^{\overline{a}} \quad . \tag{2.1}$$

The Mark-Houwink exponent, \bar{a} , is approximately 0.5, indicating that the PB/PIB solutions of this study were examined under theta conditions. The pre-exponential factor, K', is 0.40 cm³/g.

Figure 2.3 (a) shows the storage modulus, G', of the three PB/PIB solutions. A relaxation time for each of the solutions (see Table 2.1) is calculated by,

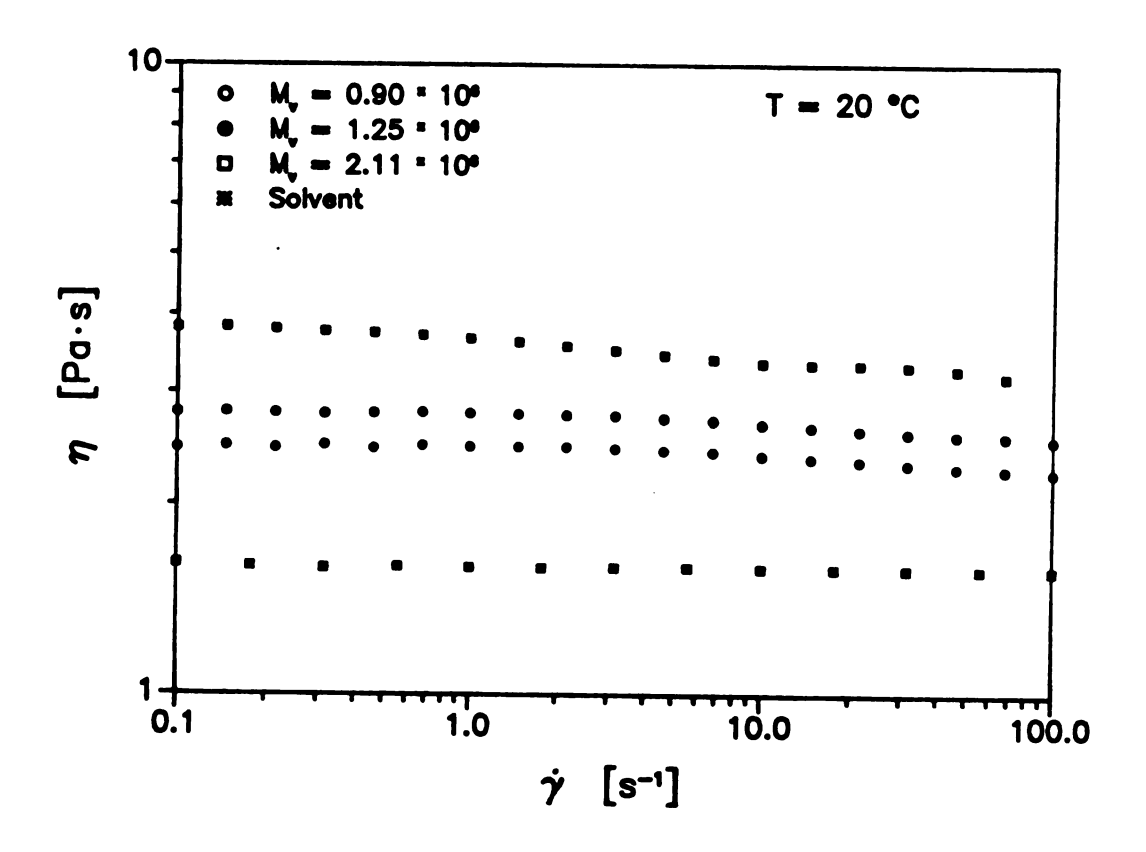


Figure 2.1 (a) Steady shear viscosity of the PIB in PB solutions.

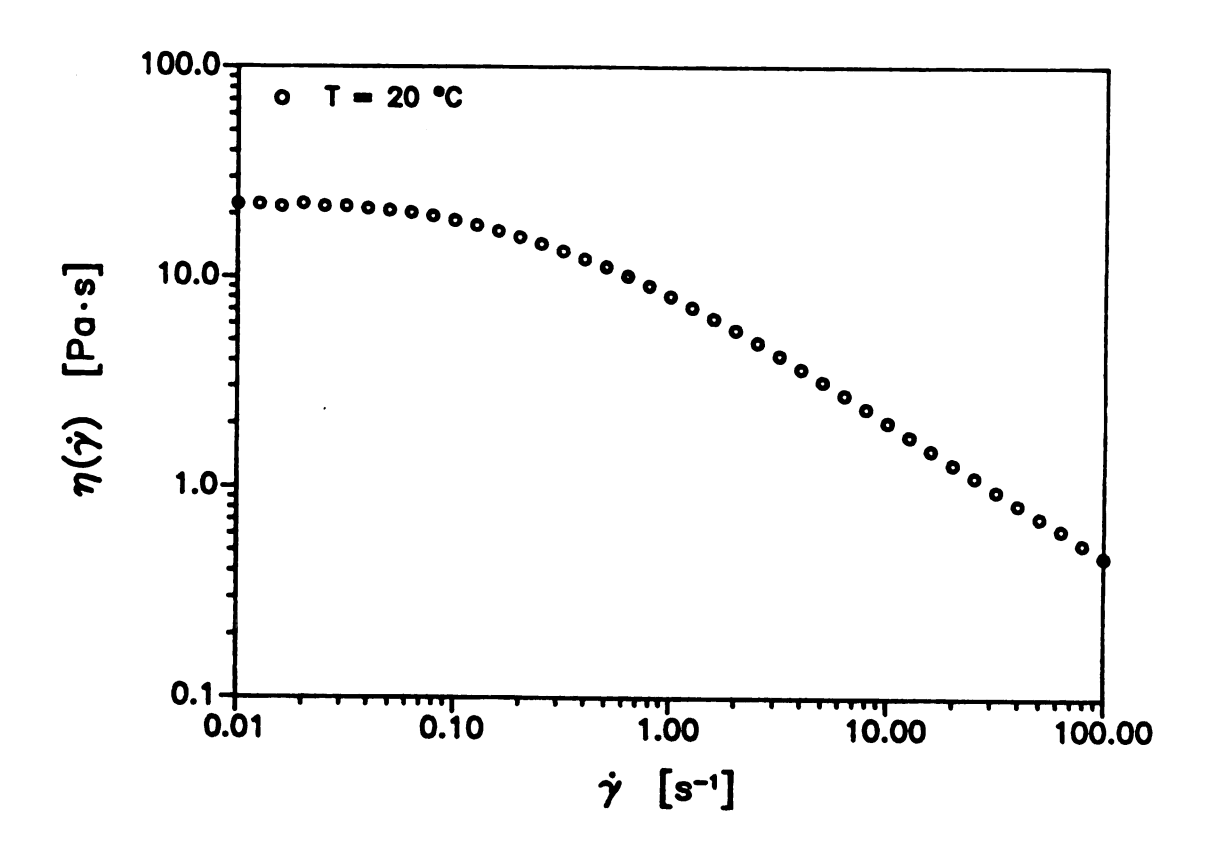


Figure 2.1 (b) Steady shear viscosity of the PIB in decalin solution.

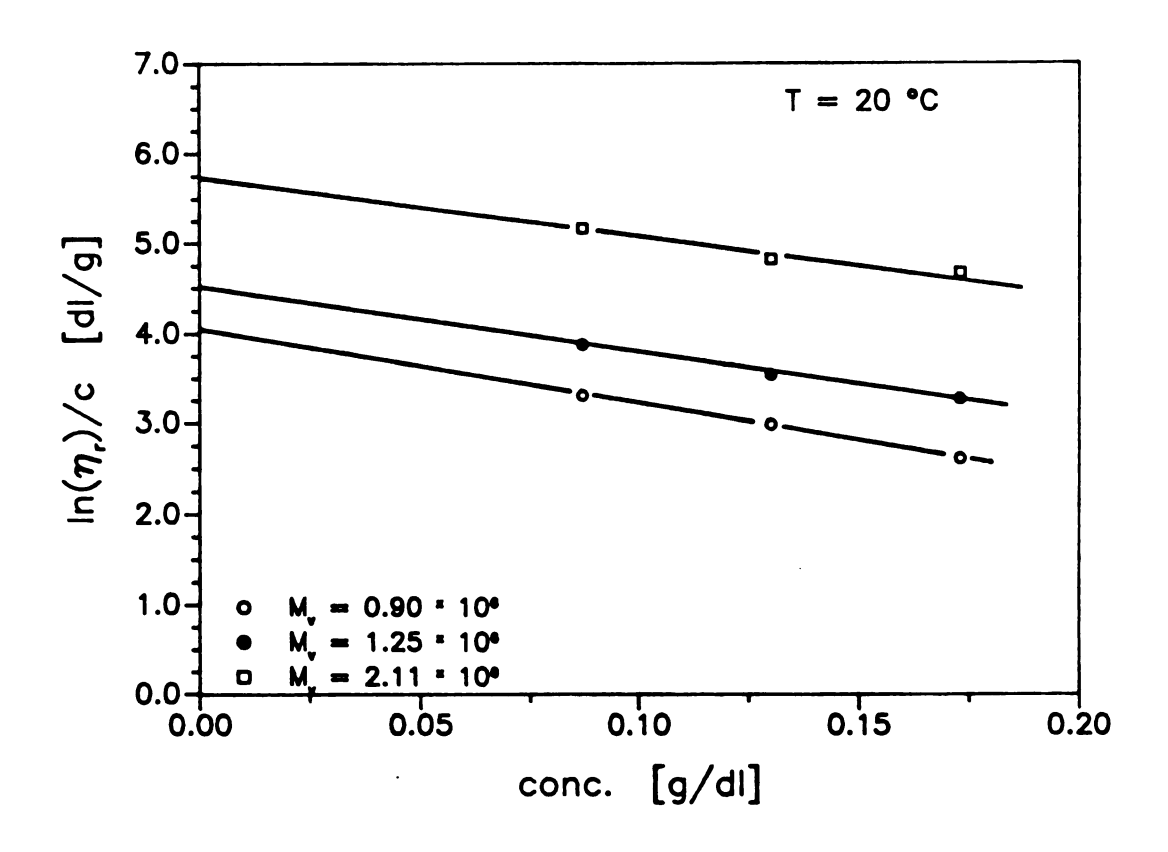


Figure 2.2 (a) Relative viscosities of the PIB in PB solutions as a function of solution concentration.

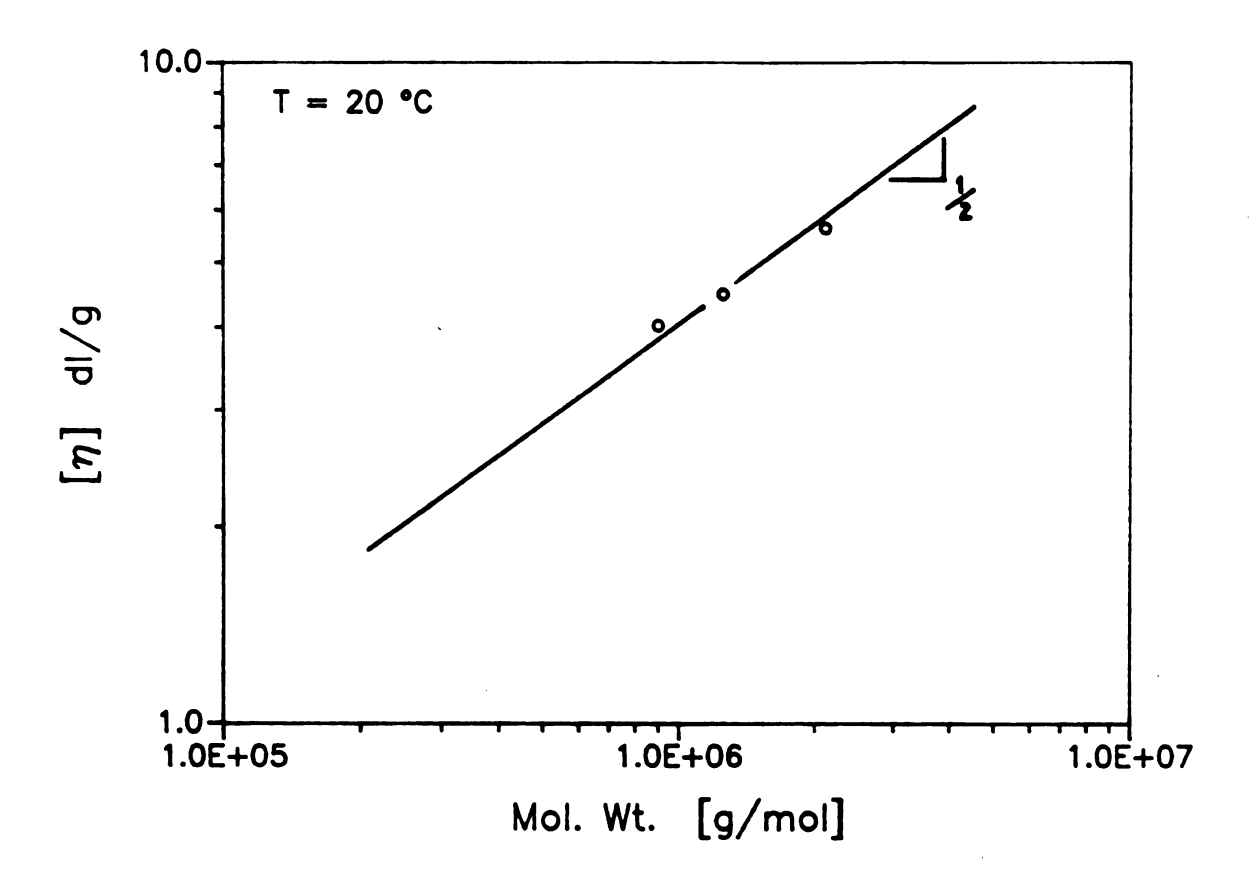


Figure 2.2 (b) Intrinsic viscosities of the PIB in PB solutions.

$$\lambda_1 = \frac{G'}{\omega^2 (\eta_Q - \eta_Z)} \quad . \tag{2.2}$$

The value of the storage modulus is taken from the low frequency region where G' is quadratic in frequency. Figure 2.3 (b) shows the dynamic moduli, at 20 °C, of the PIB/decalin solution. The storage modulus of this fluid also shows quadratic behavior with frequency, but at much lower rates than the liquids of Figure 2.3 (a).

2.4 Fiber spinning

2.4.1 Extensional flow apparatus

The unsteady elongational flow properties of the elastic fluids were measured by fiber spinning. The apparatus, shown schematically in Figure 2.4, is similar to that of other researchers (see Hudson et al., 1974, for example), and utilizes a bending beam load cell to measure the force exerted by test fluids on the capillary. Nitrogen pressure is used to pump fluid from a reservoir and through a 20 cm long stainless steel capillary (0.238 cm I.D.). The capillary pivots at its upstream end via a miniature ball bearing and is attached to the load cell at its downstream end.

The bending beam load cell consists of a 7.0 cm by 1.3 cm by 0.013 cm strip of spring steel, acting as a cantilever beam. The free end of the beam is attached to the end of the capillary. At the fixed end of the beam, four encapsulated foil strain gages (Omega Engineering, model DY11) are arranged to form a Wheatstone bridge. The

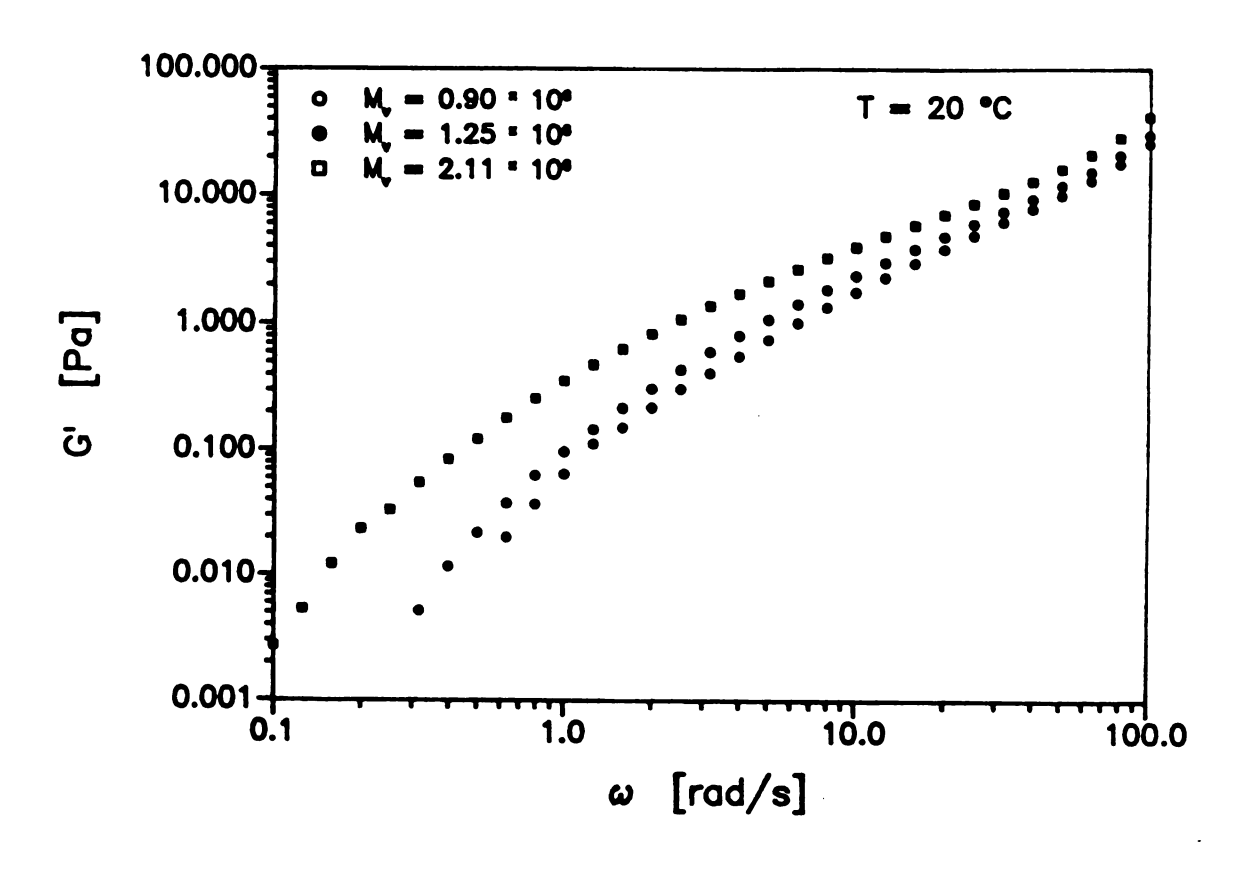


Figure 2.3 (a) Dynamic storage moduli of the PIB in PB solutions.

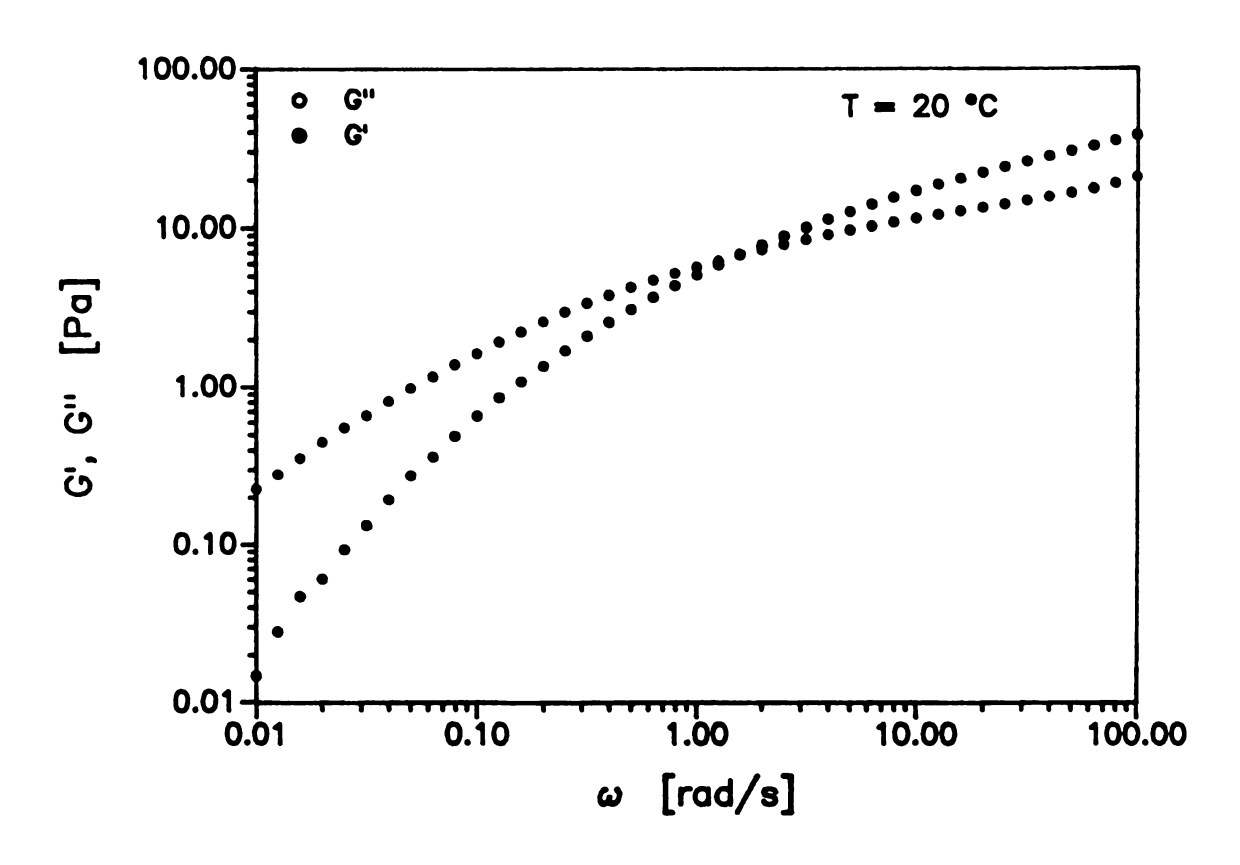


Figure 2.3 (b) Dynamic moduli of the PIB in decalin solution.

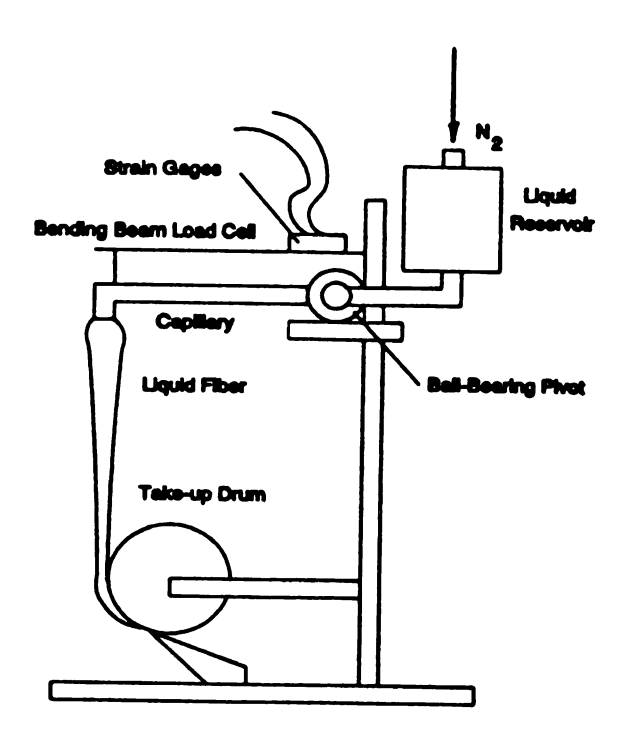


Figure 2.4 Schematic of the fiber spinning apparatus.

bridge is powered with 10 volts and emits a millivolt signal proportional to the bending strain in the beam. The beam strain, ϵ_B , is proportional to both the applied force, F_B , and the moment arm, l_B , according to,

$$\epsilon_B = \frac{6 F_B l_B}{E_B b h_B^2} \quad , \tag{2.3}$$

where b is the width of the beam, h_B is the beam thickness and E_B is the beam modulus. The load cell is sensitive to 0.1 mN and the signal output is linear over the range of forces measured in this study (4 to 50 mN). The utility of this force measurement method is not only its cost effectiveness, but it also provides a convenient way of adjusting the sensitivity of the load cell to meet the needs of a particular application.

Steady extension of a liquid filament extruding from the capillary is maintained by an adjustable speed take-up drum at the downstream end of the fiber. Still photograph enlargements of an elongated liquid fiber are used to obtain filament diameter profiles.

Table 2.2 lists the operating parameters of the elongational flow experiments performed on each of the PIB test solutions.

2.4.2 Extensional flow results and discussion

The fiber spinning experiments were conducted under isothermal conditions and such that gravity, surface tension and fluid inertia were all very small compared to the tensile force. The cross sectional average of the tensile stress at any axial location, z,

Table 2.2 Operating parameters in fiber spinning experiments.

FLUID	TEMP °C	Q cm³/s	F _B	L _{FE}	D,
Boger Liquids					
0.20 % PIB L-80	21	0.200	6.8	5.7	19.4
0.20 % PIB L-100	21	0.241	16.0	5.6	18.1
0.20 % PIB L-140	21	0.151	50.4	4.4	19.4
Shear Thinning					
2 % PIB B200 1.	23	0.526	10.2	6.3	5.7
2.	23	0.526	20.2	6.1	8.7
3.	23	0.223	4.0	7.7	10.6
4.	23	0.223	6.2	7.9	14.8
5.	23	1.008	. 13.4	9.0	4.5

down the fiber was calculated by,

$$T_{zz}(z) - T_{zz}(z) = \frac{4 F_B}{\pi D(z)^2}$$
, (2.4)

where T_{zz} and T_{rr} are components of the total stress tensor, F_B is the tensile force and D(z) is the diameter of the filament at location z. The extensional strain rate will be represented by the average, $\langle \dot{\epsilon} \rangle$,

$$\langle \dot{\epsilon} \rangle = \frac{v(L_{pg}) - v(0)}{L_{pg}},$$
 (2.5)

where L_{FS} is the length of the fiber, and v(0) and $v(L_{FS})$ are the axial velocities at the capillary outlet and at the take-up drum respectively. Since the axial velocity profiles in these spinning experiments are nearly linear, the local extensional strain rates at all axial locations are approximately equal to the average extensional strain rate. Combining Eqs. 2.4 and 2.5, the transient extensional viscosity can be represented as,

$$\eta_{z}^{+}(z) = \frac{T_{zz}(z) - T_{zz}(z)}{\langle \dot{\epsilon} \rangle} .$$
(2.6)

The fiber spinning results of the PB/PIB solutions are shown in Figures 2.5 (a)

and (b). In Figure 2.5 (a) the transient extensional viscosity is scaled with 3η and the time is scaled with λ_1 . This figure indicates a molecular weight effect on the transient extensional viscosity independent of the dominant molecular time scale. An average extensional viscosity between two points on the spin line may be calculated as suggested by Mackay and Petrie (1989),

$$\overline{\eta}_{E} = \frac{4F_{B}L_{FS}}{\pi D(0)^{2} V(0) \ln(\frac{V(L_{FS})}{V(0)})} . \qquad (2.7)$$

The ratio of the extensional viscosity to the shear viscosity, accounting for the polymer contribution, is plotted against molecular weight in Figure 2.5 (b). Since these fluids had similar pre-shear histories and were spun at approximately the same extension rate $(\dot{\epsilon} \sim 15 \text{ s}^{-1})$, these results demonstrate that the apparent Trouton ratio scales linearly with the molecular weight. This result can be anticipated by treating the Boger fluids as a dilute solution of finitely extensible non-linear elastic (FENE) dumbbells. At sufficiently large Deborah numbers (De > 1) the extensional viscosity in a uniaxial extensional flow scales with the square of the extensibility parameter, L (cf. Chilcott and Rallison, 1986 and Bird et al., 1987),

$$\frac{\eta_B - 3\eta_B}{\eta - \eta_B} \propto L^2 - 1 \quad , \tag{2.8}$$

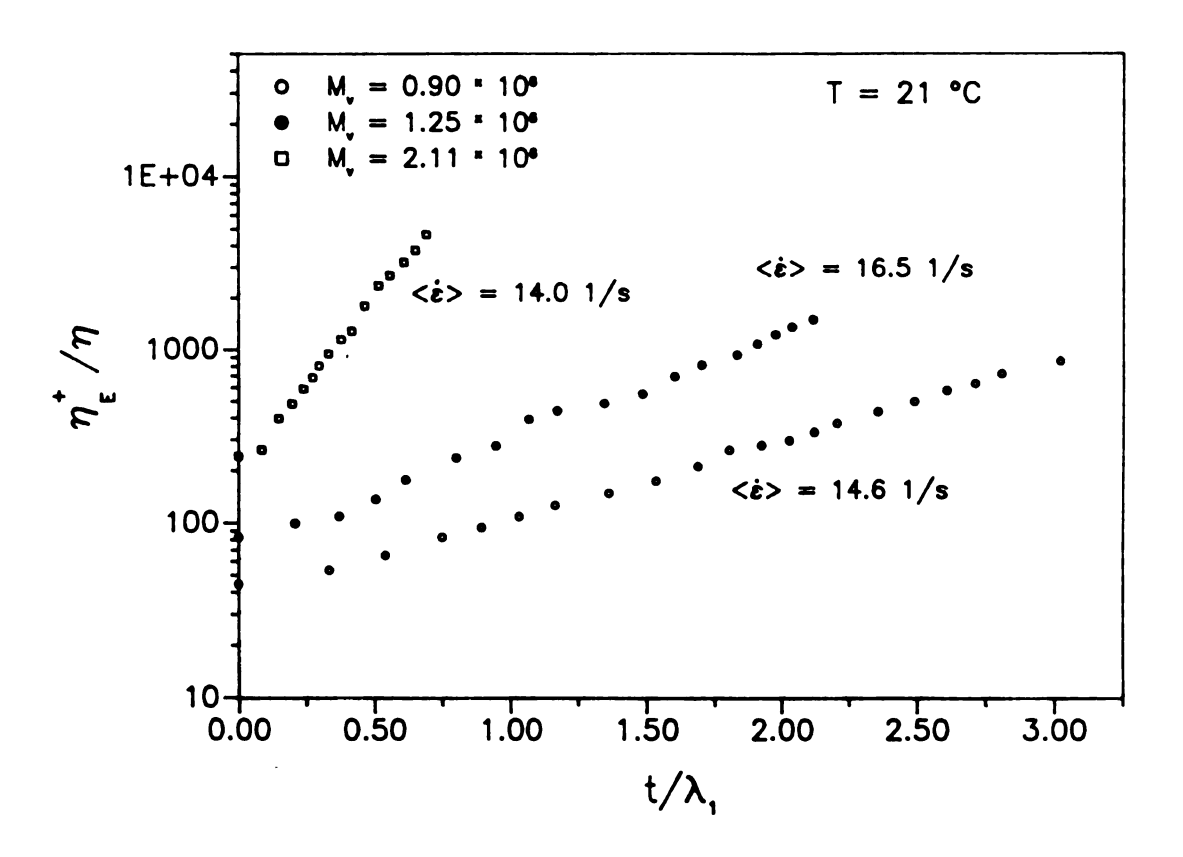


Figure 2.5 (a) Transient extensional viscosities as measured by fiber spinning for the PIB in PB solutions.

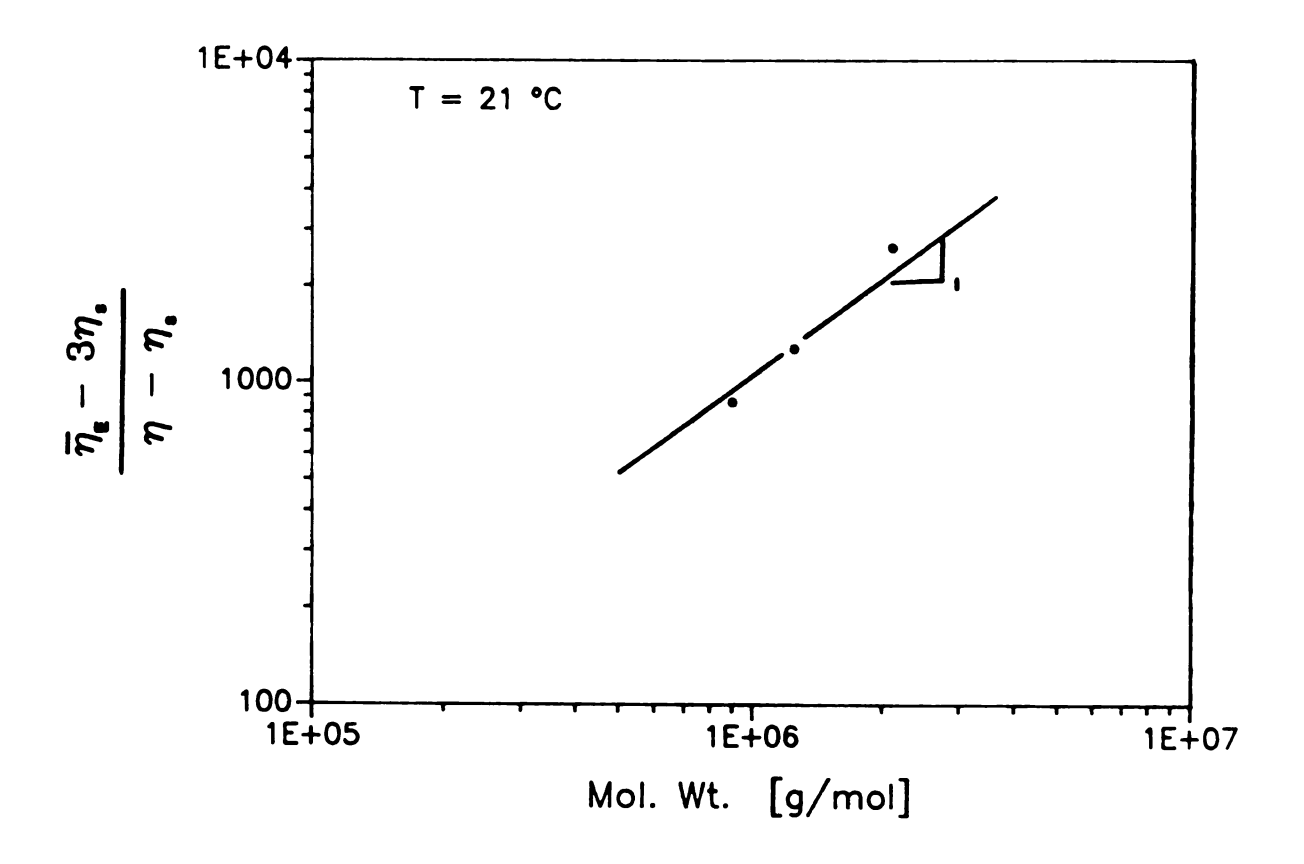


Figure 2.5 (b) Apparent Trouton ratios, accounting for the polymer contribution, based on fiber spinning measurements taken at $\dot{\epsilon} \sim 15 \text{ s}^{-1}$ for the PIB in PB solutions.

where L^2 represents the ratio of the mean square end-to-end distance for the fully extended polymer molecule to its equilibrium value. For a theta system, the mean squareend-to-end distance of a polymer molecule scales linearly with the molecular weight,

$$\langle r^2 \rangle_{\alpha\sigma} \propto M_W$$
 (2.9)

The mean square end-to-end distance of the fully extended chain scales with the square of the molecular weight,

$$\langle r^2 \rangle \propto M_W^2 \quad . \tag{2.10}$$

Thus, by definition the square of the extensibility of a polymer molecule in a theta solvent is proportional to its molecular weight,

$$L^2 = \frac{\langle r^2 \rangle}{\langle r^2 \rangle_{eq}} \propto M_W , \qquad (2.11)$$

and hence,

$$\frac{\eta_B - 3 \eta_g}{\eta - \eta_g} \quad \ll \quad M_W \quad . \tag{2.12}$$

The fiber spinning experiments on the PIB/Decalin solution were performed over a range of flow rates, fiber lengths and draw ratios (see Table 2.2). Figure 2.6 shows the apparent Trouton ratio plotted against the extension rate for five different tests. Here, the average extensional viscosity is divided by the shear viscosity evaluated at a shear strain rate of $\dot{\gamma} = \sqrt{3} \dot{\epsilon}$.

2.5 Crossflow through cylinder arrays

2.5.1 Permeation apparatus

The experimental apparatus used in this study was similar to that of Chmielewski et al. (1990a) with modifications aimed at minimizing polymer degradation and providing a means of flow visualization. A set of experiments was initiated by charging the holding tank with a fresh 8 liter batch of test fluid (see Figure 2.7). Approximately 2 liters of this fluid was then pumped via a peristaltic pump (TAT Engineering, model 110-43E) into a reservoir. Regulated nitrogen was used to move the fluid from the reservoir, through the permeation apparatus and back into the holding tank. Pressure transducers on either side of the cylinder array provided pressure drop measurements, and the flow rate was obtained by monitoring the change in liquid level within the reservoir over time. The same 8 liter charge was used throughout the permeation testing of one cylinder pitch type. When the cell geometry was changed a fresh batch of fluid was employed.

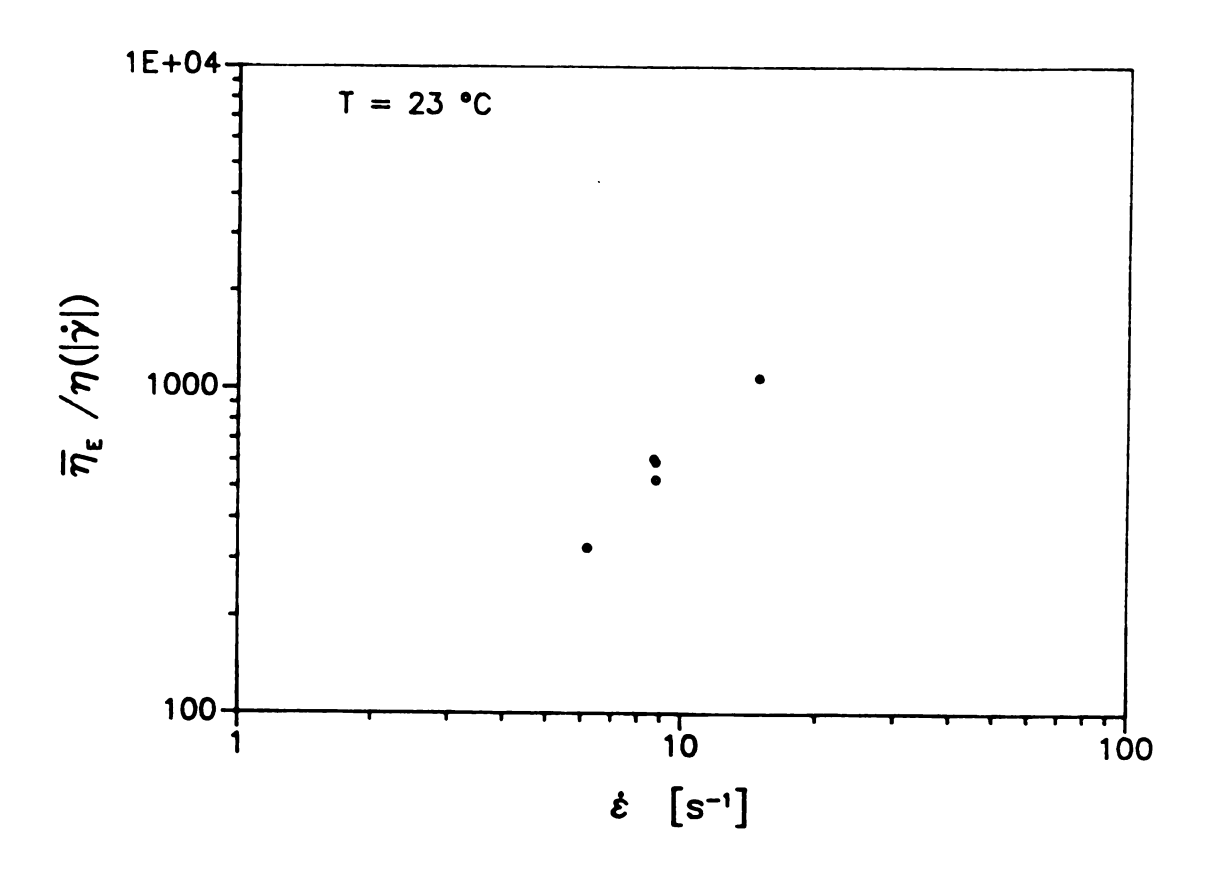


Figure 2.6 Apparent Trouton ratios based on fiber spinning data of the PIB in decalin solution where the values of η are determined at $\dot{\gamma} = \sqrt{3} \dot{\epsilon}$.

Permeation Apparatus

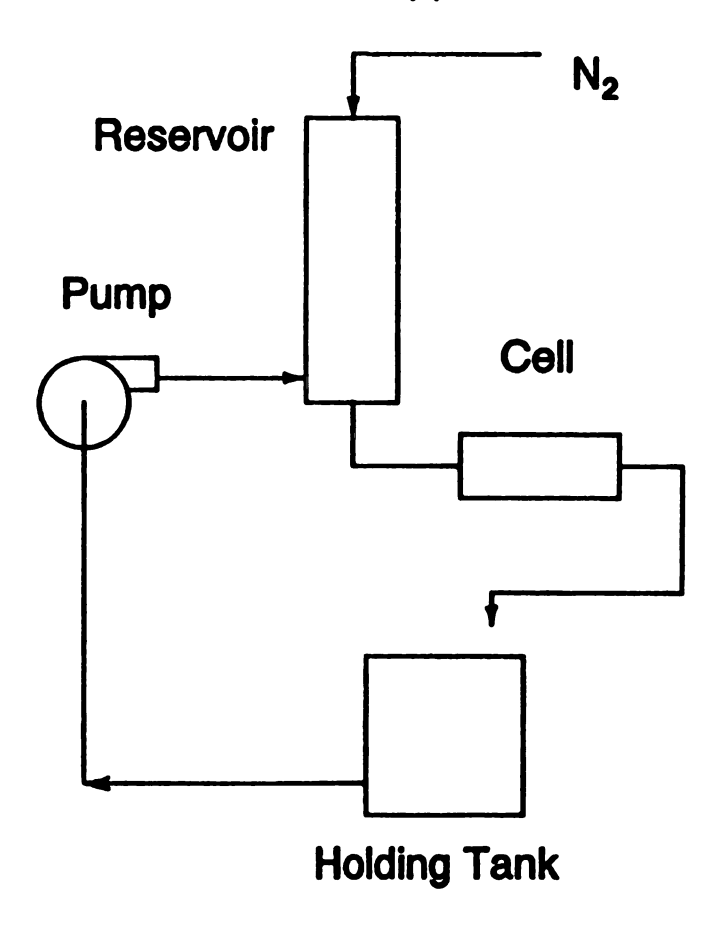


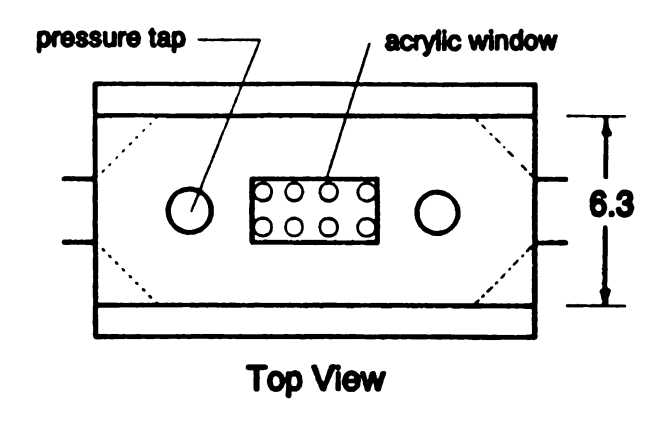
Figure 2.7 Schematic of the permeation apparatus.

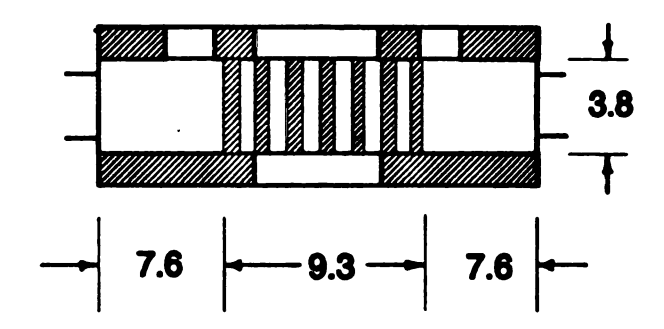
Two permeation cells are used which differ only in the packing geometries of the cylinder arrays they contain. Figure 2.8 shows a schematic of the permeation cells. The test fluid enters the cell through a 2.5 cm I.D. pipe and travels through a 7.6 cm long transition region before reaching the cylinder array. The cross section of the cell is rectangular and measures 6.3 cm by 3.8 cm. As shown in the top view on Figure 2.8, solid wedges fill the corners of the cell to facilitate a smooth transition of the fluid as it enters and leaves the cell.

The arrays are composed of acrylic circular cylinders, 0.476 cm in diameter and 3.8 cm long. The cylinders are situated so that their axes are perpendicular to the flow, and they are flush with the cell walls to prevent fluid channeling. Wall and end effects are known to be negligible (see Chmielewski et al., 1990a). Cylinder bed lengths in both cells are approximately 9.3 cm (12 rows) and contain flush mount diaphragm type pressure transducers (Omega Engineering, model PX102) on either side. A chart recorder was used to monitor the upstream and downstream pressures over the duration of each test. Figure 2.9 shows the square and hexagonal pitch geometries. As shown in Figure 2.9, the cylinders in the square pitch are spaced 0.771 cm from center to center and in the hexagonal pitch the cylinders form equilateral triangles which are 0.828 cm on a side and 0.717 cm in height.

2.5.2 Flow unsteadiness

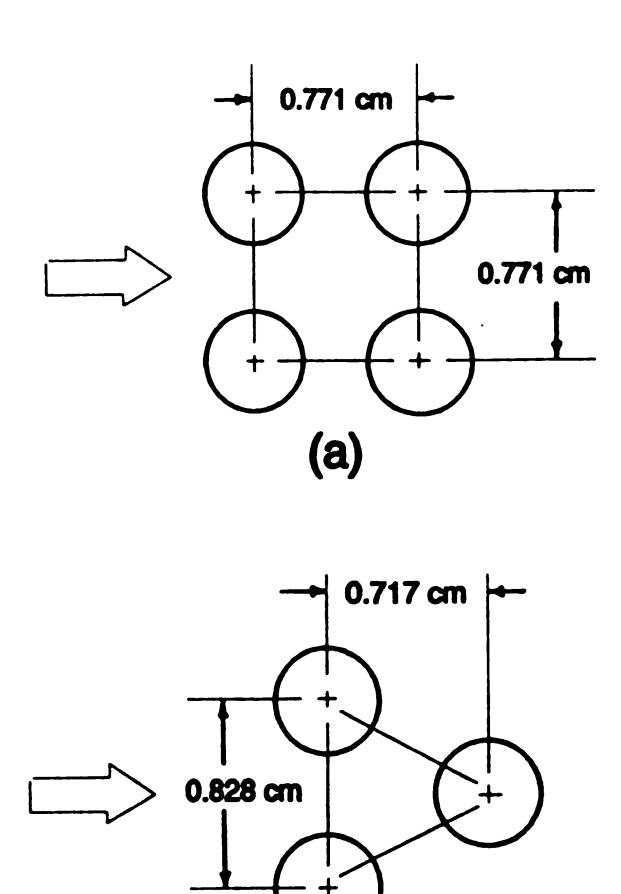
Both upstream and downstream pressure traces of the Newtonian fluids showed no variation with time. This was not the case with the viscoelastic fluids. Small





Side View (cross section)

Figure 2.8 Schematic of the permeation cells (all dimensions in cm).



(b)

Figure 2.9 Geometry of the circular cylinders (radius = 0.238 cm) (a) square pitch (b) hexagonal pitch.

amplitude oscillations were recorded by the downstream pressure transducer at a Deborah number of 1.2 for all of the non-shear thinning elastic fluids. Above this onset, the pressure oscillations grew in amplitude up to 2 percent of the average pressure with increasing Deborah number; the Deborah number was controlled by the flow rate. At no time were pressure fluctuations observed upstream of the cylinder arrays. No pressure fluctuations were recorded in flow through a blank channel at Deborah numbers up to 4. This indicates that the unsteadiness resulted from fluid elasticity in flow through the array of cylinders.

Two examples of pressure traces for the square and hexagonal array of the 2.11 x 10^6 molecular weight solution at De ~ 2.6 are given in Figure 2.10. In both traces the upstream and downstream measurements are on a different scale. Figure 2.10 (a) represents the pressure over time of a test run in the hexagonal array. At a flow rate of 81 cm^3 /s the upstream pressure measured $2.92 \times 10^5 \text{ Pa}$ (42.3 psi), while the downstream pressure fluctuated around an average value of $0.11 \times 10^5 \text{ Pa}$ (1.6 psi). At this Deborah number the amplitude of oscillation is approximately 2 percent of the average pressure and the dominant frequency is approximately 0.2 Hz. A pressure trace at De = 2.6 for the square array is given in Figure 2.10 (b). Here the flow rate is 113 cm^3 /s, and the corresponding upstream pressure is $1.78 \times 10^5 \text{ Pa}$ (27.8 psi). The downstream pressure oscillates around the mean of $0.17 \times 10^5 \text{ Pa}$ (2.5 psi). Again the amplitude of oscillation is about 2 percent of the mean pressure, and the dominant frequency is approximately 0.4 Hz. Though this estimate of a characteristic frequency of the pressure fluctuations is crude, it still bears pointing out that these frequencies are of the same order of

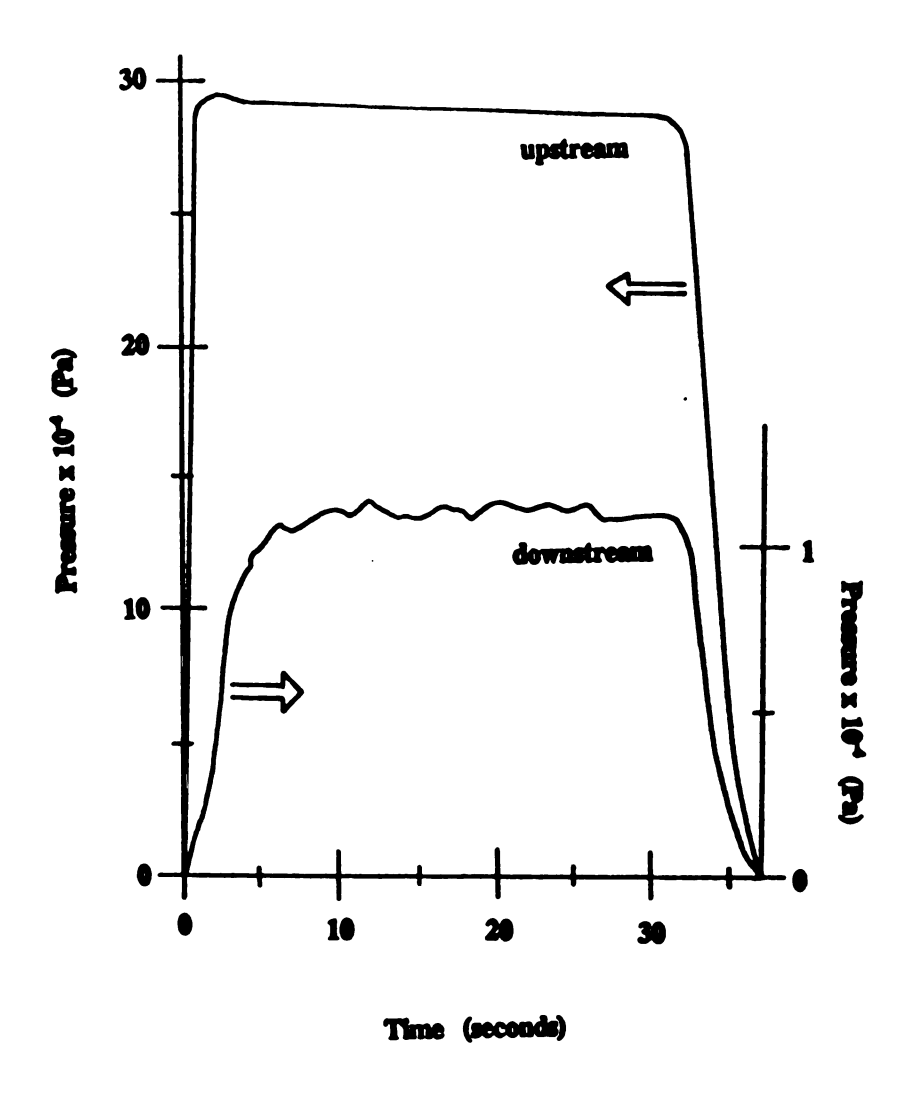


Figure 2.10 (a) Pressure traces for the 2.11 x 10^6 molecular weight PIB/PB solution in the hexagonal array at De = 2.6 (Q = 81 cm³/s, upstream P = 29.2 x 10^4 Pa, downstream P = 1.1 x 10^4 Pa).

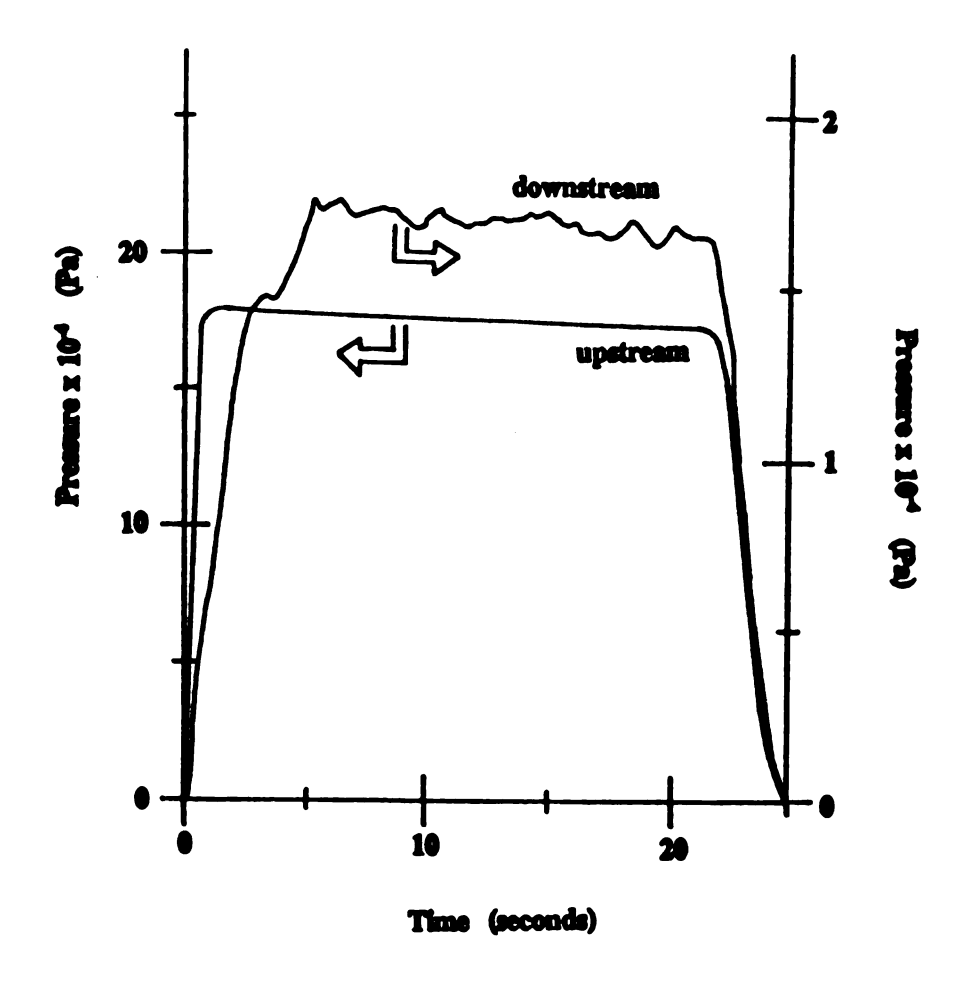


Figure 2.10 (b) Pressure traces for the 2.11×10^6 molecular weight PIB/PB solution in the square array at De = 2.6 (Q = 113 cm³/s, upstream P = 17.8×10^4 Pa, downstream P = 1.7×10^4 Pa).

magnitude as the velocity fluctuations found by McKinley et al. (1991) near the lip of a 4:1 axisymmetric contraction flow using similar viscoelastic solutions.

2.5.3 Polymer degradation

The permeation apparatus had several design features which had been incorporated to minimize the severe polymer degradation found by Chmielewski *et al.* (1990a) - see Chapter 4. These features included a reduction in the expansion and contraction ratios at the entrance and exit of the permeation cell, and an increase in the reservoir size, reducing the frequency in which a batch of fluid is cycled through the cell. Also, lower molecular weight PIBs were used in this investigation.

In order to assess the extent of polymer degradation the shear viscosity and storage modulus were measured on fluid samples taken from an 8 liter fluid batch after it had passed through an array several times. This information was used to determine the number of runs after which fresh batches of each fluid were required. Very little degradation was observed for all of the solutions used in this study. This is in contrast to the extreme amounts of chain scission found when care was not taken to minimize degradation (see Chapter 4).

2.5.4 Permeation of Newtonian fluids

The flow resistance of the test fluids passing through the arrays may be represented by the friction factor, f,

$$f = \frac{(-\Delta P)}{l} \frac{2a\rho}{G_o} \frac{\epsilon^3}{(1-\epsilon)} , \qquad (2.13)$$

where ρ is the fluid density, $-\Delta P$ is the pressure drop, ϵ is the void fraction of the bed, l is the bed length, a is the cylinder radius and G_o is the superficial mass flux. The Reynolds number, Re, is defined by,

$$Re = \frac{2aG_o}{\eta_o} \frac{1}{(1-\epsilon)} . \qquad (2.14)$$

In this study two Newtonian fluids, whose shear viscosities differ by nearly an order of magnitude, are used to obtain friction factor results for Reynolds numbers ranging from 0.001 to 0.3. Figure 2.11 shows no significant difference in the flow resistance of the Newtonian fluids in the square and hexagonal arrays at the void fraction level of 70 percent. The theoretical calculations of Sangani and Acrivos (1982) also predict little difference in the flow resistance for these two array types at this void fraction level. For example, the product of the friction factor and Reynolds number, which is inversely proportional to the transverse permeability, has a theoretically predicted value of 150 for the square array and 141 for the hexagonal array at a void fraction level of 70 percent.

Figure 2.11 reveals very good agreement between the experimentally measured friction factors for the two arrays and the theoretically predicted values over the range of Reynolds numbers studied. This agreement is also evidence of the insignificance of wall

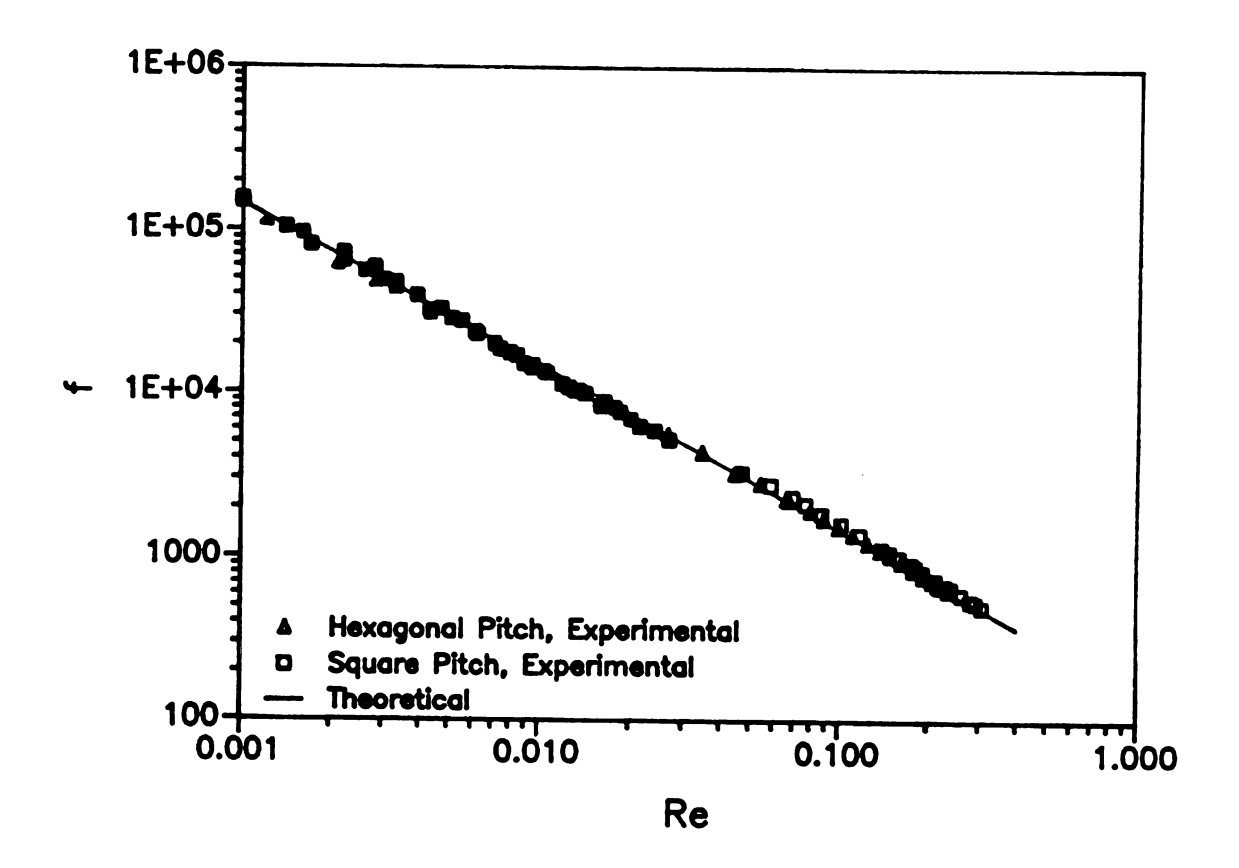


Figure 2.11 Friction factor vs. Reynolds number of two Newtonian PB liquids compared to the theoretical prediction of Sangani and Acrivos (1982) in square and hexagonal arrays (closed symbols represent the higher molecular weight PB).

and end effects.

2.5.5 Permeation of viscoelastic liquids

The departure of the friction factor from Newtonian behavior for the elastic liquids is shown in Figures 2.12 (a) and (b). The Re at which the onset of elastic effects occurs decreases with increasing molecular weight just as it does in the random packed bed experiments of Kulicke and Haas (1984). Also, at the same molecular weight the onset Re is consistently lower for the hexagonal pitch geometry than square pitch.

In order to scale out molecular relaxation time differences related to the PIB molecular weights, Figures 2.13 (a) and (b) present the relative fluid resistance, $f \cdot Re/(f \cdot Re)_N$, versus the Deborah number,

$$De = \lambda_1 \frac{V_o}{a} \quad , \tag{2.15}$$

where v_o is the superficial velocity. With this definition of De, a clear distinction may be made of the onset of viscoelastic effects between the two array types, 0.80 for the square pitch array and 0.35 for the hexagonal pitch array. The onset Deborah number, however, is independent of molecular weight. At sufficiently large Deborah numbers the relative flow resistance becomes independent of the Deborah number. This has also been observed by Kulicke and Haas (1984) and James and McLaren (1975) for the flow of polymer solutions through random beds of spheres. The asymptotic value of the

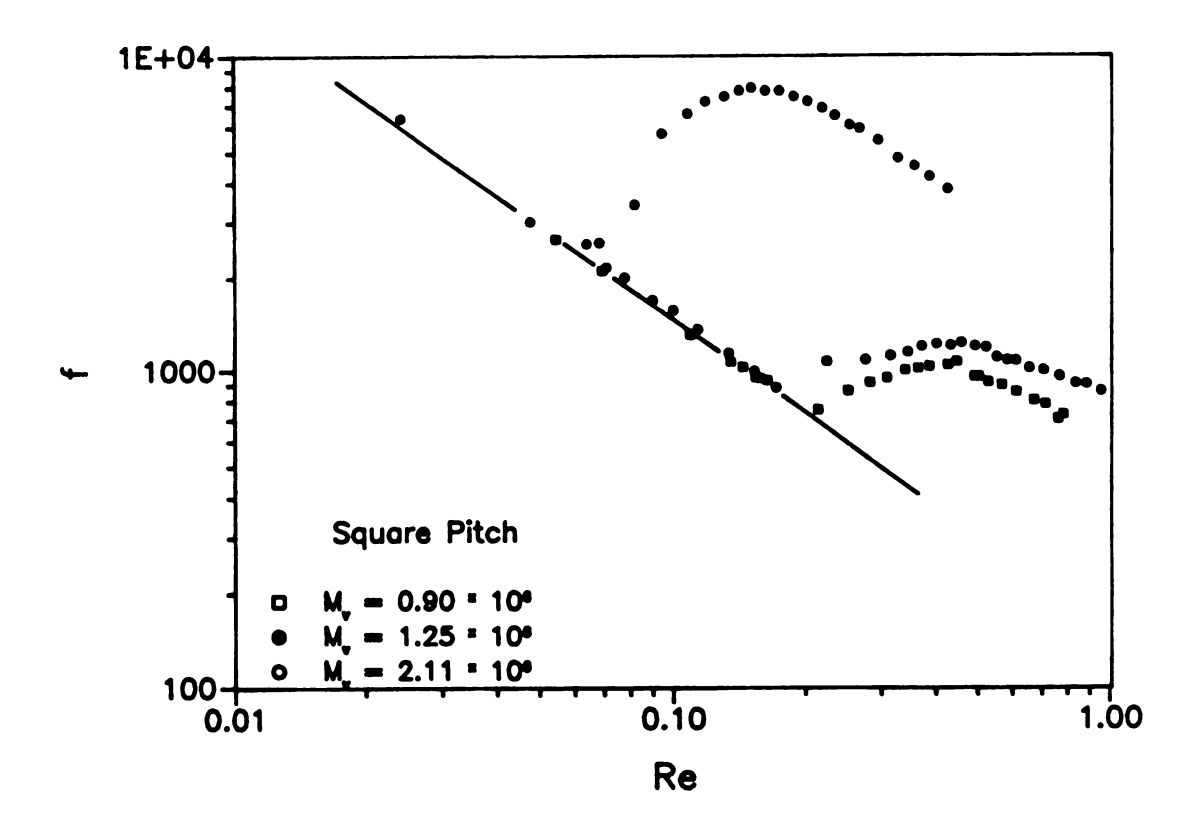


Figure 2.12 (a) Friction factor vs. Reynolds number of the PIB in PB solutions flowing through the square array.

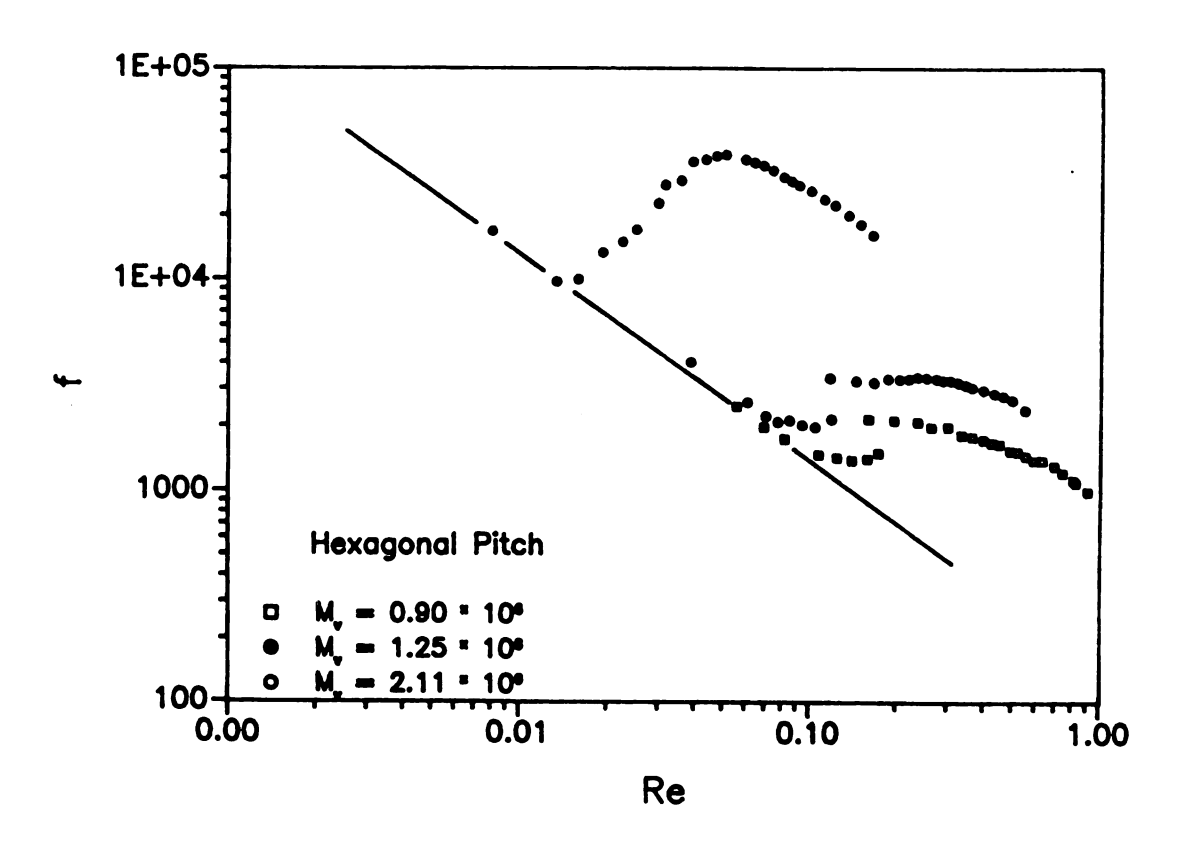


Figure 2.12 (b) Friction factor vs. Reynolds number of the PIB in PB solutions flowing through the hexagonal array.

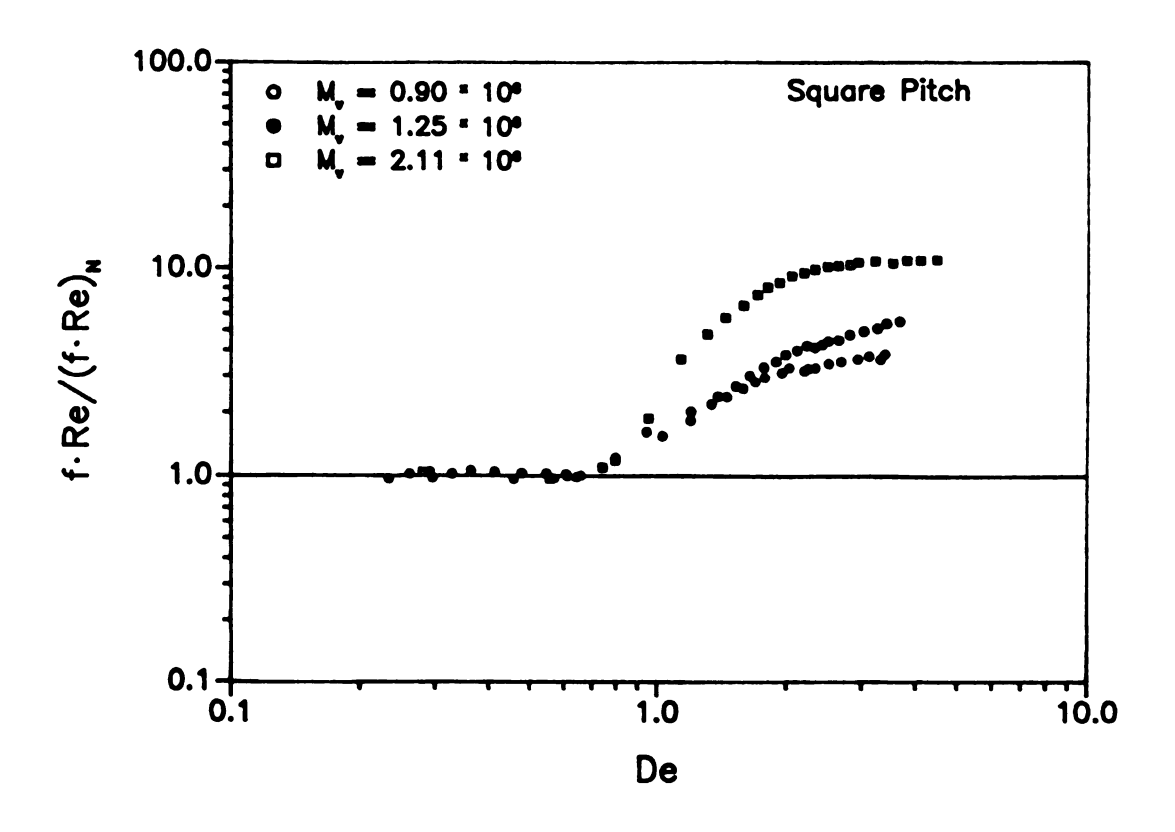


Figure 2.13 (a) Flow resistance vs. Deborah number for the PIB in PB solutions flowing through the square array.

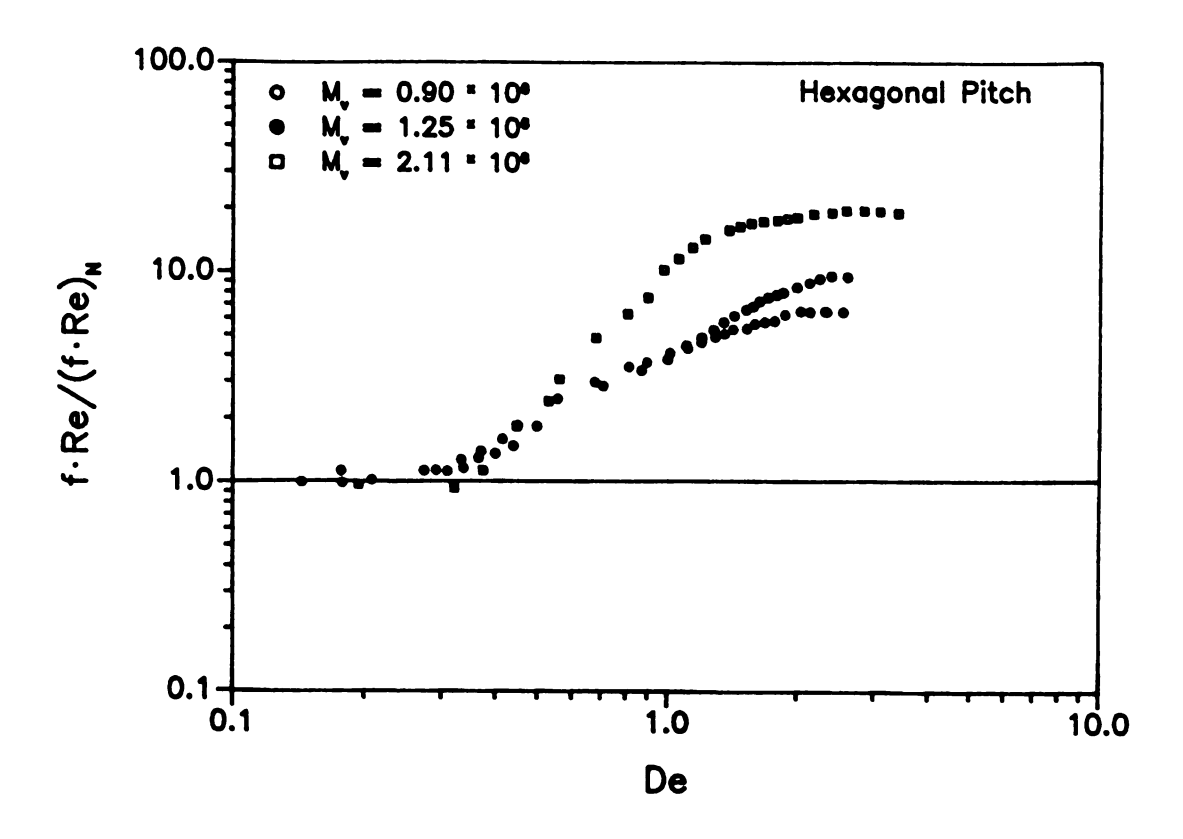


Figure 2.13 (b) Flow resistance vs. Deborah number for the PIB in PB solutions flowing through the hexagonal array.

resistance ratio increases with increasing molecular weight in both arrays, but is consistently lower in the square array than the hexagonal array at comparable molecular weights. Figure 2.14 is a plot of the numerical value of the asymptotic ratio versus molecular weight of the polymer solute for each array. In both arrays the value of the flow asymptote scales linearly with the molecular weight,

$$\frac{f \cdot Re}{f \cdot Re|_{N}}|_{De>>1} \propto M_{N} , \qquad (2.16)$$

just as the apparent Trouton ratio of these solutions does (Figure 2.5 (b)). This is reasonable because the kinematics of the flow of polymer solutions transverse to cylinder arrays is dominated by planar extension at high Deborah numbers. In planar extensional flows, as in uniaxial extensional flows, the extensional viscosity of a FENE model fluid at high Deborah numbers is proportional to L^2 , and thus to the molecular weight,

$$\frac{\eta_{g}-2\eta_{g}}{\eta-\eta_{g}} \ll L^{2}-1 \ll M_{W} . \qquad (2.17)$$

Hence,

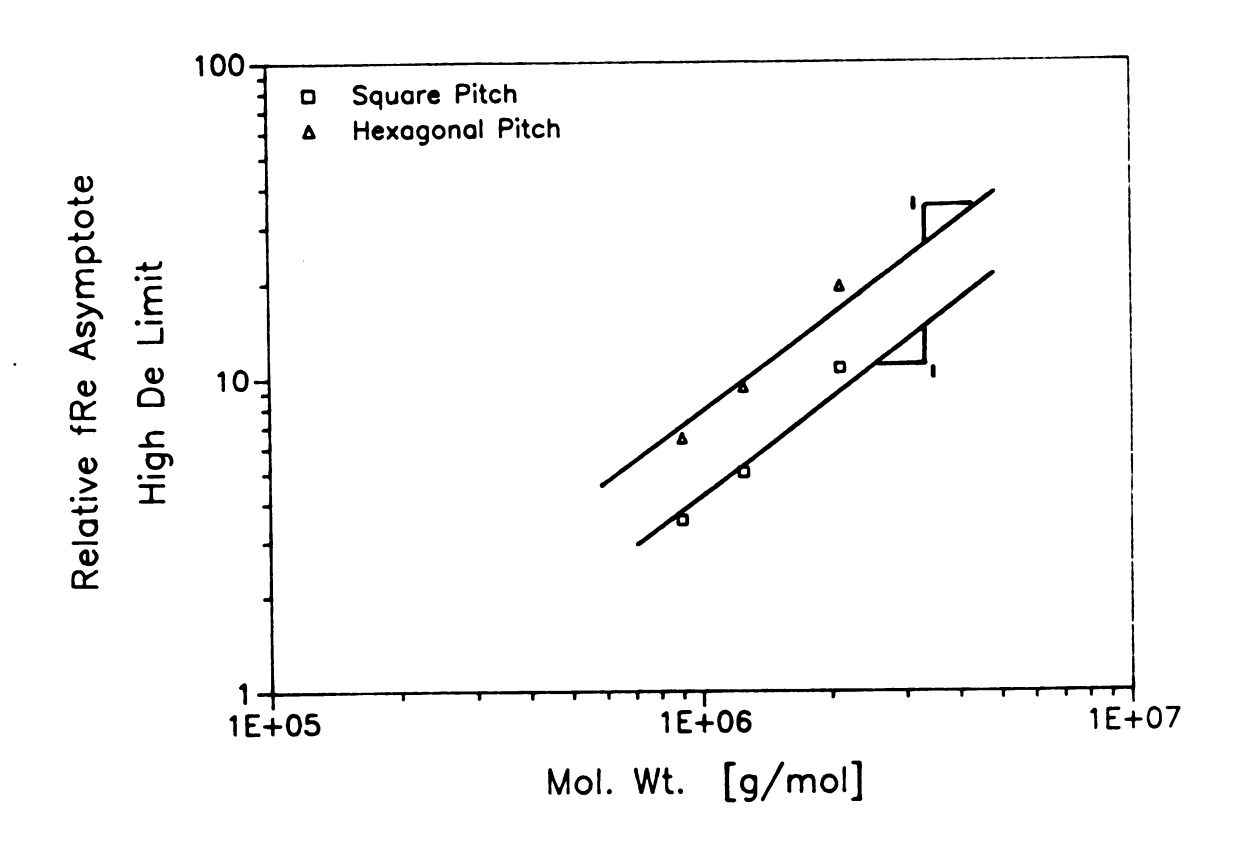


Figure 2.14 The high Deborah number flow resistance asymptotes as a function of molecular weight for both the square and hexagonal pitch arrays.

$$\frac{f \cdot Re}{f \cdot Re|_{N}}|_{De>>1} \propto \frac{\eta_{B} - 2\eta_{B}}{\eta - \eta_{B}} . \qquad (2.18)$$

This relationship between the asymptotic values of the relative flow resistance and the solution molecular weight comes about as a result of differences in the degree of extensibility of the polymer molecules. For theta systems the square of the extensibility is proportional to the molecular weight (Eqs. 2.9-2.11). These results also indicate that even though fiber spinning is an axisymmetric extensional flow, the results are quite relevant to the planar geometry of flow through cylinder arrays.

Figure 2.15 shows the flow resistance results for the PIB/Decalin solution in both the square and hexagonal pitch cylinder arrays. Here the Deborah number is defined with $\lambda_1(\hat{\gamma})$,

$$\lambda_1(\dot{\gamma}) = \frac{G'(\omega)}{\omega G''(\omega)}|_{\omega \to \dot{\gamma}}. \qquad (2.19)$$

These data show a plateau at a flow resistance less than 1 for both the square and hexagonal arrays for Deborah numbers in the range of 0.3 to 1. We were not able to work at sufficiently low Deborah numbers to observe Newtonian behavior. This reduction in the flow resistance was not observed for the Boger liquids and is a result of the highly shear thinning nature of the PIB/Decalin solution. As the Deborah number is increased further, the flow resistance increases, and at De = 3 for the hexagonal array

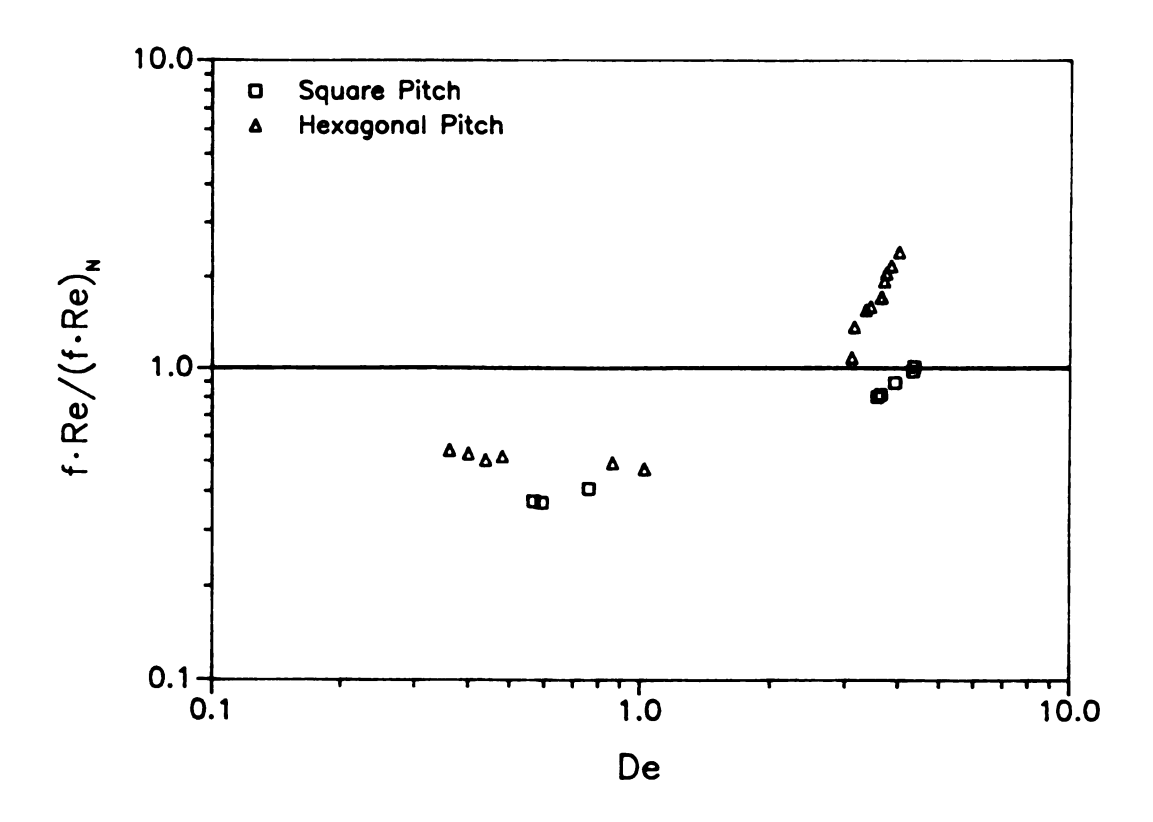


Figure 2.15 Flow resistance vs. Deborah number for the PIB in decalin solution flowing through both the square and hexagonal array.

and De = 4.2 for the square array the flow resistance crosses the relative f·Re axis at

1. This enhancement in the flow resistance at high Deborah numbers is a result of
extensional viscosity effects dominating the shear viscosity effects. This is similar to the
fiber spinning results where it was found that the averaged extensional viscosity of the
PIB/Decalin solution increased with increasing extension rate.

2.6 Conclusions

The effect of varying polymer extensibility on the dynamics of polymer solutions flowing transverse to cylinder arrays is studied. The polymer extensibility of each solution is controlled through the molecular weight of the polymer solute. Average extensional viscosity measurements affirm that increasing molecular weight corresponds to increasing polymer extensibility. The apparent Trouton ratio at a fixed stretch rate scales linearly with the molecular weight. The pressure drop of non-shear thinning elastic liquids flowing through both square and hexagonal pitch cylinder arrays at a void fraction of 70 percent is enhanced at onset Deborah numbers of 0.8 and 0.35 respectively. At high values of Deborah number the relative flow resistances in both arrays become independent of the Deborah number. This was observed after care was taken to avoid degradation of the polymer. The magnitude of the high Deborah number flow resistance asymptote scales linearly with the molecular weight, and hence correlates well with the apparent Trouton ratios measured.

Chapter 3

THE KINEMATICS OF VISCOUS AND VISCOELASTIC LIQUID FLOWS WITHIN ARRAYS OF CIRCULAR CYLINDERS

3.1 Summary

The kinematics and hydrodynamic stability of viscous and viscoelastic liquid flows transverse to periodic arrays of circular cylinders has been studied at Reynolds numbers less than 0.5. Both streak photography and laser Doppler velocimetry were used to observe flow transitions resulting from fluid elasticity in square and hexagonal pitch arrays at a porosity level of 70 percent. Below an onset Deborah number, the flow of a non-shear thinning elastic liquid was steady, spatially periodic, and identical to the experimentally observed Newtonian kinematics and Stokes flow simulations. LDV measurements made above the onset Deborah number reveal flow unsteadiness in both array types. Particle path asymmetry is also observed above the onset Deborah number. The onset Deborah number corresponds approximately to the onset of elastic effects in flow resistance measurements found in the previous chapter: 0.70 for the square array

and 0.25 for the hexagonal array. Results with a shear thinning liquid underline the elastic origin of the instability observed. Also, these results indicate that any attempt to predict flow resistance increases must describe the viscoelastic transition to unsteady flow.

3.2 Introduction

The question addressed in this chapter is whether fluid elasticity, resulting from the dissolution of small amounts (0.2 wt. %) of a high molecular weight polymer into a viscous liquid, affects the flow kinematics within periodic arrays of circular cylinders. This issue is examined with two experimental techniques - streak photography and laser Doppler velocimetry (LDV).

The study of how velocity fields are affected by fluid rheology is important to both the experimentalist, who uses this information to evaluate flow dynamics, and to the theorist, who uses the data to evaluate constitutive models and computational methods. The flow of non-Newtonian liquids past a cylinder provides a good example of this. Using tracer dyes, Manero and Mena (1981) visualized the slow flow (Re < 0.01) of shear thinning elastic liquids around circular cylinders. They found that in the range 0.2 < De < 1 the streamlines shifted downstream from the symmetric pattern characteristic of Newtonian fluids. This was in qualitative agreement with the perturbation calculations of Mena and Caswell (1974), using an Oldroyd constitutive model. At De ~ 1 there was no displacement in streamlines, and for De > 1 the streamlines moved upstream of

the Newtonian pattern.

In the present study another flow visualization method, streak photography, is used to qualitatively examine the flow field within arrays of cylinders. In this method small particles in the fluid reflect light from a sheet of light illuminating the flow field. The flow is then photographed at long exposure times so that the paths of several particles show up as streaks on the film. This technique has been used extensively by several researchers to visualize flow pattern changes and instabilities, resulting from fluid elasticity, in axisymmetric entry flows through circular tubes. For example, Nguyen and Boger (1979) present a series of photographs revealing several flow transitions with increasing Deborah numbers for non-shear thinning, elastic fluids - Boger fluids - flowing through a 7.675:1 axisymmetric contraction. At sufficiently low Deborah numbers (~ 0.5), the flow pattern was similar to the Newtonian fluid pattern, having a small secondary vortex in the corner of the upstream tube. As the flow rate increased so did the size of the vortex, beyond what is seen with Newtonian liquids. At De ~ 3 the vortex continued to grow and became asymmetric. At De ~ 6 the asymmetric vortex began to rotate around the tube. Finally, at De ~ 15 the flow became chaotic.

In addition to flow visualization, laser Doppler velocimetry (LDV) has been used to obtain quantitative local velocity measurements within cylinder arrays. LDV is an experimental technique which measures point velocities within a fluid flow by detecting the Doppler shift of light scattered from solid particles in the fluid. Presumably these particles are small enough so that their velocity corresponds to the local fluid velocity.

Since this technique's introduction by Yeh and Cummins (1964), LDV has been

widely used on both laminar and turbulent flows of gases and Newtonian liquids. The use of LDV on flows of viscoelastic liquids, however, has not been as extensive. An LDV study particularly relevant to this investigation has been made by Lawler *et al.* (1986). They examined the velocity field and flow transitions of an elastic, non-shear thinning polyisobutylene solution (a Boger fluid) in a 4:1 axisymmetric contraction flow. For De < 0.8 the flow was steady and identical to the predicted Newtonian flow field, but at De = 0.8 the flow became time periodic with a fluctuating tangential velocity component. At De = 1.2 the flow again became time independent, but was no longer identical to the Newtonian velocity field. It is interesting that the flow transition at De = 0.8 is lower than the onset Deborah number for the appearance of large corner vortices, indicating that the LDV technique is sensitive to flow transitions, particularly temporal transitions, which otherwise could not be detected by more conventional flow visualization techniques.

The work presented here examines the kinematics of viscous and viscoelastic liquids in periodic arrays of circular cylinders. The flow field is explored by both streak photography and by laser Doppler velocimetry. LDV provides point velocity measurements of both viscous and viscoelastic liquids in cylinder arrays for comparison with numerical simulations, while streak photography provides global comparisons of flows at Deborah number of O(1) with the Newtonian flow field. In both the square and hexagonal arrays a flow transition is observed for the viscoelastic liquid near the Deborah number where onset of elastic effects is observed in the flow resistance data.

3.3 Laser Doppler velocimetry (LDV)

3.3.1 Basic principles

A dual beam, single component LDV system is used in this study, and is shown schematically in Figure 3.1. Plane polarized light, emitted from a 35 mW He-Ne laser at a wavelength of 632.8 nm, is split into two beams of equal intensity and focused by a transmitting lens. The receiving optics and photomultiplier are set up in the forward scatter mode, directly in line with the transmitting lens. It is in this direction that the intensity of scattered light, resulting from small particles moving through the beam intersection, is the greatest. Velocity measurements are made in the ellipsoid, known as the "measuring volume", formed by the beam intersection and it is in this location, between the transmitting and receiving lenses, that the permeability cells were placed.

The simplest and most widely used explanation of the operation of the dual beam LDV system is based on the fringe model. This model avoids reference to the Doppler shift effect and yet provides many correct results in terms of the velocity measurement. It breaks down, however, in the calculation of predicted signal intensity of light scattered from the measuring volume.

The fringe model is based on the interference of intersecting waves at the measuring volume, producing a fringe pattern with spacing, d_f,

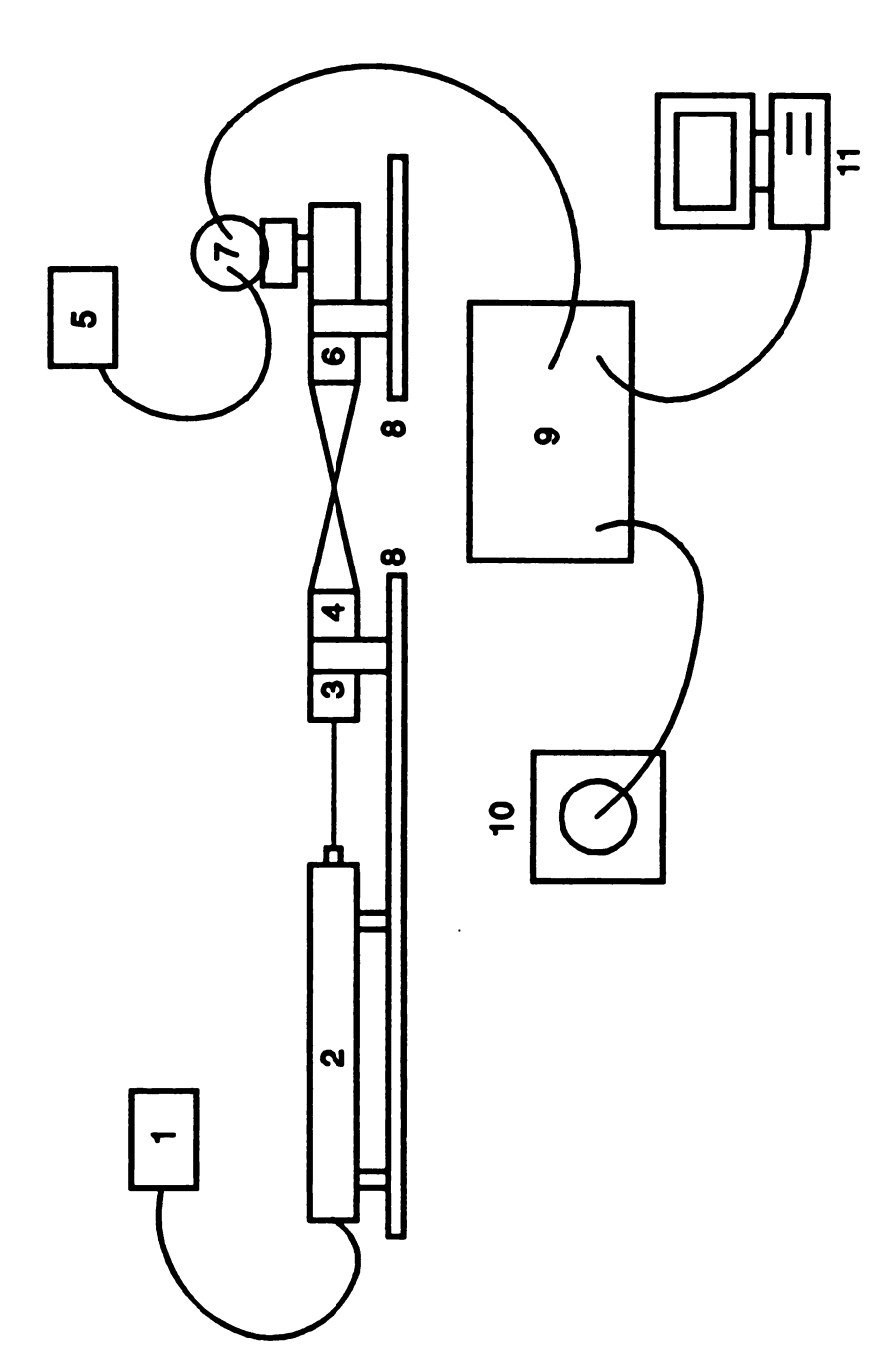


Figure 3.1 Schematic of laser Doppler velocimeter system (components are identified in Table 3.1).

Table 3.1 Components of the laser Doppler velocimeter system shown in Figure 3.1.

Component	TSI Model	Description
1	9126-255	Laser power supply
2	9126-105A	35 mW He-Ne laser, $\lambda = 632.8$ nm
3	9115-2	Beam Splitter, 50 mm separation
4	9118	Transmitting lens, f = 250 mm
5	9165	Photomultiplier power supply
6	9118	Receiving lens, f = 250 mm
7	9160A	Photomultiplier
8	9126, 9121	Optical rails
9	1980	Signal Processor, 100 MHz clock
10	465 M	Portable Oscilloscope
11	*****	Apple IIe computer

$$d_f = \frac{\lambda}{2\sin(\kappa)} \quad , \tag{3.1}$$

where λ is the wavelength of the laser light and κ is the half angle of the intersecting beams ($\kappa = 5.71^{\circ}$). In the present system the fringe spacing is 3.18 μ m, resulting in 64 fringes within the measuring volume. These fringes are set in planes perpendicular to the plane in which the beams lie, and run parallel to the line bisecting the angle formed by the beam crossing. Figure 3.2 shows a schematic of the ellipsoid and fringe pattern at the beam intersection. Here the beams cross in the x-z plane and the z axis lies along the bisector of the angle formed by the beams.

The velocity measurement of fluid flowing through the measuring volume relies on small solid particles, traveling with the flow, to scatter light. As a particle moves through the fringe pattern, past the light and dark bands, it reflects light with an oscillating intensity. This reflected light is picked up by the photomultiplier and converted into an electronic signal. The signal, shown in Figure 3.3, contains a mean low frequency component known as the pedestal and a sinusoidal component which oscillates at the Doppler frequency (ν_D). During processing of the signal, the pedestal is usually removed, leaving ν_D which is proportional to the velocity,

$$v_D = \frac{|u|}{d_r} \quad . \tag{3.2}$$

.

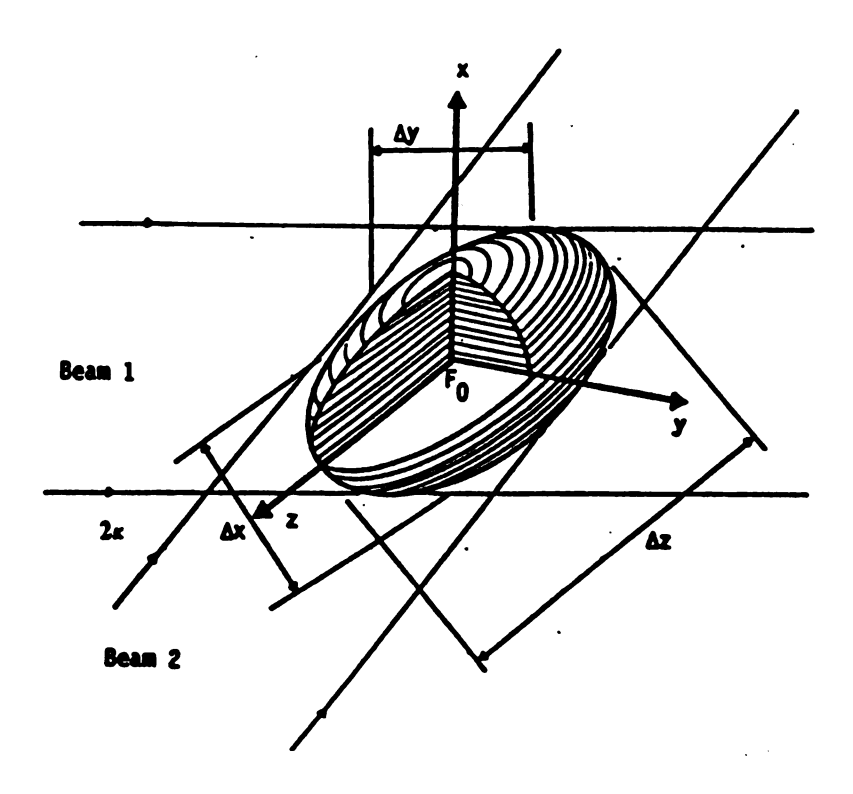


Figure 3.2 Measuring volume and fringe pattern formed by the beam intersection. The beams intersect in the x-z plane and the z axis follows the bisector of the angle of beam crossing (Dabir, 1983).

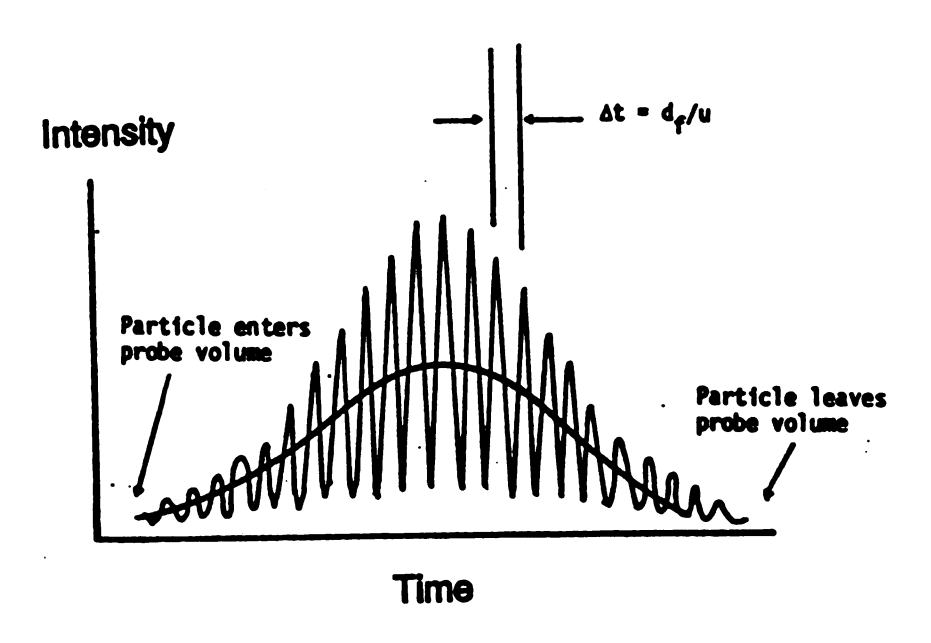


Figure 3.3 A typical signal from the photomultiplier (Dabir, 1983).

Hence, calculated fluid velocity is based solely on the measured Doppler frequency, the wavelength of laser light and the half angle of the beam crossing. The dual beam system measures only velocity components perpendicular to the plane of the fringes (the x direction in Figure 3.2) since the other components represent particle motion within a fringe plane, producing no oscillating signal.

The absolute value in Eq. 3.2 indicates this technique's inability to determine flow direction. A particle traveling through either end of the measuring volume at the same speed will result in an identical signal. In flows where the local direction of fluid motion is unknown a technique called frequency shifting is employed. Instead of the measuring volume containing a stationary interference pattern, the frequency of one of the transmitted beams is shifted by v_s , causing a moving wave-like fringe pattern. Thus, particles in the measuring volume moving in the same direction as the fringes will result in experimentally measured frequencies less than v_s , while particles moving in the opposite direction will result in frequencies greater than v_s .

3.3.2 Experimental LDV system

Figure 3.1 shows the dual beam Thermo-Systems Inc. (TSI) LDV system used in this study. Each of the individual components is listed and described in Table 3.1. All experiments are performed in the forward scatter mode and frequency shifting is not employed. The light source is a 35 mw He-Ne laser, emitting light at a wavelength of 632.8 nm. The major optical components consist of a beam splitter, which divides the incident beam into two equal intensity beams separated by 50 mm, and transmitting and

receiving lenses, each having a focal length of 250 mm. This lens system produces a beam half angle of 5.17° and an ellipsoid measuring volume with dimensions: $\Delta z = 1.9$ mm, $\Delta x = 0.18$ mm and $\Delta y = 0.18$ mm (see Figure 3.2). As shown earlier by Eq. 3.1, the fringe spacing is 3.18 μ m, resulting in 64 fringes across the measuring volume. Also, the industrial grade solvents used in this study are sufficiently contaminated with dust and other forms of dirt that seeding the flow is unnecessary. The velocities measured in this study typically are in the range of 0.5 to 5 cm/s, which correspond to Doppler frequencies of approximately 1.6 to 16 kHz.

The processing of the Doppler signal begins at the photomultiplier which picks up photons from the receiving optics and converts them into a voltage signal. The voltage signal is then sent to a TSI model 1980 signal processor where it passes through an input conditioner and a timer. The input conditioner amplifies and filters the signal with 1 kHz and 10 kHz (or 100 kHz) high and low pass filters. The conditioner also contains a Schmitt trigger. If the signal amplitude is greater than 50 mV the trigger is activated, converting the sinusoidal wave into a square wave. Otherwise, the output is not updated. The timer's function is to measure the length of the envelope containing N cycles from the Schmitt trigger; the numbers of cycles per burst, N, is set externally and for this study is 8. The timer also measures the length of an envelope N/2 cycles long. If the average signal frequency of the first N/2 cycles is not within 5 percent of that of the N cycles then the data point is rejected and the system is reset without updating the output. Otherwise, the frequency is latched to output.

3.3.3 LDV measurement difficulties

The LDV measurements, made on both the viscous and viscoelastic liquids within the cylinder arrays, suffered from low data rates. Data rates of approximately 1 to 5 Hz were obtained. This is in comparison to rates of 100 to 500 Hz which are necessary in order to obtain temporal information about the velocity. As a result, sampling was limited to the "handshake" mode of data collection. Typically, at data rates of 100 Hz, data can be collected every 100 ms with confidence that every data point is independent. With a data rate of 1 Hz and sampling every 100 ms, however, every tenth data point is independent. The other nine represent the same point because the previous signal will remain in memory until a new point replaces it. In the handshake mode of operation data points are sampled only as frequently as they arrive. Thus, making accurate velocity measurements of steady flows was not a problem. Obtaining temporal information from unsteady flows, however, was not possible as a result of the low data rates.

During this investigation, sets of 256 data points were sampled at each location in the flow field; at data rates of 1 Hz this process took more than 4 minutes per set. A TSI data reduction program, running on an Apple IIe, collected the frequencies from the signal processor, calculated the corresponding velocities and presented a statistical evaluation of the data which included the probability distribution function, the mean velocity and standard deviation. Collecting data this way worked well since the standard deviations of the data sets were less than 1 percent of the mean values for the stable flows.

The precise cause of the low data rates is unknown. What is known is that the

low rates were not a result of infrequent Doppler bursts, but rather small signal amplitudes. The amplitude of the electronic signal received from the photomultiplier was usually lower than the 50 mV necessary to activate the Schmitt trigger. Thus, the timer infrequently received data to compare and latch to output. This occurred even though the signal gain was set at maximum. The cause of this low output amplitude was initially thought to be the result of a faulty photomultiplier. However, a TSI inspection has revealed that this is not the case. Furthermore, the entire LDV system was tested by measuring the velocity of water stirred in a glass beaker. Good Doppler signals were obtained with data rates of 100 Hz. Seeding the flow with spherical 5 micron Nylon particles was also tested. This appeared to slightly increase the frequency of Doppler bursts, but had no effect on the signal amplitude.

The most likely cause of the low signal intensities is optical inhomogeneities in the Plexiglas windows of the permeability cells. Because the cylinders are tightly press fit into the windows, much residual stress remains in the material. This is confirmed by the asymmetric stress patterns observed in the Plexiglas when they are examined between two polarizing lenses. These patterns are the result of local index of refraction differences caused by residual stresses. Thus, light exiting the permeability cell is scattered by the Plexiglas window, reducing the intensity of light picked up by the receiving optics.

3.4 Experimental

3.4.1 Test fluids

Three test fluids were used in this study: a Newtonian fluid, a non-shear thinning, elastic fluid (a Boger fluid) and an elastic shear thinning fluid. The Newtonian liquid is a pure polybutene (PB), Amoco grade H25, whose material and rheological properties can be found in the preceding chapter. The Boger liquid is a polyisobutylene/ kerosene/ polybutene mixture, having the following composition by weight: 0.25 % PIB/ 7 % kerosene/ 92.75 % PB H25. The PIB is a 4 to 6 million molecular weight polymer purchased from Aldrich Chemical Co. This solution is a Boger fluid similar to the M1 standard (Sridhar, 1990) with the shear viscosity nearly constant over shear rates up to 10 s^{-1} (see Figure 3.4). The shear viscosity, shown in Figure 3.4, is 2.8 Pa·s at 25 °C and the relaxation time, λ_1 , calculated from the quadratic region of the storage modulus vs. frequency curve (see Figure 3.5) is 0.86 s. The shear thinning liquid is a 2 wt.% PIB in decalin solution whose rheological properties are presented in the preceding chapter.

3.4.2 Apparatus

The flow loop and permeability test cells have been described in detail in the previous chapter, and only the important features of the apparatus are discussed here. A schematic of the apparatus is shown in Figure 2.7. Test fluid is pumped via a peristaltic pump from the holding tank into the liquid reservoir. From here the test fluid

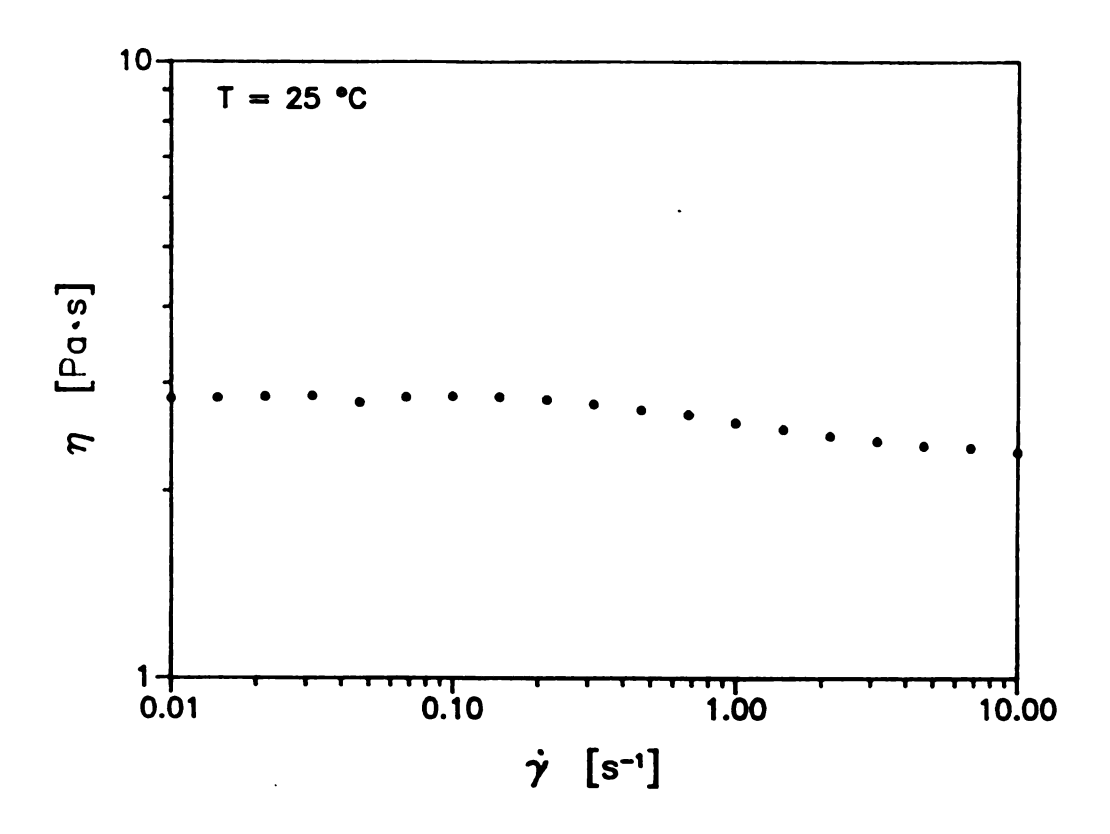


Figure 3.4 Steady shear viscosity of a 0.25 % PIB/PB solution at 25 °C.

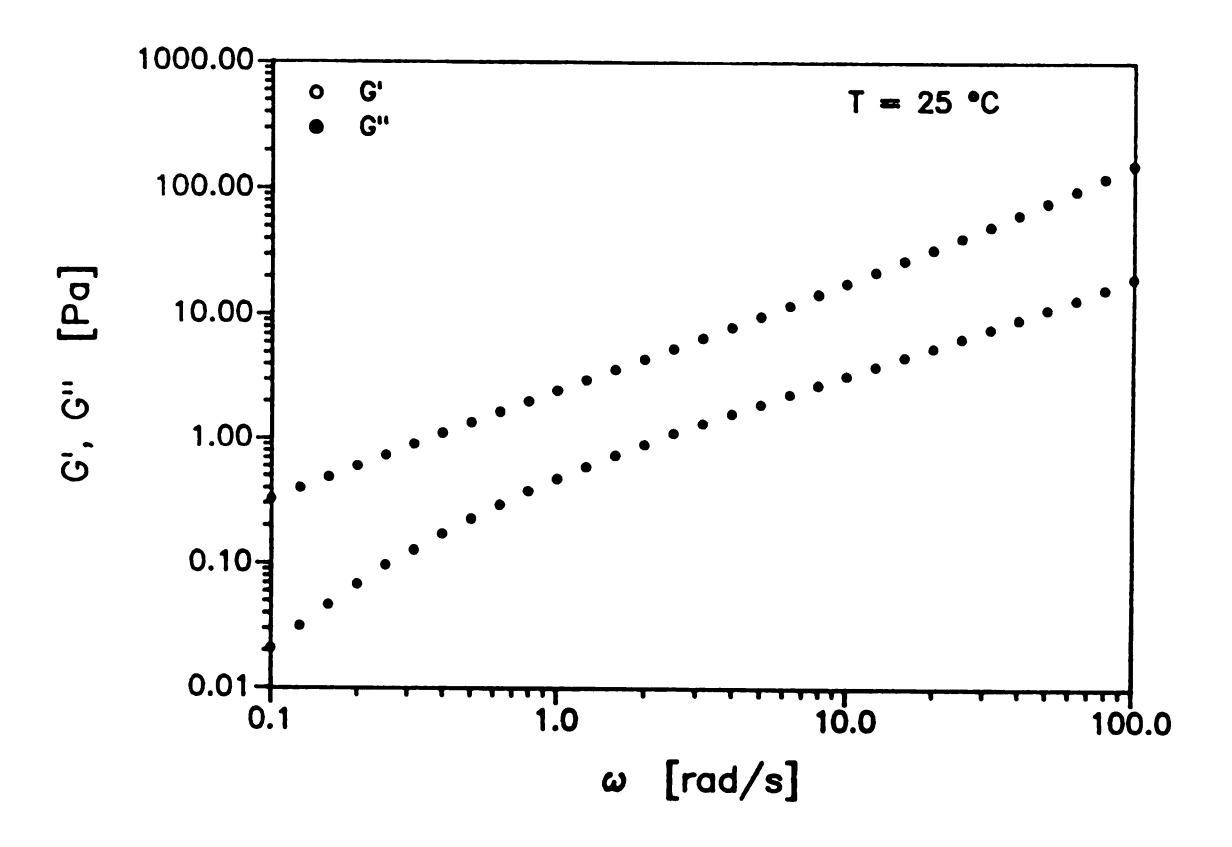


Figure 3.5 Linear viscoelastic properties of a 0.25 % PIB/PB solution at 25 °C.

either flows freely or is forced by regulated nitrogen pressure through the cells. Flow rate measurements are made by weighing fluid samples collected over time or by monitoring the reservoir liquid level with time. Pressure transducers on either side of the cylinder array measure the mean pressure drop across the bed as shown in Figure 2.7.

The kinematics of flow transverse to a square array and to a hexagonal array of circular cylinders is studied. Each array has a void fraction of 70 percent and is composed of acrylic cylinders (radius = 0.238 cm) arranged as shown in Figure 2.9. Localized velocity measurements within the cylinder arrays are made by LDV and have been discussed above.

3.4.3 Streak photography

The flow patterns are mapped by streak photography. This is done by passing a light beam (from the 35 mW laser used in the LDV experiments) through a cylindrical lens to form a thin sheet of light. This sheet is then reflected off a surface coated mirror and passed through a window in the top of the permeability cell, illuminating the flow field. The light sheet lies perpendicular to the axes of the cylinders and in the plane of the 2 dimensional flow. Pictures taken with a 35 mm camera, using a time exposure of 1.5 seconds, capture the path of 50 μ m silicon carbide particles seeded (0.033 grams per liter fluid) in the flow.

3.5 Validation of experimental technique

3.5.1 Stokes flow simulation

Finite element simulations have been carried out for two dimensional Stokes flow in the domains shown in Figure 3.6. These domains represent repeat units of the periodic square and hexagonal cylinder arrays used in the experimental section of this chapter. Both the x and y coordinates are scaled with the cylinder radius and the velocity with the superficial velocity. Over the entire boundary of both domains the y component of the velocity is zero. This is the result of no-slip at cylinder surfaces and symmetry along all other boundaries. The x component of the velocity is set to zero only at the cylinder surfaces. Otherwise, it is specified at the upstream portion of the domain boundary (x = -1.62 and x = -3.01 for the square and hexagonal pitch geometries respectively). The periodicity of both geometries requires that the x velocity component along the downstream domain boundary be equivalent to the upstream boundary. This condition is satisfied by iterating; the boundary velocities upstream are replaced by calculated downstream velocities until convergence is attained. The results of the simulations are shown in Figure 3.7. As expected for linear fluids with periodic boundary conditions, the streamlines in both the square and hexagonal arrays are symmetric around the cylinders.

3.5.2 Newtonian liquid flow visualization

The flow patterns for the pure polybutene in both the square and hexagonal arrays

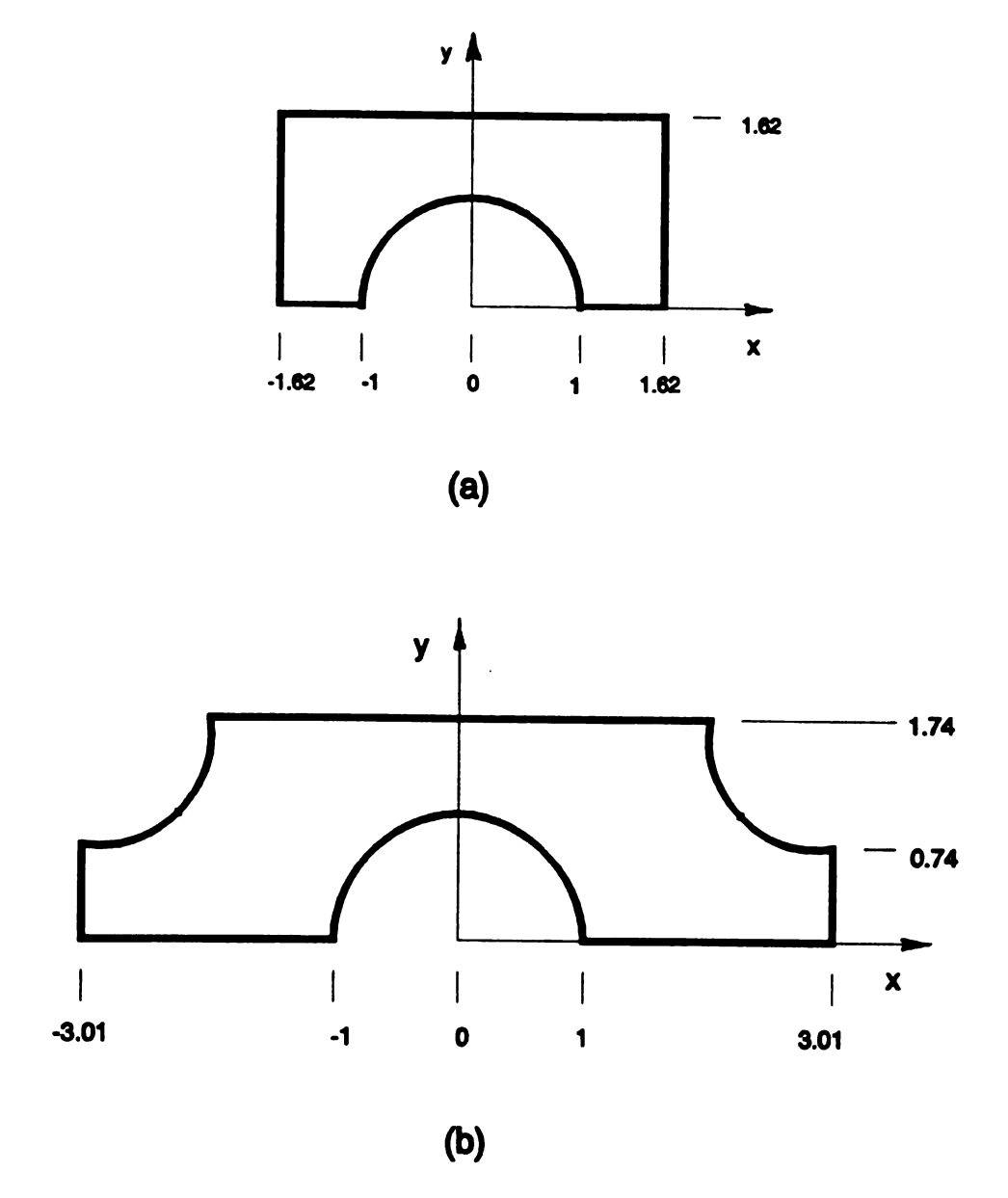
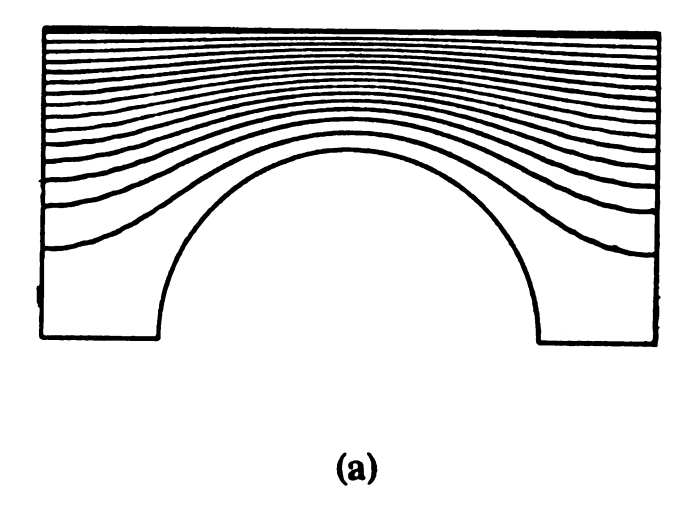


Figure 3.6 Geometric domains used for the Stokes flow simulations (a) square array and (b) hexagonal array.



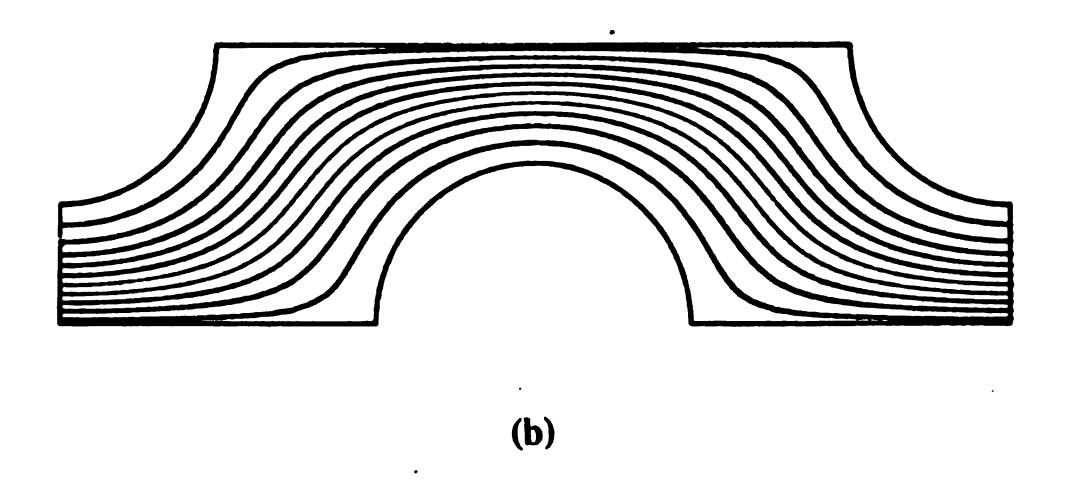


Figure 3.7 Streamline output from the Stokes flow simulations (a) square array and (b) hexagonal array.

at Re = 0.027 and Re = 0.013 respectively, are shown in Figure 3.8. The fluid is travelling from right to left. The particle paths in the photographs are symmetric, reflecting the periodicity of the arrays, and are identical to the streamline calculations in Figure 3.7. In the square array no streaklines are visible in the space between cylinder stagnation points because of extremely low velocities (compared to the bulk flow) between rows of cylinders. Streak photographs for Reynolds numbers up to 0.5 in both arrays have also been taken but are not presented here. These photos show the same patterns as those in Figure 3.8. Also, flow resistance measurements for these tests are in good agreement with Darcy's law (see Chapter 2), and at no time did the flow exhibit array instability.

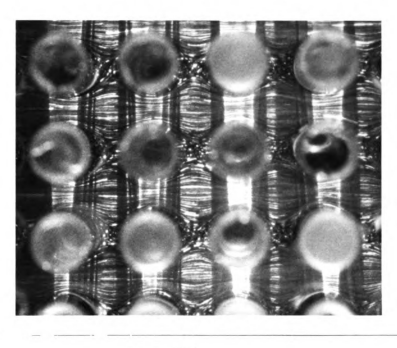
3.5.3 Newtonian liquid LDV measurements

The results of LDV measurements taken along lines of geometric symmetry, y = 1.62 and y = 1.74 for the square and hexagonal arrays respectively, are shown in Figure 3.9. Along these lines the geometric symmetry requires that the y component of the Velocity vanish at steady state. Again, good agreement is found between the numerical simulations and the velocity measurements.

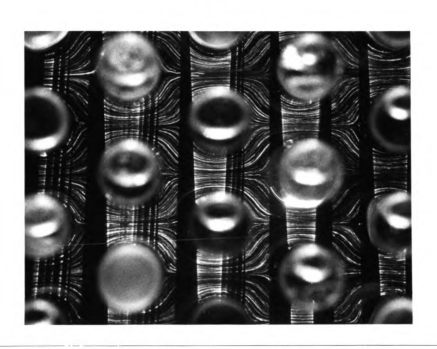
3-6 Elastic liquid results and discussion

3.6.1 Flow visualization on the PIB/PB liquid

Figures 3.10 (a)-(e) and 3.11 (a)-(d) show a series of streak photographs, each



(a)



(b)

Figure 3.8 Streak photographs for a Newtonian polybutene liquid in the cylinder arrays at a void fraction of 70 percent (flow from right to left) (a) square array, Re = 0.027 and (b) hexagonal array, Re = 0.013.

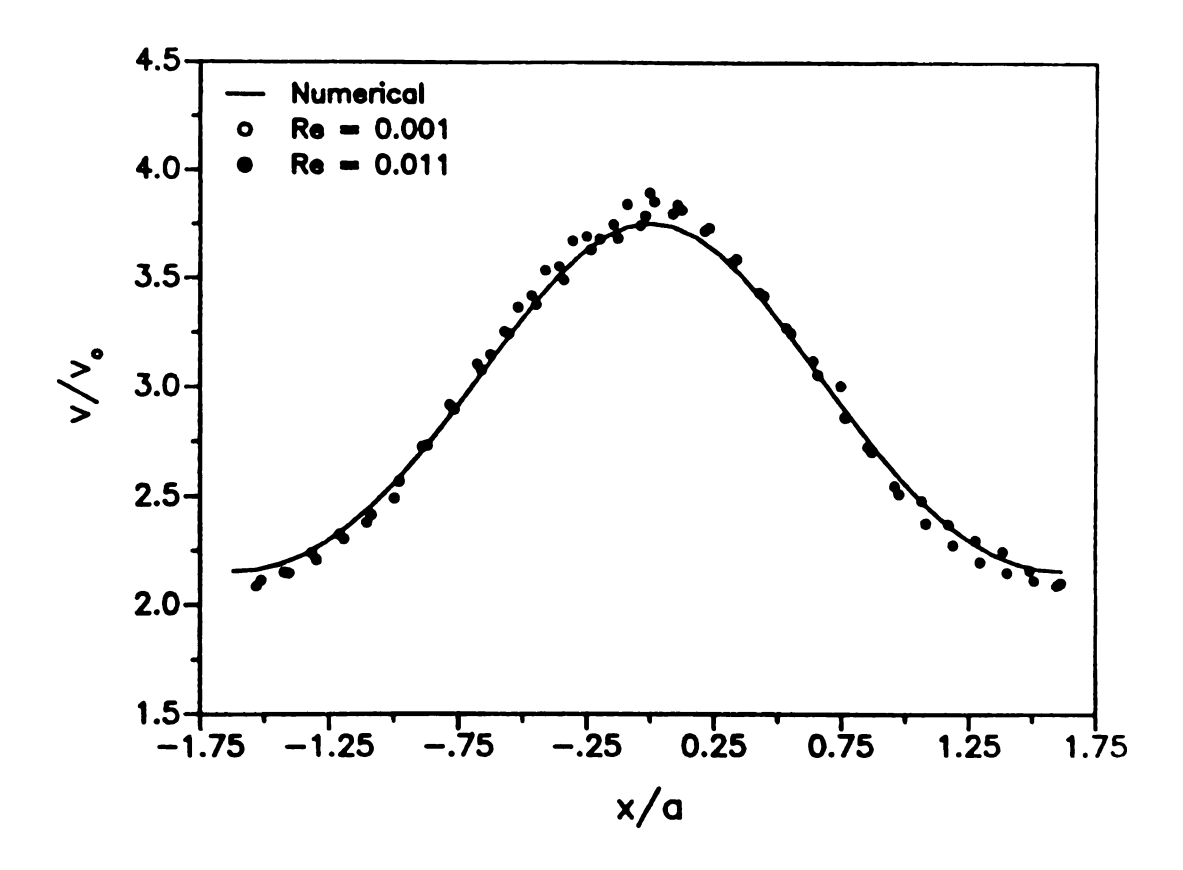


Figure 3.9 (a) LDV measurements and the Stokes flow prediction for the inelastic Newtonian fluid in the square array along y = 1.62.

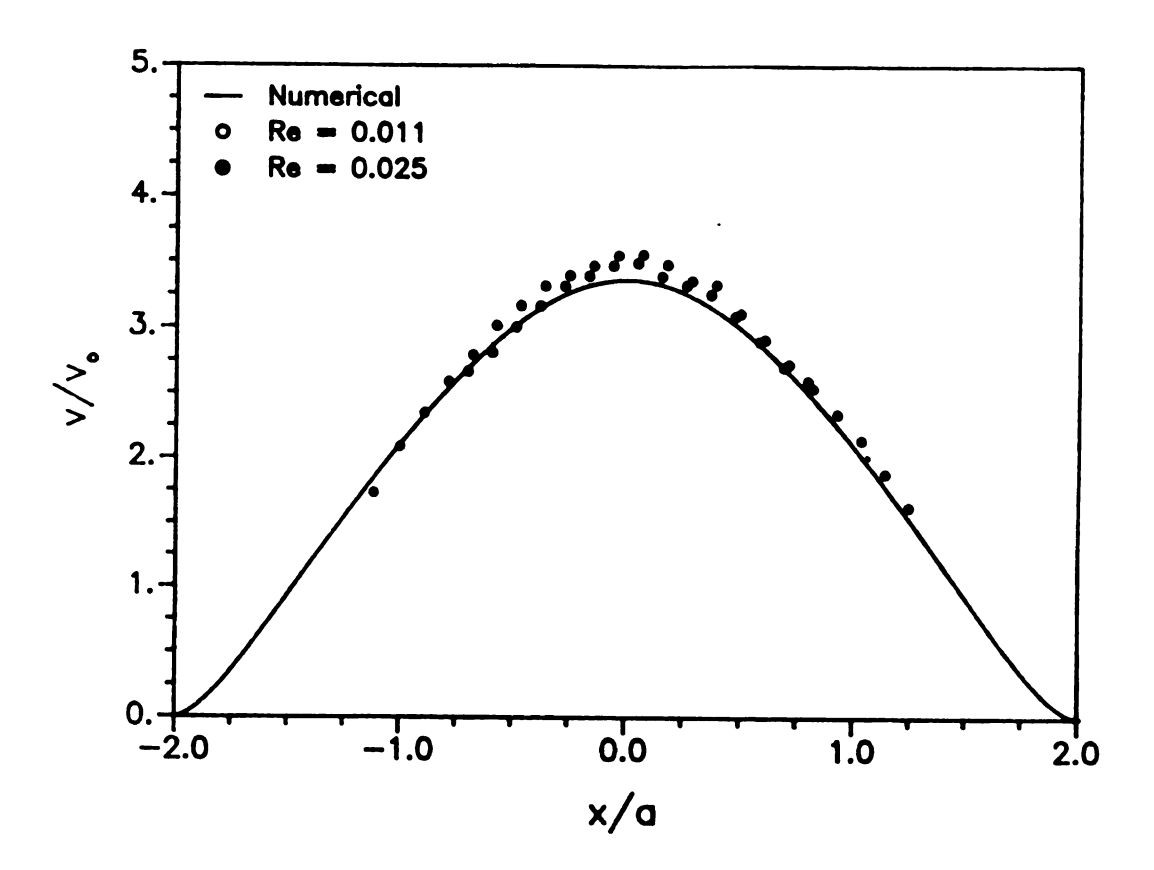


Figure 3.9 (b) LDV measurements and the Stokes flow prediction for the inelastic Newtonian fluid in the hexagonal array along y = 1.74.

at a consecutively higher De, of the PB/PIB solution flowing through the square and hexagonal arrays. In all photographs the fluid is travelling from right to left and the Reynolds number is less than 0.5. The relative flow resistances, corresponding to the flow situation in each photograph, are given in **Figure 3.12**. The flow resistance data are consistent with those presented in the previous chapter, showing an elastic onset at De = 0.70 in the square array and at De = 0.25 in the hexagonal array. Sufficiently large Deborah numbers were not attained in either array to observe the asymptotic high Deborah number limit of flow resistance for this high molecular weight PIB.

The photos in Figures 3.10 (a) and 3.11 (a) were taken of flows at De = 0.16 and De = 0.06 respectively. As seen in Figure 3.12 these Deborah numbers are below the onset values. Accordingly, the particle paths in these photos are symmetric and match both those found with the Newtonian fluids and those calculated in the computer simulation. As the Deborah number increases past the onset values, the flow in both arrays go through a transition from a steady Newtonian flow to an unsteady flow. This has been observed in both arrays through the downstream pressure fluctuations discussed in the previous chapter and by LDV measurements discussed in the next section. The streak photographs presented here also capture this unsteadiness.

In the case of the square array, both flow unsteadiness and asymmetry are observed. The progression of the asymmetry with Deborah number can be observed in the photographs shown in Figures 3.10 (b)-(f). This asymmetry is characterized by particles which follow flow paths winding randomly between cylinders and crossing through lines of geometric symmetry. This becomes more apparent as the Deborah

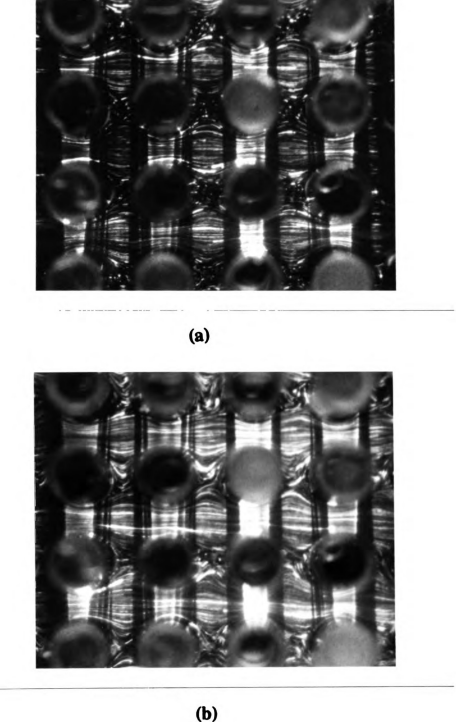
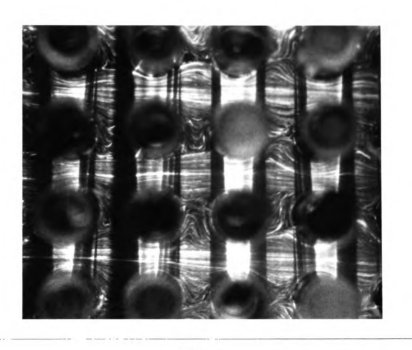
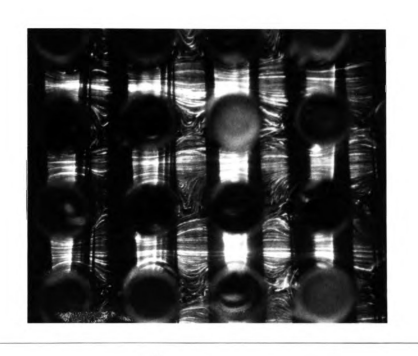


Figure 3.10 Streak photographs for the viscoelastic liquid in the square array having a void fraction of 70 percent (flow from right to left) (a) Re = 0.039, De = 0.16 (b) Re = 0.19, De = 0.80.

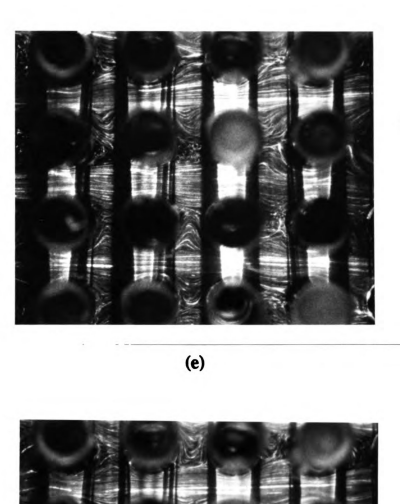


(c)



(d)

Figure 3.10 (c) Re = 0.25, De = 1.09 (d) Re = 0.36, De = 1.44.



(f)

Figure 3.10 (e) Re = 0.48, De = 1.91 (f) Re = 0.48, De = 1.91.

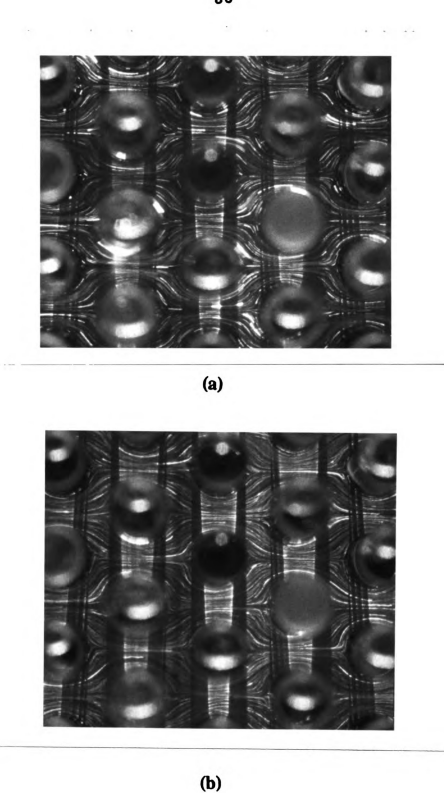
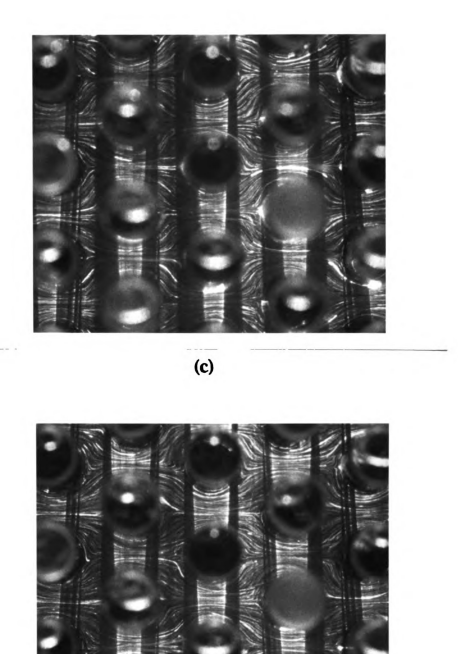


Figure 3.11 Streak photographs for the viscoelastic liquid in the hexagonal array having a void fraction of 70 percent (flow from right to left) (a) Re = 0.015, De = 0.059 (b) Re = 0.069, De = 0.28.



(d)

Figure 3.11 (c) Re = 0.11, De = 0.43 (d) Re = 0.14, De = 0.56.

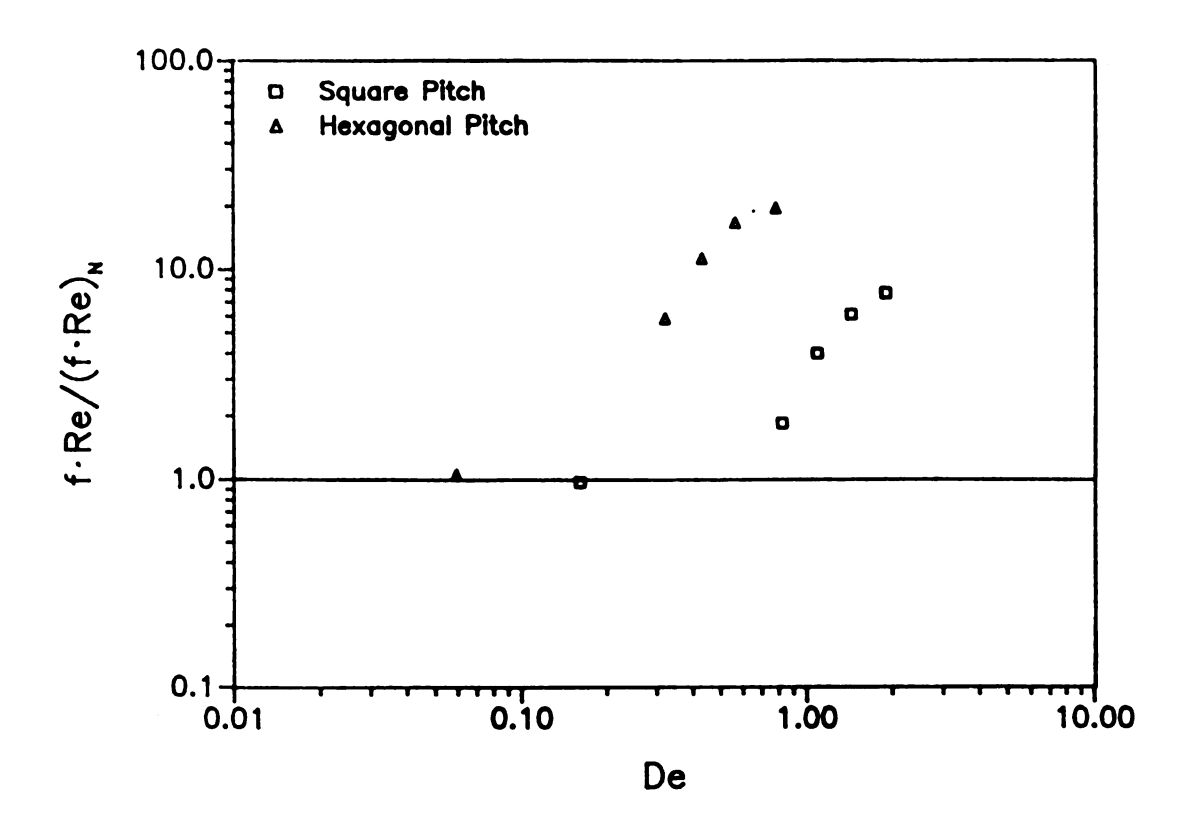


Figure 3.12 Relative flow resistance of a 0.25 % PIB/PB elastic liquid in both square and hexagonal cylinder arrays.

number is increased. The flow unsteadiness is apparent by comparing streak lines in photos taken at the same Deborah during two different experiments. From one snap shot to the next the particle paths differ - even at the same Deborah number! For example, Figures 3.10 (e) and (f) are photographs taken of two separate test runs, both at De = 1.91 and both at the same location in the flow field. Besides noting the asymmetry of the streak lines, one can also observe identical regions in the flow field where the particle paths are completely different from each other, indicating flow unsteadiness.

Particle path asymmetries and flow unsteadiness are not as easily observed in the photographs taken here of the high Deborah number flows with the hexagonal array (see Figure 3.11 (b)-(d). Close examination of the photos reveal many areas where the particle paths cross each other. This is most apparent in the highest Deborah number flow shown in Figure 3.11 (d). Particle path crossing is evidence of flow unsteadiness in the hexagonal array.

3.6.2 LDV measurements on the PIB/PB liquid

Laser Doppler velocimetry measurements of the PIB/PB liquids made along y = 1.62 and y = 1.74, in the square and hexagonal arrays respectively, confirm that for Deborah numbers below the onset values the kinematics of the flow are identical to those of Stokes flow (see Figure 3.13). This is no longer true when the Deborah numbers exceed the onset values.

The LDV measurements made in both arrays at Deborah numbers above the onset values resulted in Doppler signals which appeared extremely "noisy". The Doppler burst

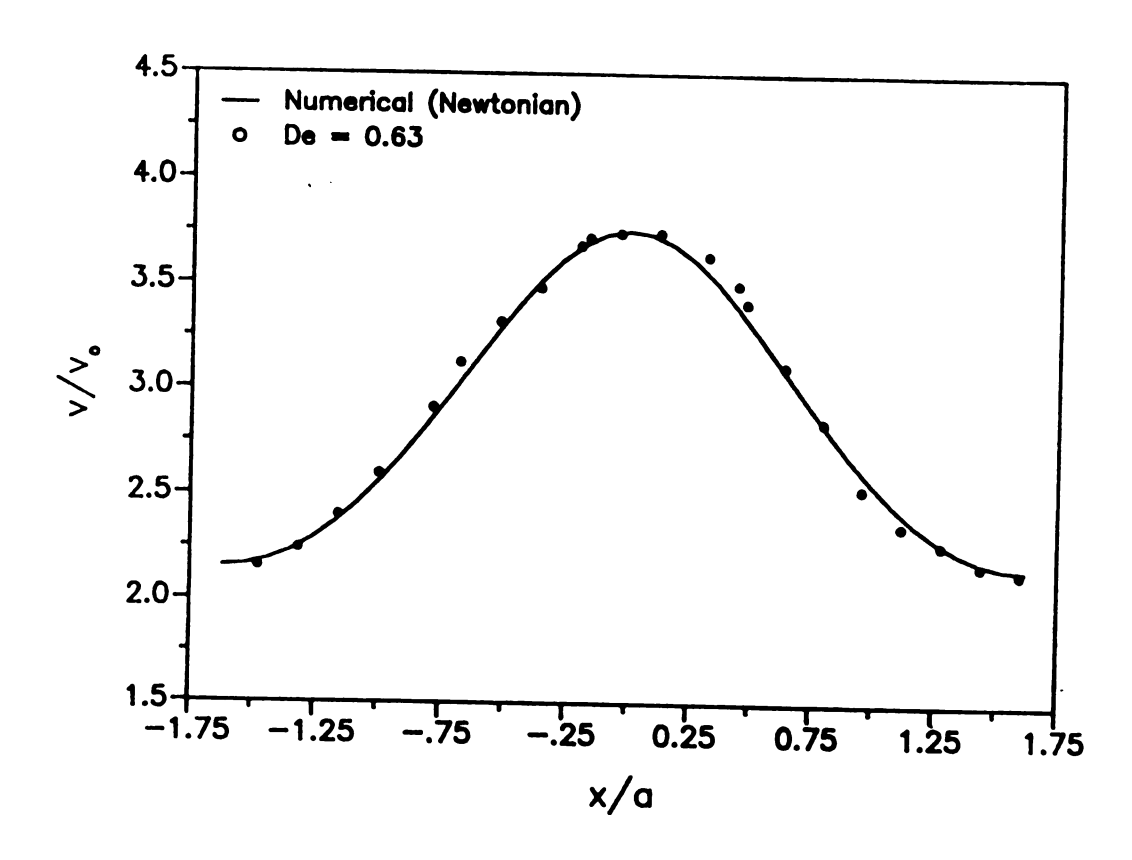


Figure 3.13 (a) LDV measurements and the Stokes flow prediction for the 0.25 % PIB/PB elastic liquid in the square array along y = 1.62.

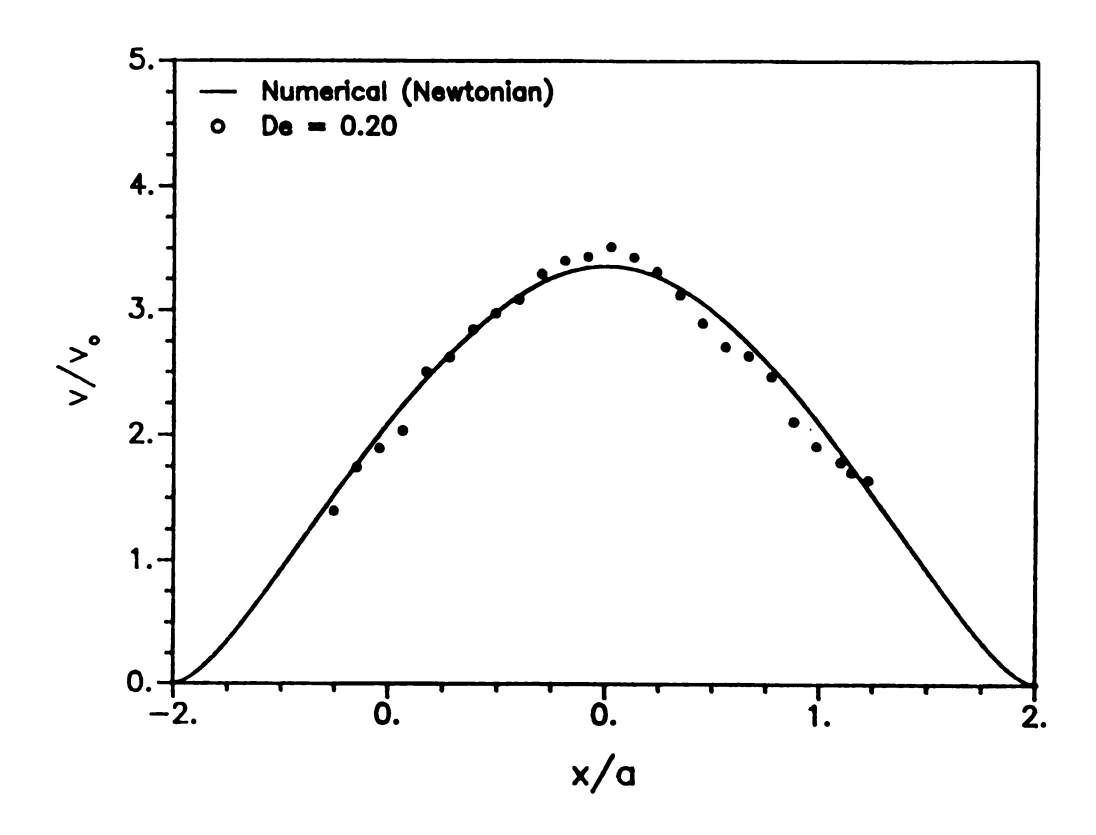
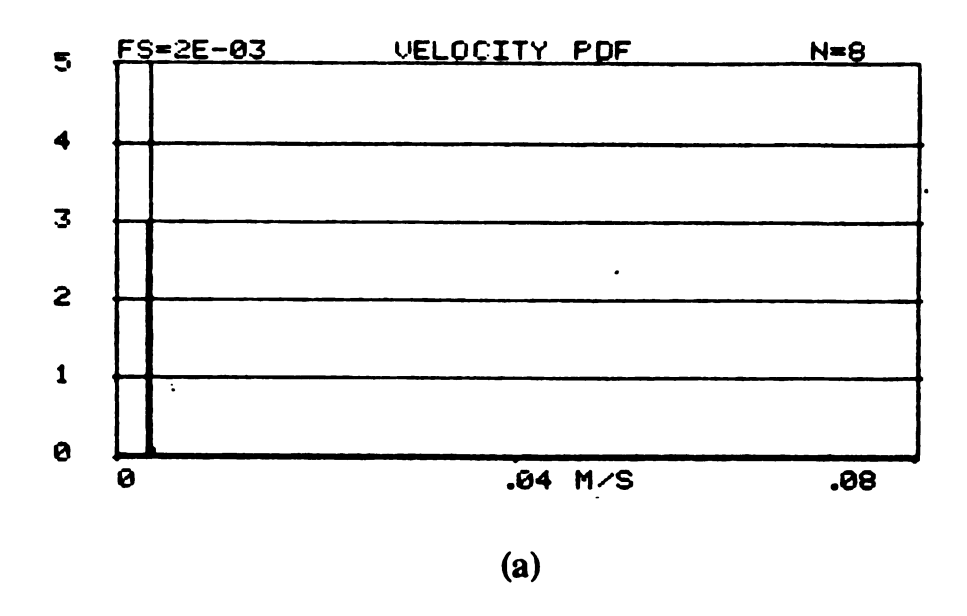


Figure 3.13 (b) LDV measurements and the Stokes flow prediction for the 0.25 % PIB/PB elastic liquid in the hexagonal array along y = 1.74.

was not composed of a single frequency as illustrated in Figure 3.3 but contained multiple frequencies. A local velocity unsteadiness will produce this result. Multiple scattering particles within the measuring volume, each moving at different velocities, will result in a Doppler signal containing several frequencies, as illustrated in Figure 3.14 (b). Figures 3.14 (a) and (b) show the probability distribution of 1024 velocity data points taken at x = -1.58 and y = 1.74 in the hexagonal array at two different Deborah numbers, De = 0.085 and De = 0.36 respectively. The extremely narrow velocity distribution shown in Figure 3.14 (a) indicates the steadiness of the flow below the onset Deborah number. Above the onset Deborah number, the velocity distribution is very broad (Figure 3.14 (b)), demonstrating the flow unsteadiness. Similar trends in the velocity probability distributions below and above the onset Deborah number were seen in the square array also. As a result of the handshake mode of data collecting it is impossible to determine whether the fluctuating velocity measurements in either array were time periodic.

3.6.3 LDV measurements on the PIB/decalin liquid

Figure 3.15 (a) shows velocity data in the square array along the symmetry line y = 1.62 for De = 0.69 and De = 0.82. At these Deborah numbers the flow is steady, and the shear thinning properties of the fluid dominate the flow dynamics, resulting in relative flow resistances below the Newtonian value (see Figure 2.15). The velocity profiles of Figure 3.15 (a) show higher velocities than the predicted Newtonian values along y = 1.62. This is consistent with the reduced pressure drop observed at these



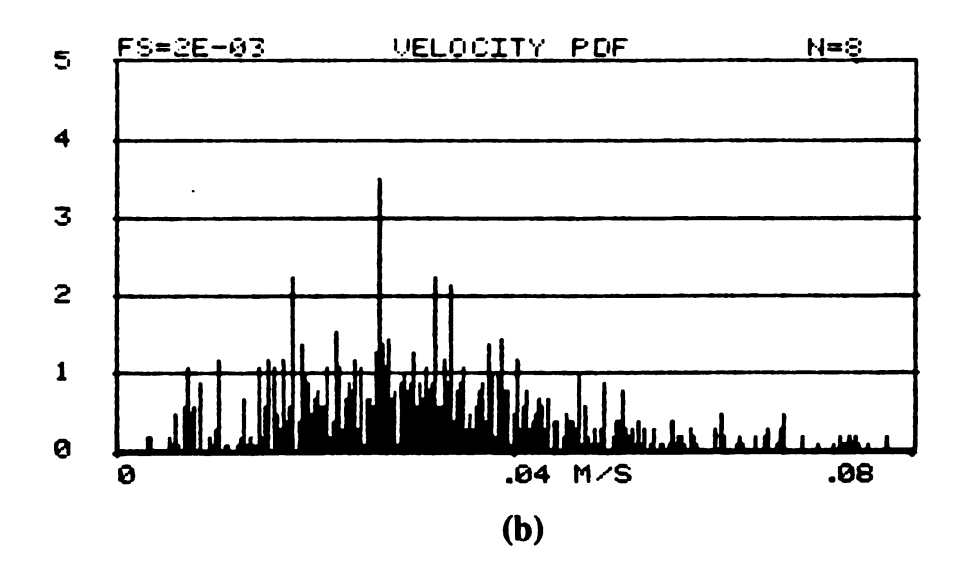


Figure 3.14 Probability distribution function of the elastic fluid's velocities measured in the hexagonal array at x = -1.58 and y = 1.74 (a) De = 0.085 (b) De = 0.36.

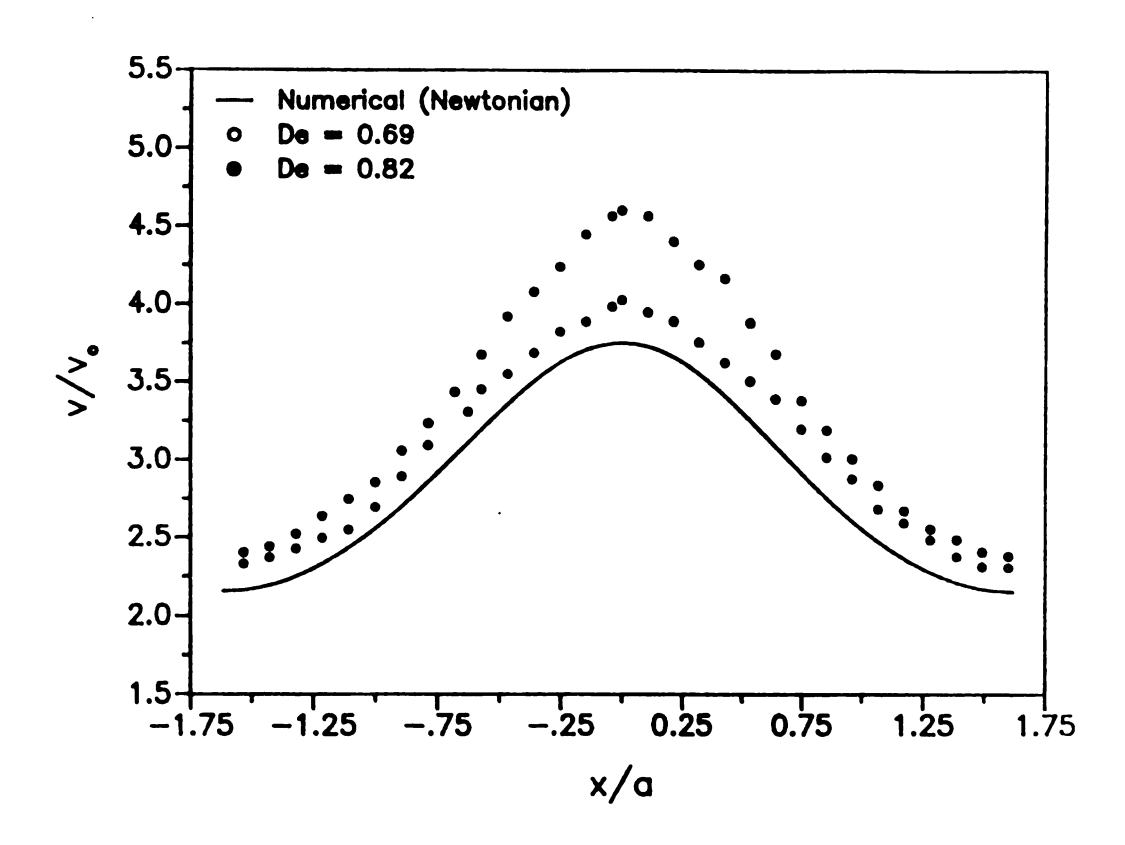


Figure 3.15 (a) LDV measurements and the Stokes flow prediction for the PIB/Decalin liquid in the square array along y = 1.62.

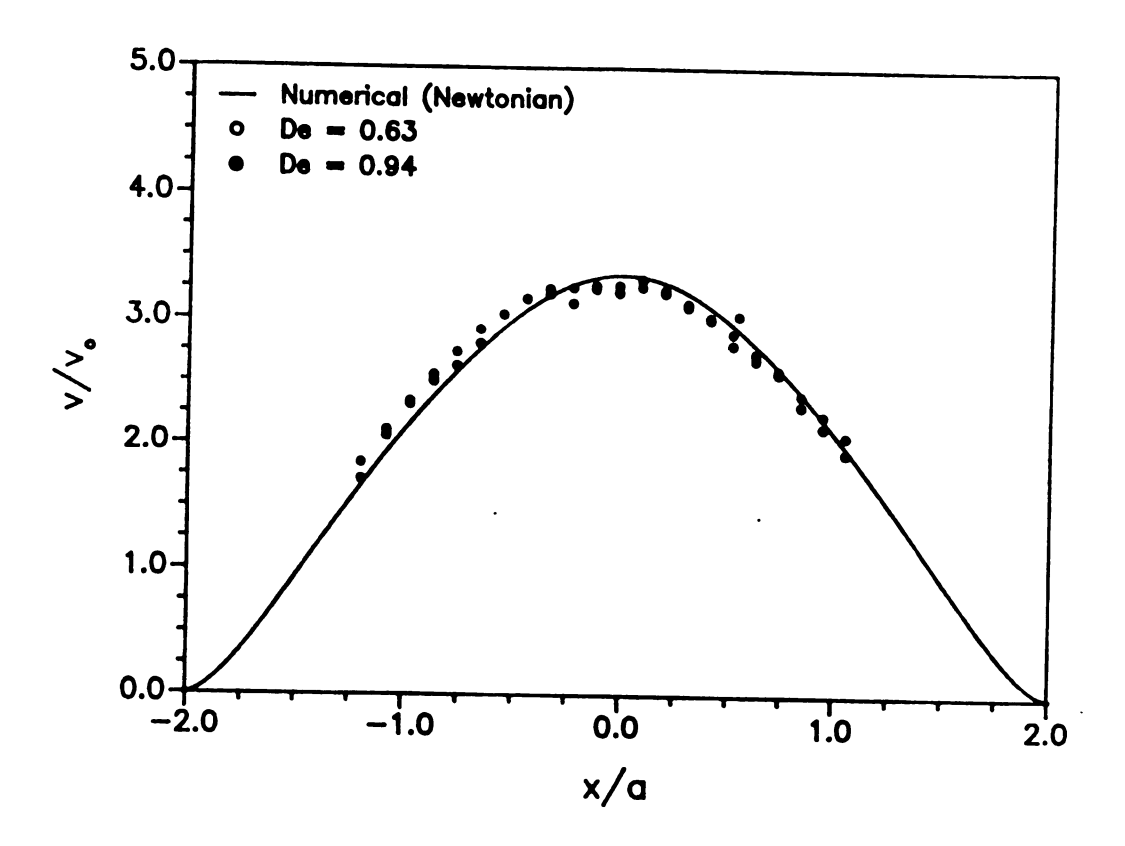


Figure 3.15 (b) LDV measurements and the Stokes flow prediction for the PIB/Decalin liquid in the hexagonal array along y = 1.74.

Deborah numbers. As the Deborah number is increased above 1.0 the extensional properties of the fluid begin to dominate and the relative flow resistance increases. As this occurs, a velocity transition similar to that found with the Boger liquid, is observed. For De > 1, the LDV signal becomes "noisy", indicating a transition from a steady to an unsteady flow.

Figure 3.15 (b) presents the velocity profiles along the line connecting two stagnation points (y = 1.74) in the hexagonal array for De = 0.63 and De = 0.94. Along this symmetry line the velocities agree with the Stokes flow prediction even though at these Deborah numbers the flow resistance curve of Figure 2.15 reveals a large shear thinning effect. As a result of the stagnation points on this particular symmetry line, the flow along this line is dominated by elongational properties. Shear thinning effects must occur in the narrow gaps that are not aligned in the x-direction. As the Deborah number increases above 1, extensional effects begin to dominate the flow and the relative flow resistance begins to increase. At this point the flow becomes unsteady.

The significance of these results is that at flow conditions where shear thinning effects dominate the flow is steady, even at Deborah numbers as high as 1. It is not until the extensional effects begin to dominate the flow at higher Deborah numbers that the flow becomes unsteady.

3.6.4 Discussion of flow unsteadiness

That the onset of flow unsteadiness occurs at the same Deborah number as the onset of the excess pressure drop suggests that the nature of the two phenomena are the

same. In the previous chapter it has been shown that increases in the relative flow resistance are consistent with and can be correlated by extensional viscosity increases occurring in localized regions within the cylinder arrays. This is evident in the hexagonal array. Stokes flow calculations show that along streamlines connecting stagnation points extension rates of up to 3.5 times the nominal shear rate are obtained. The large extension rates coupled with the high fluid residence time near the stagnation points cause macromolecules in these areas to elongate several fold and even break. This is supported not only by the chain extension calculations of Chmielewski *et al.* (1990), but also by the birefringence data of Cressely and Hocquart (1980). Cressely and Hocquart (1980) studied the flow of polymer solutions around a circular cylinder and found very localized birefringence along the streamline emanating from the stagnation point on the downstream side of the cylinder. In the case of the square array the region of the highest extension rates is localized along the symmetry line running between cylinder rows (y = 1.62).

At comparable Deborah numbers, the maximum extension rate in the square array is lower than that in the hexagonal array, resulting in differences in the onset Deborah number for the two arrays, 0.25 and 0.70 respectively. This difference in onset Deborah number can be accounted for quantitatively by redefining the Deborah number in terms of the maximum array extension rate instead of the nominal strain rate, $\dot{\gamma}_o$,

$$De^{\bullet} = \lambda_1 \cdot (\alpha \dot{\gamma}_o) \quad , \tag{3.3}$$

where α is 1.5 for the square array and 3.5 for the hexagonal array based on Stokes flow calculations. Thus, the onset of elastic effects occurs at De $^{\circ}$ ~ 1 for both arrays. This value corresponds to the Deborah number where macromolecules in extensional flows undergo the transition from a coiled to an elongated state - the coil to stretch transition (De ~ 1). Hence, at De $^{\circ}$ ~ 1 macromolecules in the polymer solutions become elongated in localized regions within the cylinder arrays, resulting in an excess pressure drop across the arrays.

The complex fluid dynamics resulting from high extensional stresses generated in the extensional flow regions may result in the observed flow unsteadiness. An indication of the apparent Trouton ratio attained in the cylinder arrays can be obtained from the fiber spinning experiments of the previous chapter. The ratio of the average extensional viscosity to the shear viscosity of a 2.11 million molecular weight PIB in PB solution is 1500 at De = 3.6. Also, data on a PIB in decalin solution show that this ratio increases with increasing Deborah number.

The onset of flow unsteadiness, occurring at the same Deborah number where localized regions of large stress appear is consistent with the observations reported by Ambari et al. (1984) on laminar flow around a single cylinder. They used an electrochemical technique to study the mass transfer from a circular cylinder in dilute polyethylene oxide solutions. At an onset Deborah number of approximately 3 they observed a large decrease in the mass transfer rate with respect to the Newtonian value. This decrease was accompanied by an onset of fluctuations of the limiting diffusion current. The RMS values of these fluctuations increased with increasing Deborah

numbers, but eventually reached a plateau. Ambari et al. (1984) attributed these fluctuations to the high extensional viscosities localized near the upstream cylinder stagnation point.

Similar to the observations of Ambari et al. (1984), LDV measurements taken at a single point in the flow field demonstrate an increase in the "degree" of flow unsteadiness with increasing Deborah number. The degree of unsteadiness is quantified by the ratio of the standard deviation of a set of velocities measured at a point to the mean value. As the Deborah number of the flow is increased the standard deviation ratio increases. This is shown in Figure 3.16 which represents LDV data taken in the hexagonal array at a point approximately one half cylinder radius behind a stagnation point (x = -1.58 and y = 1.74). Figure 3.16 shows that at De ~ 0.2 (De* ~ 1) there is a large jump in the degree of unsteadiness, confirming that this Deborah number indeed represents a transition point for viscoelastic flow in the hexagonal array. Unlike the observations of Ambari et al. (1984), the standard deviation of the fluctuations does not level off for the Deborah number range shown in Figure 3.16.

3.7 Conclusions

The kinematics of viscous and viscoelastic liquids flowing through square and hexagonal cylinder arrays has been studied. Both streak photographs and LDV measurements indicate that below an onset Deborah number, De* ~ 1, the flow of non-shear thinning elastic fluids is identical to the Stokes flow field. However, above the

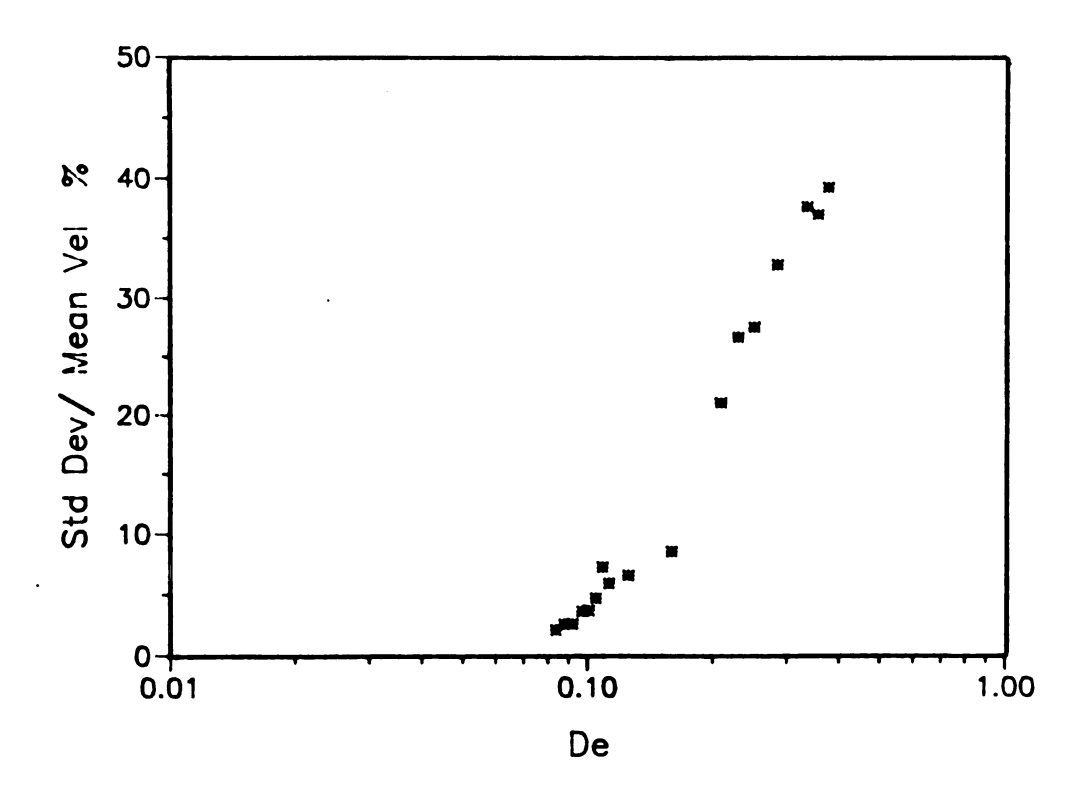


Figure 3.16 Growth of the flow instability in the hexagonal array for the 0.25 % PIB/PB elastic liquid as measured by LDV at x = -1.58 and y = 1.74.

onset Deborah number the flow becomes unstable. The results with the shear thinning liquids underline the elastic origin of the instability observed.

The steady Newtonian flow changes to an unsteady and spatially aperiodic flow field at an onset Deborah number where elongational flow dominates. This onset Deborah number corresponds to the onset of fluid elasticity effects on the pressure drop across the array. Thus, any attempt to predict flow resistance increases must describe the viscoelastic transition to unsteady flow.

Chapter 4

THE DEGRADATION OF POLYMER SOLUTIONS FLOWING THROUGH ARRAYS OF CIRCULAR CYLINDERS

This chapter was published in the *Journal of Non-Newtonian Fluid Mechanics* 35, 309-325 (1990), with co-authors C.A. Petty and K. Jayaraman.

4.1 Summary

The flow of a dilute solution of polyisobutylene in polybutene transverse to unidirectional arrays of cylinders has been investigated at Reynolds numbers less than 0.1. Two different arrays were used - a triangular pitch array and a rectangular pitch array. Both arrays have a porosity of 0.704, the same bed length and comprise identical cylinders. Steady state permeation experiments were run over a range of superficial velocities in both arrays, to study the onset of departure from Darcy's law. The rheology of the fluid was evaluated in shear before and after each set of runs.

While departures from Darcy's law occurred in both arrays at similar values of

Deborah number, mechanical degradation of the polymer solution was much more severe with the triangular pitch array than with the rectangular pitch array. Specifically, after several runs through the triangular array the relaxation time was halved while the change in viscosity was relatively minor; this reveals loss of the high molecular weight tail in the original polymer. This degradation was irrecoverable; no recovery was noted after two weeks. Measurements of molecular weight distribution on the same samples in Odell's laboratory confirm that the highest molecular weight components are degraded.

Finite element simulations of Stokes flow were carried out for the two different geometries to determine extensional strain rates along the flow direction in several regions. This was followed by calculations of polymer chain deformation in these regions, with the nonlinear elastic dumbbell model. These calculations reveal that the maximum stretch rate in the triangular pitch array occurs along the streamline joining the stagnation points on adjacent cylinders; this leads to nearly complete extension of the polymer chain at a nominal Deborah number of 1 in the triangular array. However, in the rectangular pitch array, the maximum stretch rate occurs along streamlines considerably removed from the stagnation points, and the polymer chains are not extended along those streamlines up to a Deborah number of 1.

4.2 Introduction

The flow of liquids through regular arrays of cylinders arises in a variety of applications ranging from heat exchangers with tube bundles, to manufacture of fiber

reinforced composites. Darcy's law is often employed as a macroscale model for flow of incompressible, Newtonian fluids through porous media at low Reynolds numbers. This macroscale representation of the superficial velocity v in anisotropic media can be written as

$$\eta \mathbf{v} = -\mathbf{K} \cdot \langle \nabla P \rangle, \tag{4.1}$$

where η is the viscosity of the fluid, K is the permeability tensor defined entirely by the geometry of the array and $\langle \nabla P \rangle$ is the mean pressure gradient in the fluid. The longitudinal permeability K₃₃ describes flow along the direction of the aligned axes of the cylinders, x₃. Flow in the plane transverse to the cylinder axis may be described in general by three constants - K₁₁, K₁₂, K₂₂, for any given configuration - cf. Sangani and Yao (1988). These constants represent the transverse permeability which is generally much lower than the longitudinal permeability. In arrays with additional rotational symmetry such as square or hexagonal packing of cylinders, one parameter suffices to describe the transverse permeability. Theoretical values of this quantity have been tabulated for both square and hexagonal arrays by Sangani and Acrivos (1982). These values were obtained by numerical solution of the creeping flow equations over representative cells for these arrays. They have also provided analytical expressions for this quantity in dilute arrays and in concentrated arrays. For arrays with void fraction greater than 0.5, the predicted values of transverse permeability with square packing and hexagonal packing are not significantly different.

No quantitative results are available from experiments or from theory for the

permeation of viscoelastic liquids transverse to regular arrays of cylinders. The flow of viscoelastic liquids at low Reynolds numbers through packed beds of spheres has been studied experimentally by Marshall and Metzner (1967). The fluids they used has a shear rate dependent viscosity as that these fluids obey Eq. 4.1 only up to a certain critical value of nominal strain rate in the bed. As the strain rate was increased above this threshold, the pressure gradient or frictional resistance increased progressively from the Darcy value by factors of 10 or more. This increase was correlated with a Deborah number, which is the product of a fluid relaxation time and strain rate. Other workers (James and McLaren, 1975, Kulicke and Haas, 1984 and Durst et al., 1981) have studied the resistance to flow of very dilute ("drag reducing") solutions of polymers passing through packed beds of spheres. These workers have reported an onset Reynolds number at which the flow resistance increased suddenly from Newtonian behavior by an order of magnitude. For example, James and McLaren (1975) worked with dilute aqueous solutions of polyethylene oxide passing through packed beds at low Reynolds numbers. They observed that the onset Reynolds number decreased with increasing concentration and with increasing molecular weight of polymer. They reported also that degradation occurred especially with larger bead sizes (0.045 cm diameter). Kulicke and Haas (1984) have shown that, for a given solvent polymer pair, the onset Reynolds numbers may be used to infer the weight average molecular weight of the polymer. Both effects-the increase in flow resistance, and degradation-have been attributed to the strong extensional flow component in such flows (see Durst et al., 1981).

The object of this paper is to report specific features of this extensional flow

component that appear to be critical in crossflow of viscoelastic liquids through unidirectional cylinder arrays with different packing geometries at a given level of porosity. The work involves both calculations of chain extension in specific geometries and steady state permeation experiments through such arrays. The liquids used have constant shear viscosity and significant elasticity. The results show that the packing geometry has a significant effect on the extent of degradation of the polymer in the porous medium. This result is explained with model calculations of polymer chain extension in the two arrays.

4.3 Experimental

4.3.1 Materials

Three test fluids were used in this investigation-the elastic M1 liquid, another dilute solution of polyisobutylene in polybutene and a Newtonian analog to the M1 fluid. It was necessary to prepare another dilute polyisobutylene solution similar to the M1 fluid because only a limited supply of the M1 liquid was available. This elastic analog was prepared by first dissolving the polyisobutylene (Vistanex L-120 from Exxon Chemical Company, $M_w = 1.66 \times 10^6$) in kerosene. This solution was then mixed with an appropriate amount of polybutene (Indopol H300 from Amoco Chemical Company) in order to obtain a shear viscosity similar to that of the M1 fluid (see Figure 4.1). The Newtonian analog was prepared by mixing 17% by weight kerosene into polybutene, again in order to obtain a shear viscosity similar to that of the M1 fluid (see Figure 4.1).

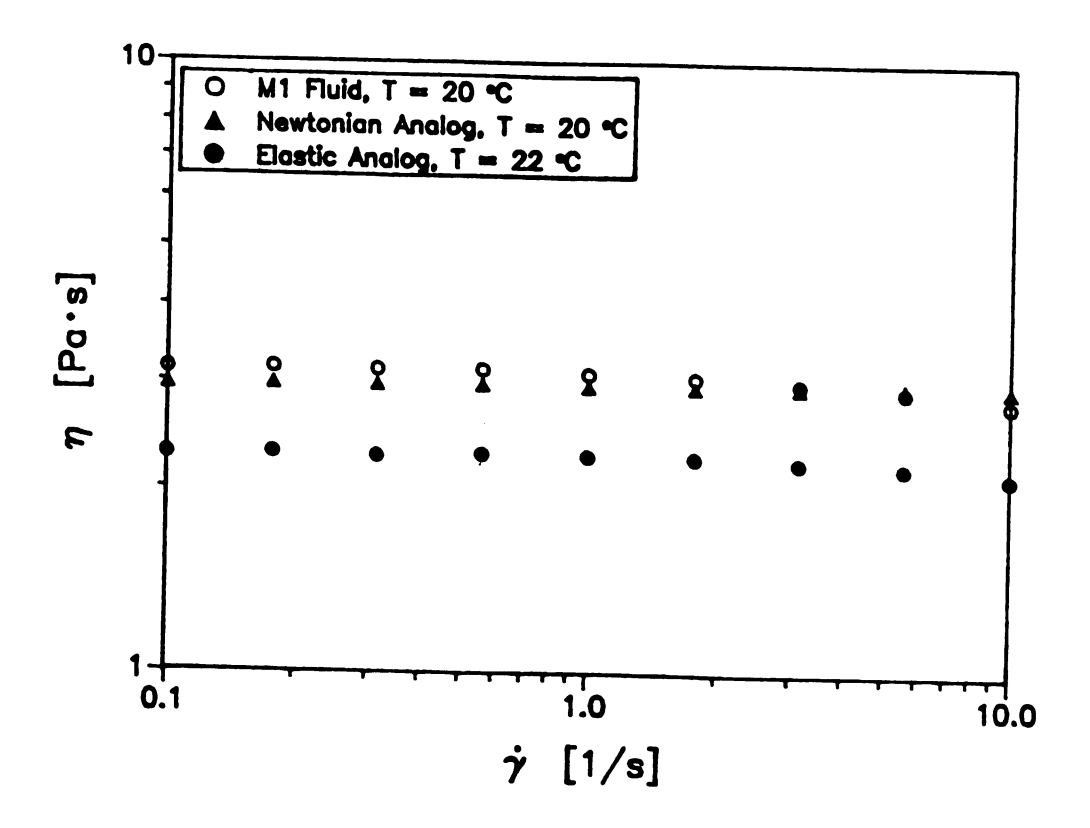


Figure 4.1 Steady shear viscosity of the fresh test fluids.

4.3.2 Rheological properties

All viscometric measurements were obtained with a Rheometrics RFS-8400 fluids spectrometer. Viscosity measurements were made under steady shear at rates ranging from 0.1 to 10 s⁻¹ and at six temperatures ranging between 15 and 30 °C. The dynamic moduli of the elastic fluids were measured under oscillatory shear at frequencies ranging from 0.1 to 100 rad/s. Measurements on the M1 liquid were made at six temperatures, also ranging between 15 and 30 °C. The elastic analog was tested only at 22 °C. Figure 4.1 is a plot of the steady shear viscosity, η , of the test fluids. The test fluids do not exhibit any shear thinning for strain rates less than 1 s⁻¹. Only slight shear thinning can be observed for the M1 fluid and the elastic analog for rates greater than 1 s⁻¹. This figure also shows that these fluids have similar viscosities near room temperature. This can be seen more clearly in Table 4.1 where the properties of the flesh test fluids are compared at the same temperature. Figure 4.2 shows the results of the oscillatory and steady shear experiments, using the M1 liquid, at 20 °C. These data extend to low enough frequencies and shear rates where the dynamic viscosity matches the steady shear viscosity. A relaxation time λ_1 may be calculated from the low frequency region of the storage modulus, G', where G' is quadratic in ω , as follows:

$$\lambda_1 = \frac{G'}{\omega^2 \left(\eta_G - \eta_g \right)}. \tag{4.2}$$

Table 4.1 Properties of the fresh test fluids.

Fluid	Temp.	⁹ o Pa∙s	/ kg/m ³	λ ₁ sec.
Ml Fluid	22.0	2.73	866.	0.220
Newtonian Analog 83% Polybutene 17% Kerosene	22.0	2.58	873.	
Other PIB Solution 81% Polybutene 18.7% Kerosene 0.25% PIB L-120	22.0	2.28	871.	0.102

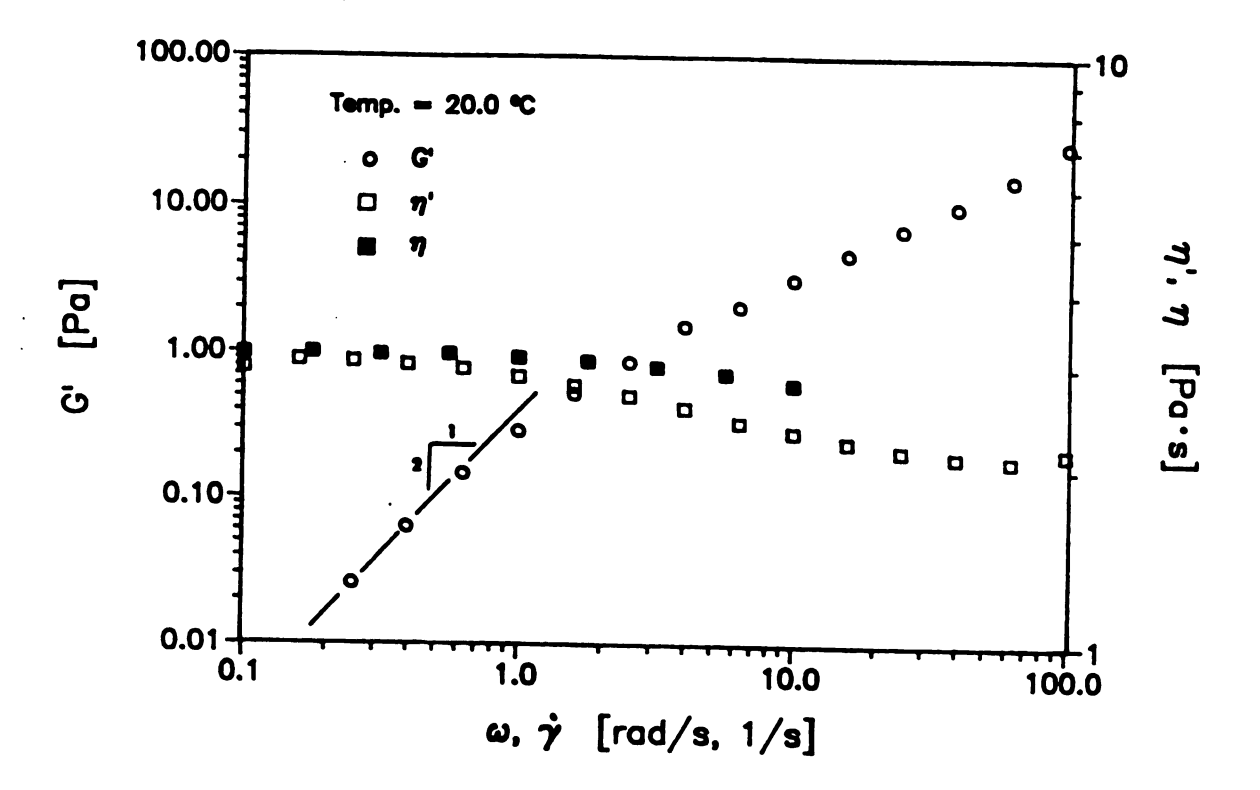
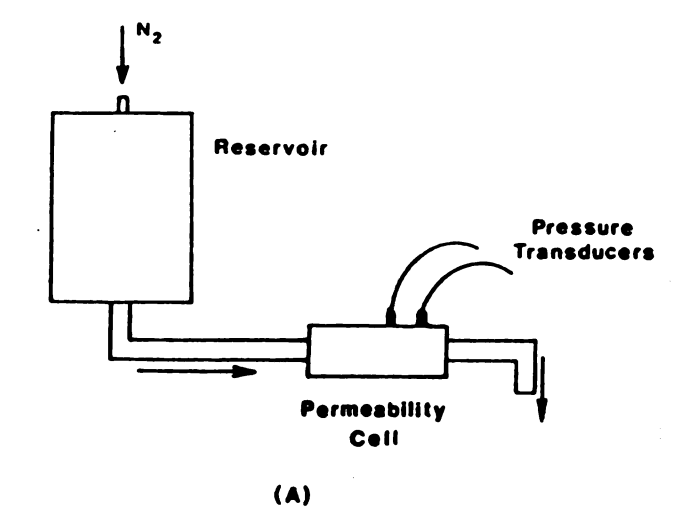


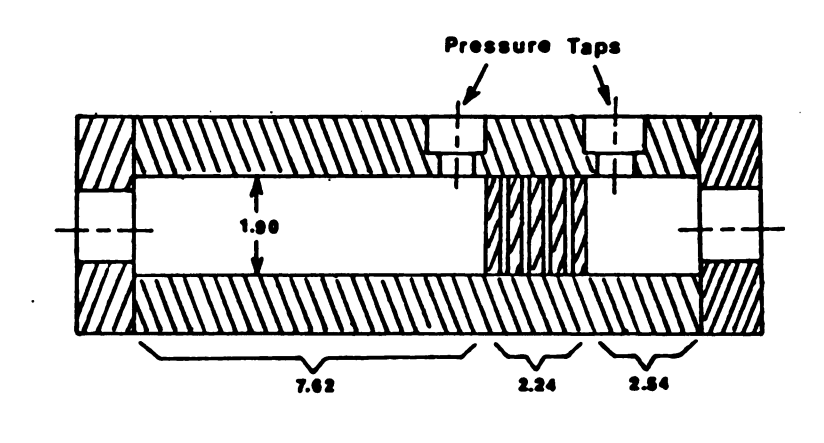
Figure 4.2 Dynamic moduli and steady shear viscosity of the fresh M1 fluid.

Here η_o is the zero shear viscosity of the solution and η_s is the solvent viscosity. This relations provides a good estimate for the FENE dumbbell model in the form used by Chilcott and Rallison (1988) if the ratio of fully extended dumbbell length to equilibrium length is 10 or more for the polyisobutylene is polybutene (cf. Chmielewski et al., 1990). A comparison of the properties for the M1 fluid and the elastic analog is also given in Table 4.1.

4.3.3 Apparatus

A diagram of the experimental apparatus is shown in Figure 4.3. The apparatus consists of a reservoir connected at one end to a nitrogen cylinder and at the other end to the permeability cell. During an experimental run, the reservoir is charged with the test fluid. A constant pressure is then supplied to the reservoir via a nitrogen tank and pressure regulator. The flowrate was varied by varying the upstream reservoir pressure. As the fluid exits the reservoir, it passes through a 5.3-to-1 contraction; the fluid then flows through a 20 cm long pipe to enter the permeability cell with a 2-to-1 expansion. The permeability cell (with cross-sectional view shown in Figure 4.3) consists of three sections. The cross-section of the cell is rectangular, measuring 5.33 cm by 1.9 cm. The entrance section leading to the array is 7.62 cm long. The length of the cylinder bed is 2.24 cm. This consists of five rows of cylinders with a maximum of ten cylinders per row; the cylinders are aligned along the 1.9 cm gap. The exit section is 2.54 cm long. The test fluids exit the permeability cell by going through a 2-to-1 contraction and into a short exit pipe.





(B)

Cell Width = 5.24

Figure 4.3 (A) Schematic of experimental apparatus and (B) a cross-sectional view of the permeability cell (all dimensions are in centimeters).

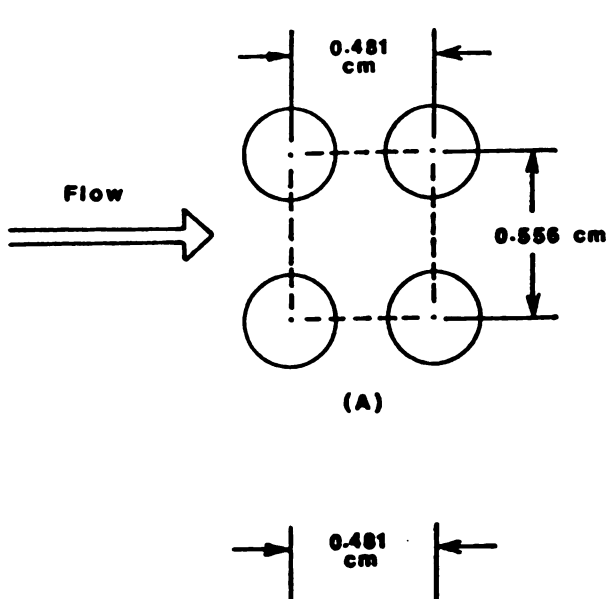
Two different cylinder arrays were used in this study as shown in Figure 4.4. In one array, the rows are aligned one behind the other to produce a rectangular pitch; in the other array, successive rows are staggered to produce an equilateral triangle pitch. The cylinder radius a is 0.159 cm and the porosity is 0.704 in both arrays. The gap between two cylinder surfaces in a row (i.e. perpendicular to the flow direction) is 0.238 cm for either array. The spacing between cylinder axes in successive rows of the staggered array forms an equilateral triangle. This array is equivalent to the hexagonal packing referred to by Sangani and Acrivos (1982). However, in the rectangular array, the gap between cylinder surfaces in successive rows is 0.163 cm. The cylinder ends are threaded to fit into the top and bottom plates in corresponding patterns. In the rows containing ten cylinders, the cylinder on either end is tangent to the channel wall.

The pressure drop across the bed of cylinders was measured by two Omega PX-610 miniature pressure transducers connected to a strip chart recorder. The bed length l was the same (2.24 cm) in all experiments. The flow rates were measured gravimetrically. All experiments were conducted at Reynolds numbers (see Eq. 4.4) ranging from 0.005 to 0.1. The temperature of the fluid was monitored by a small thermocouple contacting the fluid at the exit of the permeability cell.

4.3.4 Wall and end effects

Larson and Higdon (1987) have analyzed the flow near the surface in transverse flow of a Newtonian fluid at low Reynolds numbers through periodic arrays of cylinders.

They concluded that the effect of external velocity is damped out well before the second



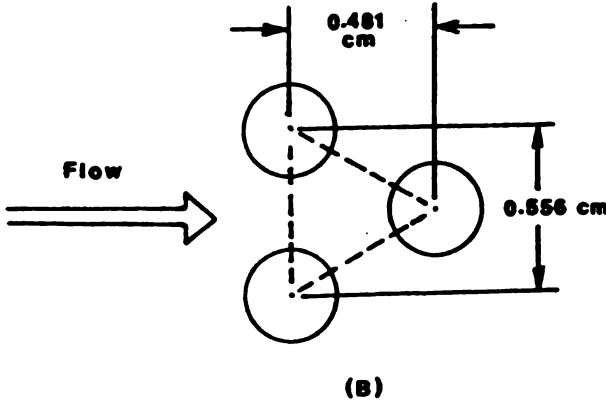


Figure 4.4 Cylinder array geometries: (A) rectangular pitch array; (B) triangular pitch array (radius = 0.159 cm and porosity = 0.704).

row of the array for a solids concentration of 0.3. A crude estimate of the distance into the array for effective damping (cf. Larson and Higdon, 1986) is given by \sqrt{k} , where k is a relevant permeability. Using the transverse permeability values reported in the next section, we may then estimate that end effects are damped within 0.05 cm. The effect of the side walls is expected to be small because there are ten cylinders in every row. Finally, good agreement between the experimentally determined permeability for the triangle array and the theoretically value obtained by Sangani and Acrivos (1982) confirms that the wall and end effects in these experiments are acceptably small.

4.4 Results and discussion

4.4.1 Transverse permeability of Newtonian liquid

The magnitude of the mean pressure gradient is plotted against superficial velocity in Figure 4.5 for the Newtonian fluid flowing transverse to the two arrays. The flow in either bed is seen to follow Darcy's law. Both lines drawn through the data on this log-log plot are of slope 1 and the transverse permeability may be determined from the intercepts of these lines. The value of $2.71 \times 10^7 \text{ m}^2$ for the array with triangular pitch compares very well with the theoretically predicted value of $2.86 \times 10^{-7} \text{ m}^{-2}$. The theoretical value of transverse permeability for the triangular array may be obtained from the results of Sangani and Acrivos (1982) [in Table 2 of their paper]. The transverse permeability for the rectangular array with the same porosity is found to be $4 \times 10^{-7} \text{ m}^2$. This is higher than the theoretical value of $2.67 \times 10^{-7} \text{ m}^2$ for a square array with the

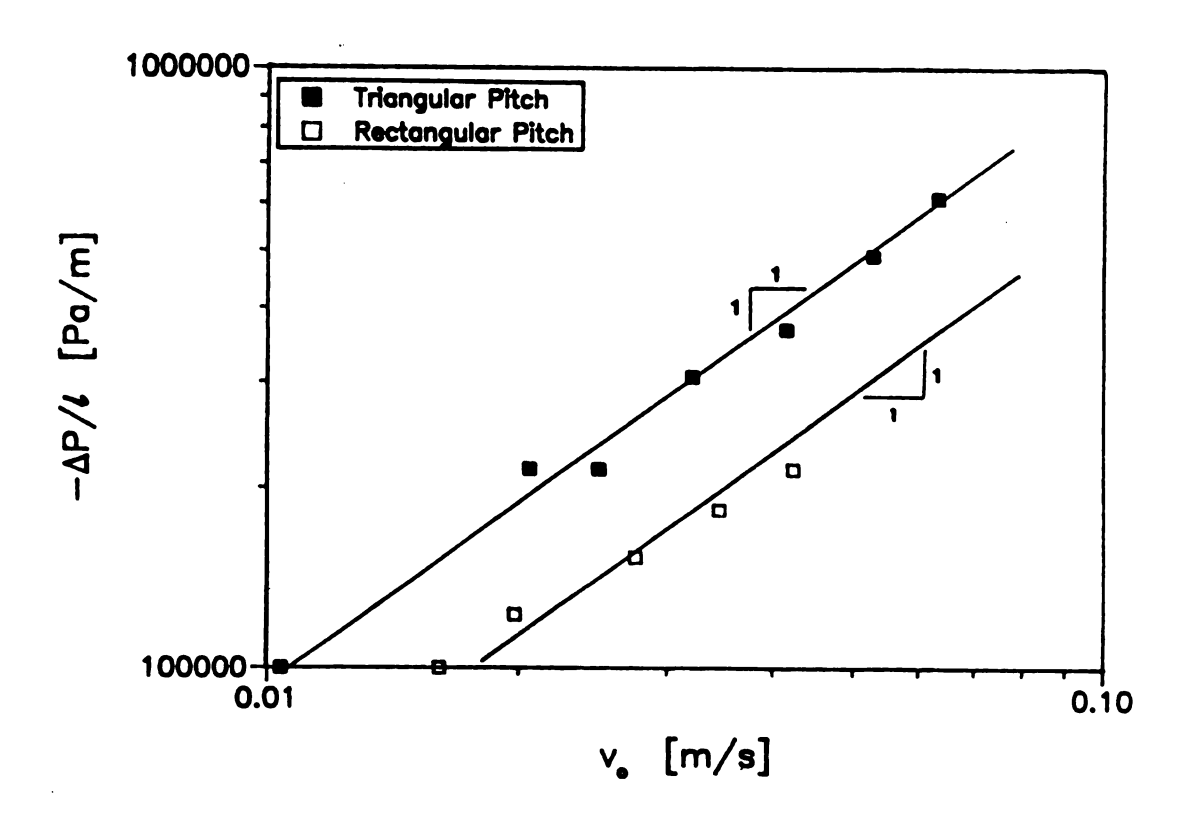


Figure 4.5 Mean pressure gradient vs. superficial velocity for the Newtonian fluid.

same area void fraction presumably because the gap between cylinder surfaces in one direction (0.238 cm) is considerably higher than the gap in another direction (0.163 cm); either gap would be 0.2 cm for the square array of the same porosity.

4.4.2 Departure from Darcy's law for elastic liquids

The onset of viscoelastic effects may be conveniently represented on a plot of the porous bed friction factor against a Reynolds number. The porous bed friction factor is defined conventionally by

$$f = \frac{(-\Delta P) \rho \cdot 2a\epsilon^3}{IG_o^2 (1-\epsilon)}, \qquad (4.3)$$

where ρ is the fluid density, $-\Delta P$ is the pressure drop, ϵ is the void fraction of the bed and G_o is the superficial mass flux. The Reynolds number is defined by

$$Re = \frac{2aG_o}{\eta_o(1-\epsilon)}.$$
 (4.4)

For Newtonian liquids, the friction factor is inversely proportional to the Reynolds number. The data for Newtonian liquids flowing through the rectangular array can be correlated by the product $f \cdot Re = 100$ while the data for the triangular array can be correlated by $f \cdot Re = 150$.

The friction factor is plotted against Reynolds number for the M1 fluid through the triangular and rectangular pitch arrays in Figures 4.6 and 4.7, respectively. Since only a limited supply of the M1 fluid was available, each of the experimental runs was made with the same charge of M1 fluid. The first set of experiments using the fresh M1 fluid was made with the triangular pitch array and is denoted as Set 1 in Figure 4.6. During this set of experiments the superficial velocity varied from 0.17 cm/s to 1.34 cm/s. The onset Reynolds number is 0.01 for the first set of runs with fresh M1 liquid. A second set of runs was made with the same fluid in the triangular pitch array is order to check for polymer degradation. Figure 4.6 shows that the onset Reynolds number for this set has increased to 0.02, indicating degradation of the polymer solute. This observation is consistent with the increase in the onset Reynolds number observed by James and McLaren (1975) and by Kulicke and Haas (1984) upon lowering the polymer molecular weight in a polymer solution. Only a few of the data points after the onset are shown on Figure 4.6 for either set because degradation changes the properties of the fluid progressively during the course of several runs. Data for the rectangular pitch array in Figure 4.7 were also obtained from runs with degraded M1 liquid and the onset Reynolds number was around 0.026.

Measurements of relaxation times reported in the next section for the M1 liquid at various stages of degradation show that the superficial velocity at the onset of viscoelastic effects scales inversely with relaxation time. This may be restated in terms of the Deborah number - a dimensionless product of the nominal strain rate (v_o/a) and the relaxation time λ_1 :

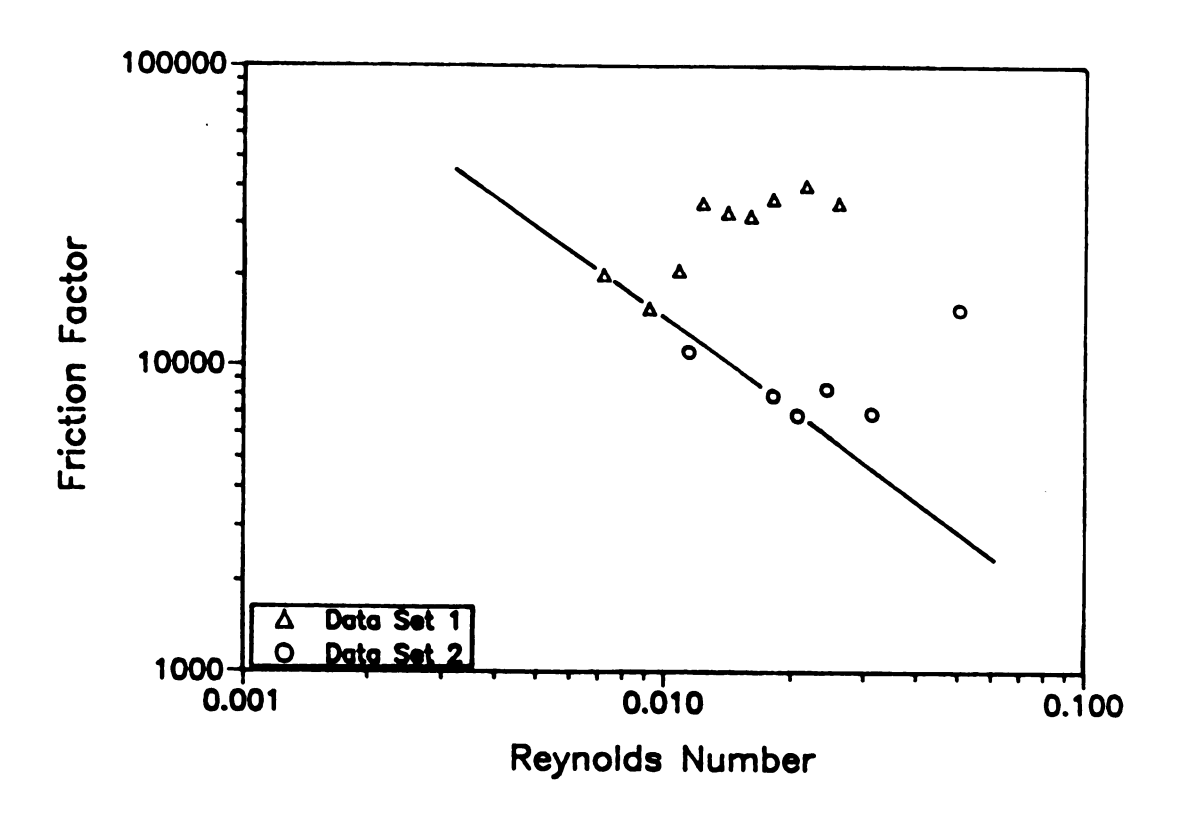


Figure 4.6 Friction factor vs. Reynolds number for the M1 fluid flowing through the triangular pitch array.

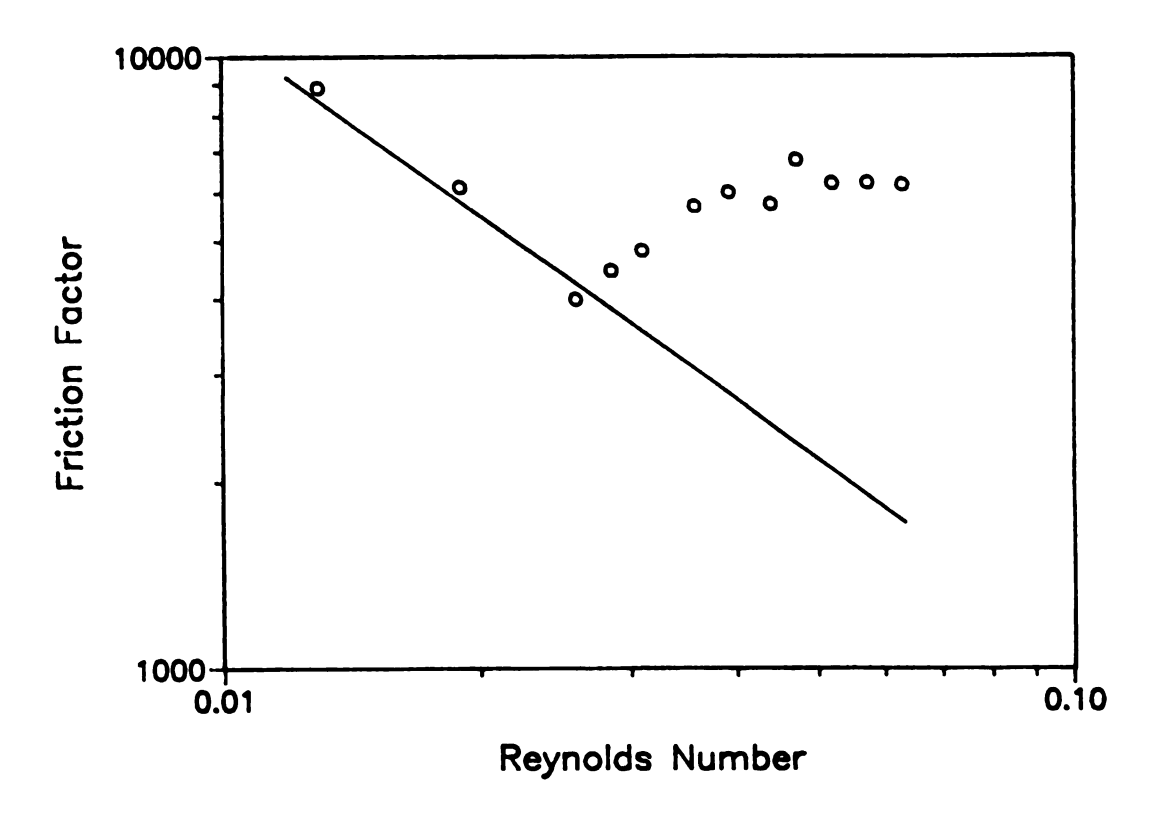


Figure 4.7 Friction factor vs. Reynolds number for the M1 fluid flowing through the rectangular pitch array.

$$De = \frac{v_o \lambda_1}{a}. \tag{4.5}$$

The Deborah number at onset of viscoelastic effects is about 0.3 for the triangular array and 0.4 for the rectangular array. This may be seen on a plot of the ratio $f \cdot \text{Re}/(f \cdot \text{Re})_N$ against the Deborah number in **Figure 4.8**. The magnitude of the resistance ratio is consistently lower for the runs through the rectangular array than for the triangular array. This difference may be due in part to the degradation of the M1 before it is passed through the rectangular array. Fresh batches of another PIB solution have been used to explore the extent of degradation alone.

4.4.3 Degradation of elastic liquids

The steady shear viscosity and dynamic shear storage modulus were evaluated for samples of the M1 fluid taken at three different stages to assess the extent of degradation. These measurements at 23 °C are reported in Table 4.2. The first sample was taken of the fresh liquid. The second sample was taken after the fluid was passed 20 times consecutively through the triangular array at nominal strain rates ranging from 0.5 to 8.4 s⁻¹. The relaxation time changed from 0.19 s for the fresh fluid to 0.098 s for the second sample; the shear viscosity change was relatively minor-less than 10%. This trend is fluid property change is typically associated with changes in molecular weight distribution. The third sample was taken after the degraded fluid was passed 13 times

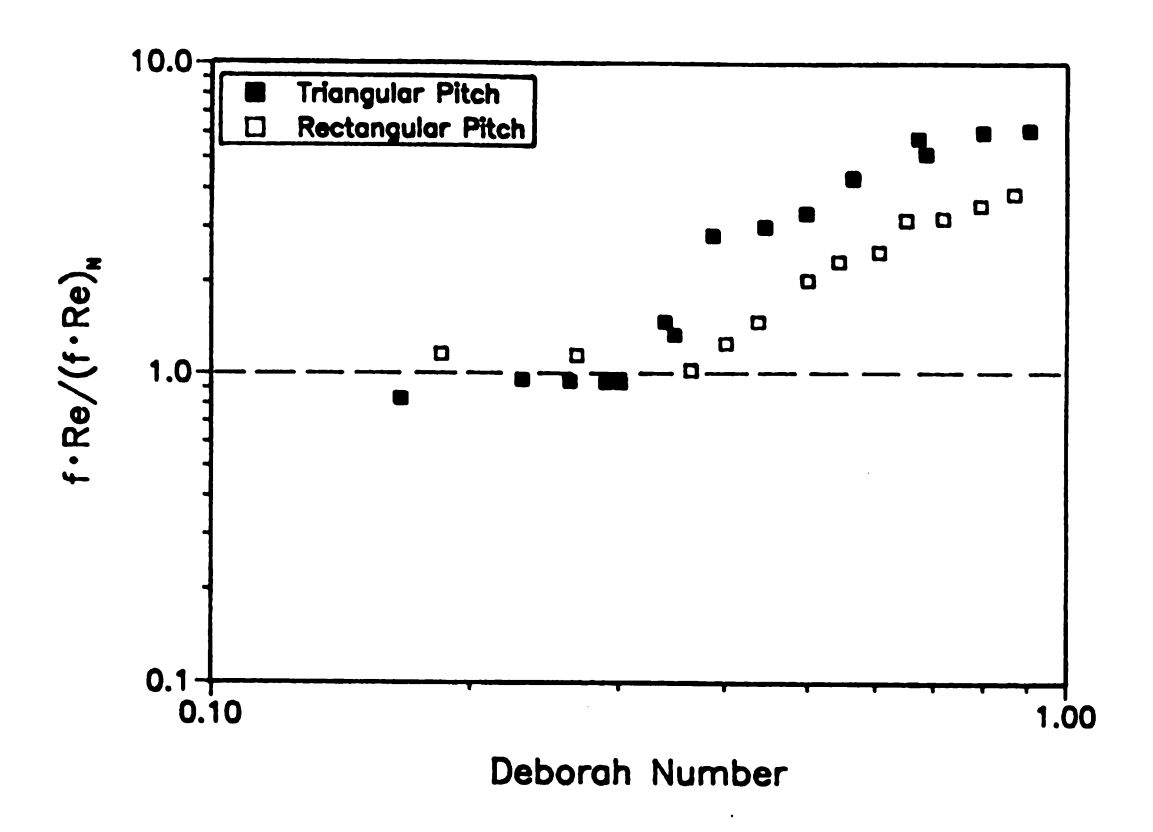


Figure 4.8 Flow resistance of the M1 fluid relative to the Newtonian value vs. Deborah number.

Table 4.2 Properties of elastic liquids before and after crossflow runs in different arrays.

State	70	λ ₁
	Pa·s	sec.
M1 Fluid at 23°C		
Fresh	2.53	0.190
After 20 passes through triangular pitch array	2.30	0.098
After runs through both array types	2.26	0.080
Two weeks following runs in both array types	2.26	0.080
Other PIB solution at 22°C		
Fresh	2.28	0.102
After 14 passes through triangular pitch array only	2.17	0.065
After 14 passes through rectangular pitch array only	2.28	0.094

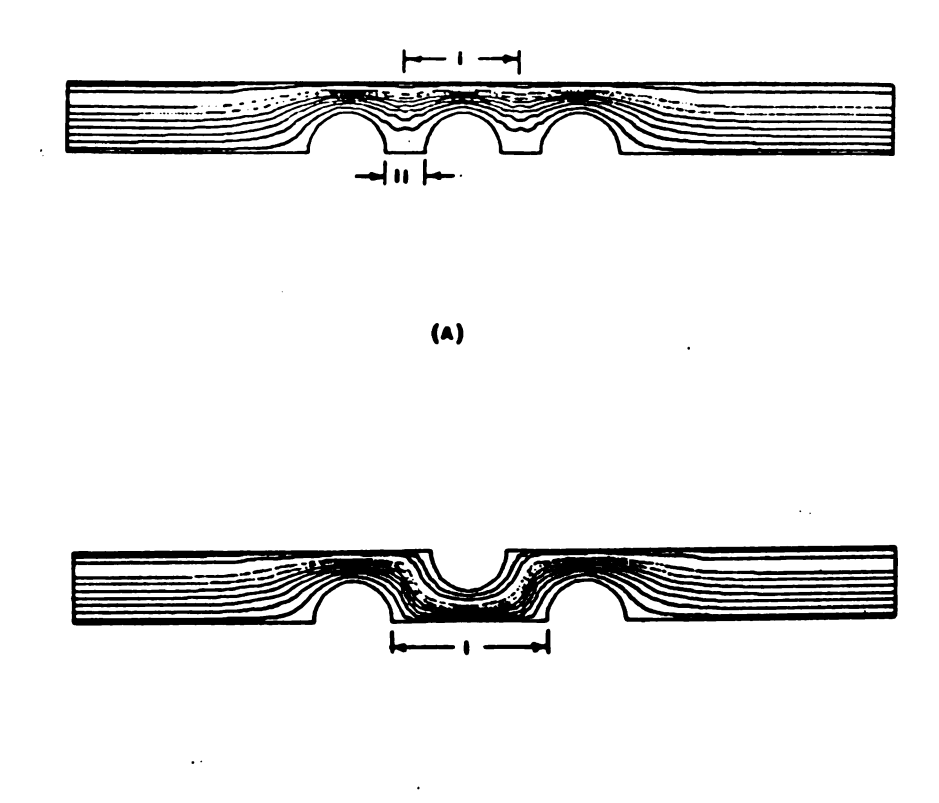
through the rectangular array at nominal strain rates ranging from 1 to 11 s⁻¹. The relaxation time changed from 0.098 s for the second sample to 0.08 s for the third sample with an insignificant change in shear viscosity. The rheological measurements were repeated after a period of two weeks and the results indicated little recovery. Molecular weight distributions were determined for the first and third samples by Odell's group and are reported in Müller *et al.* (1990). These measurements confirm that the highest molecular weight components in the fresh sample - with molecular weights of up to 32×10^6 - were lost after these runs. The highest detectable component in the degraded sample had a molecular weight of 13×10^6 .

The measurements on M1 reported in the preceding paragraph do not compare the potential for degradation of identical fresh batches in either array. This comparison was made with fresh batches of another polyisobutylene solution. The fresh polyisobutylene here had a weight average molecular weight of 1.66 x 106, leading to a relaxation time of 0.102 s for the solution. It should also be pointed out that a number of passes were required to degrade a substantial fraction of the liquid. A fresh batch of this polyisobutylene solution was passed 14 times through either array at a fixed reservoir pressure. In the case of the triangular array, the nominal strain rate was around 78 s. The relaxation time was reduced by 40% under these conditions. In the case of the rectangular array, the relaxation time was reduced only by 10%. The viscosity change was insignificant in both cases. These experimental results established the much greater extent of degradation in the triangular array for a range of PIB solutions.

4.4.4 Analysis of chain extension in arrays

It is widely recognized (see Ghoneim, 1985, for example) that the converging diverging geometry of the pores in porous media causes an extensional flow component that may be associated with the associated with the increased flow resistance for viscoelastic liquids. However, the strain required for chain scission is typically generated near stagnation points, where the fluid transit time is highest. Both the arrays in this study consist of an equal number of stagnation points. However, the experiments clearly indicate that variations in packing of cylinders at the same porosity and nominal strain rates have a profound effect on the stretching of high molecular weight polymer chains, leading to chain scission. Hence, the extent of polymer chain stretching in the two arrays, especially along the streamlines joining stagnation points, is explored analytically.

The strategy adopted here is that, close to the onset Deborah number, calculations of chain extension may be based on the Stokes flowfield. Hence, finite element simulations were carried out for two-dimensional Stokes flow within the two arrays to determine the velocity component u and the stretching component (du/dx) of the velocity gradient along segments marked in Figure 4.9. The streamline segment joining two adjacent stagnation points is chosen in either array. The length of this segment within the rectangular array is only one-fourth of the corresponding segment within the triangular array. In addition, a segment of the streamline bisecting the gap between the cylinders is chosen for the rectangular array. These segments are aligned with the bulk flow direction x; they coincide with the lines of symmetry in the mesh and with streamlines in the flow. The only non-zero component of velocity on these segments is



(D)

Figure 4.9 Streamlines computed by finite element simulation of Stokes flow through (A) the rectangular pitch array and (B) the triangular pitch array (i and ii denote selected streamline segments).

the velocity u in the bulk flow direction. This is plotted for all segments on Figure 4.10. The velocity varies from 0 to 3 times the superficial velocity over a distance of two cylinder radii along the stagnation streamline within the triangular array. There is flow reversal along the stagnation streamline in the rectangular array with rather low velocities. The velocity along the bisecting streamline in the rectangular array is much higher but the variation is significantly lower. Figure 4.11 shows that the strain rate magnitudes within the triangular array vary from 0 to 3 times the nominal strain rate while they vary from 0 to 1 times the nominal strain rate within the rectangular array. The latter variation occurs along the bisecting streamline where the velocity is at a high level throughout. The strain rates along the stagnation streamline within the rectangular array are less than 10% of the nominal strain rate. To summarize, the maximum strain rate within the triangular array occurs in the region of maximum transit time. However, the maximum strain rate within the rectangular array occurs along the streamline bisecting the gap, where the transit time is low.

We proceed to calculate the chain extension with a FENE model. The elastic liquids used in this work may be described by a FENE dumbbell model in the form used by Chilcott and Rallison (1988). This model includes a parameter L which is the ratio of fully extended dumbbell length to equilibrium length. The extensional viscosity in uniaxial extension of this model tends to a finite limit that is proportional to L^2 at high strain rates (cf. Rallison and Hinch, 1988). For example, the value of L = 10 chosen here would lead to prediction of a uniaxial extensional viscosity that is 100 times the shear viscosity. Chilcott and Rallison have shown that flow past an obstacle of a Boger

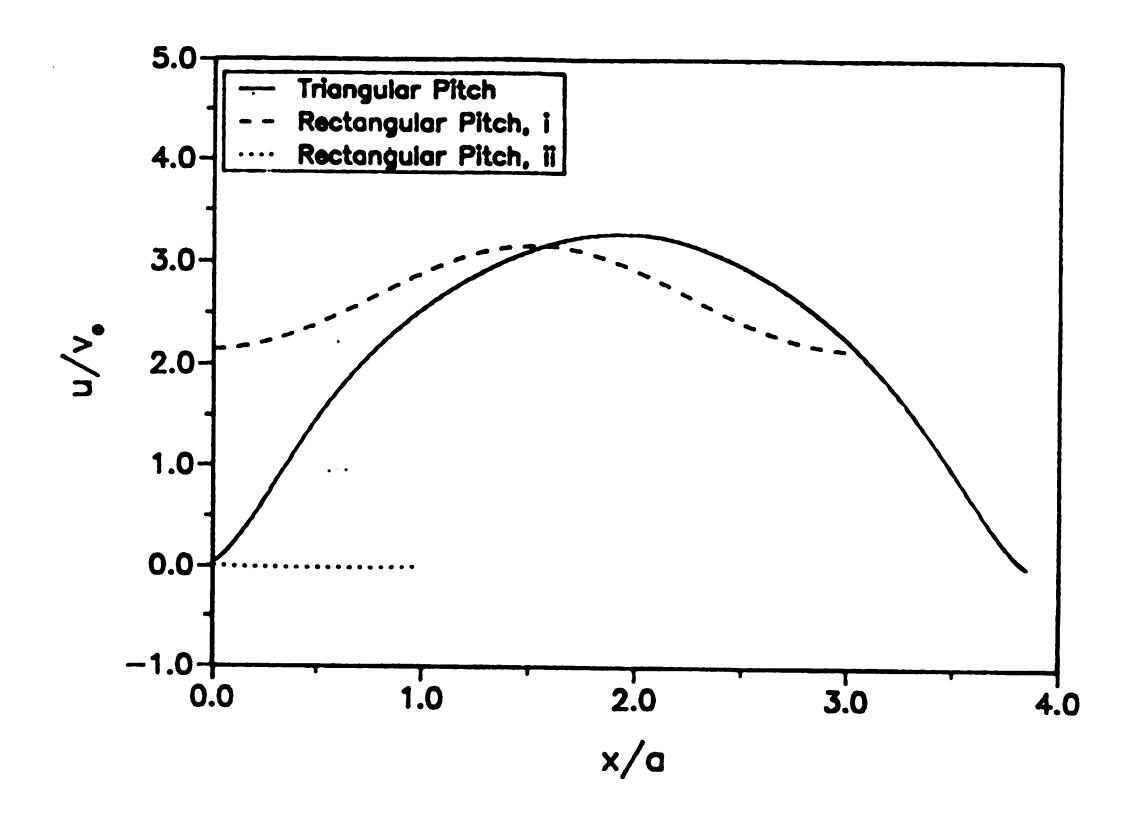


Figure 4.10 Velocity profiles along selected streamline segments (see Figure 4.9).

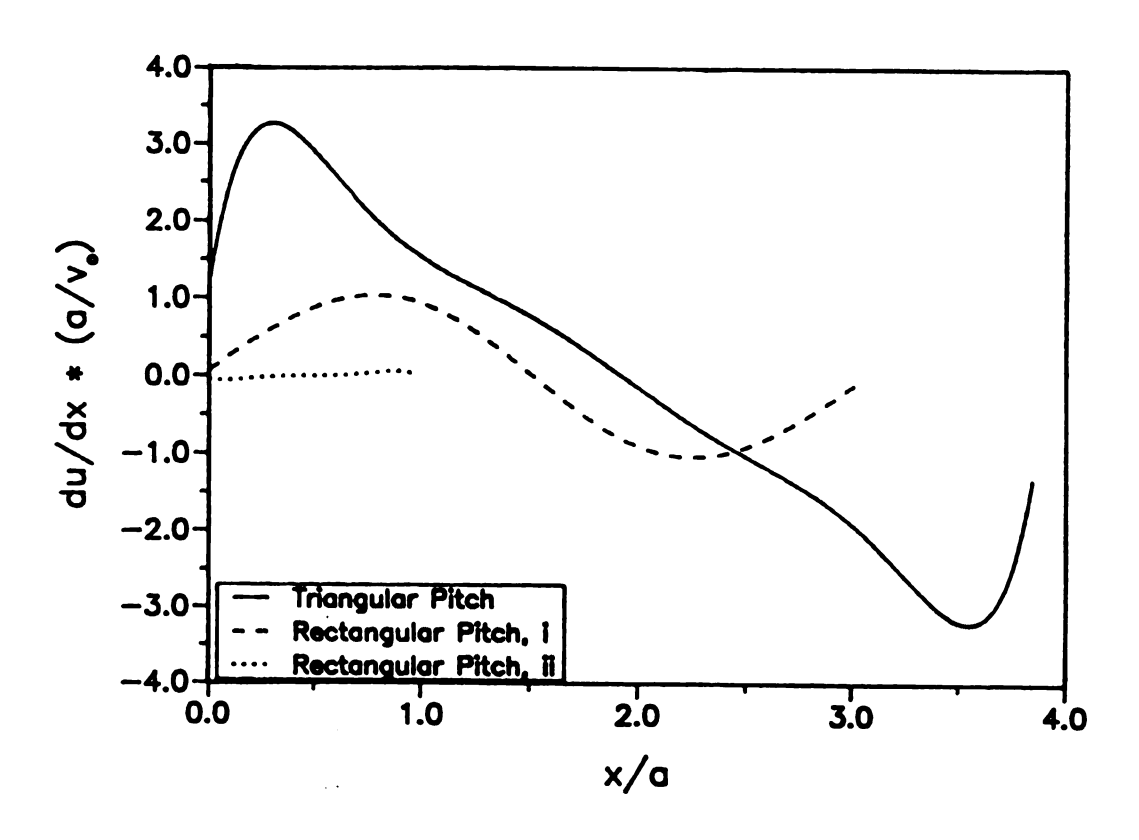


Figure 4.11 Strain rate profiles along selected streamline segments (see Figure 4.9).

liquid is modeled by values for this parameter of 3-20. It appears that similar values model the degradation behavior observed in this work.

The ordinary differential equations, which describe the evolution of the two components R_{12} and R_{22} of the normalized mean square end-to-end distance R^2 of the polymer chain, are given in Section 4.5. The normalization is such that R^2 is 1 at equilibrium. These were solved with periodic boundary conditions at the ends of the segments indicated above. A Tchebychef polynomial fit was used for the velocity along these segments. The results of these computations are plotted for Deborah numbers of 0.4 and 1 in Figures 4.12 and 4.13, respectively. Each figure shows the ratio of stretched length to equilibrium length along all three streamline segments. The curves for the two segments of the rectangular array coincide in both figures. It is clear from these figures that the chain is significantly extended only within the triangular array. The maximum stretch ratio is 5 for a Deborah number of 0.4 and 9 for a Deborah number of 1. There is virtually no extension within the rectangular array along either streamline at Deborah numbers of 1 or less. This is consistent with our experimental observations on degradation in flow of elastic liquids transverse to aligned cylinder arrays.

4.4.5 Chain extension modeling

The force law for the FENE dumbbell is given by

$$f(R) = \frac{1}{1 - \frac{R^2}{L^2}} \tag{4.6}$$

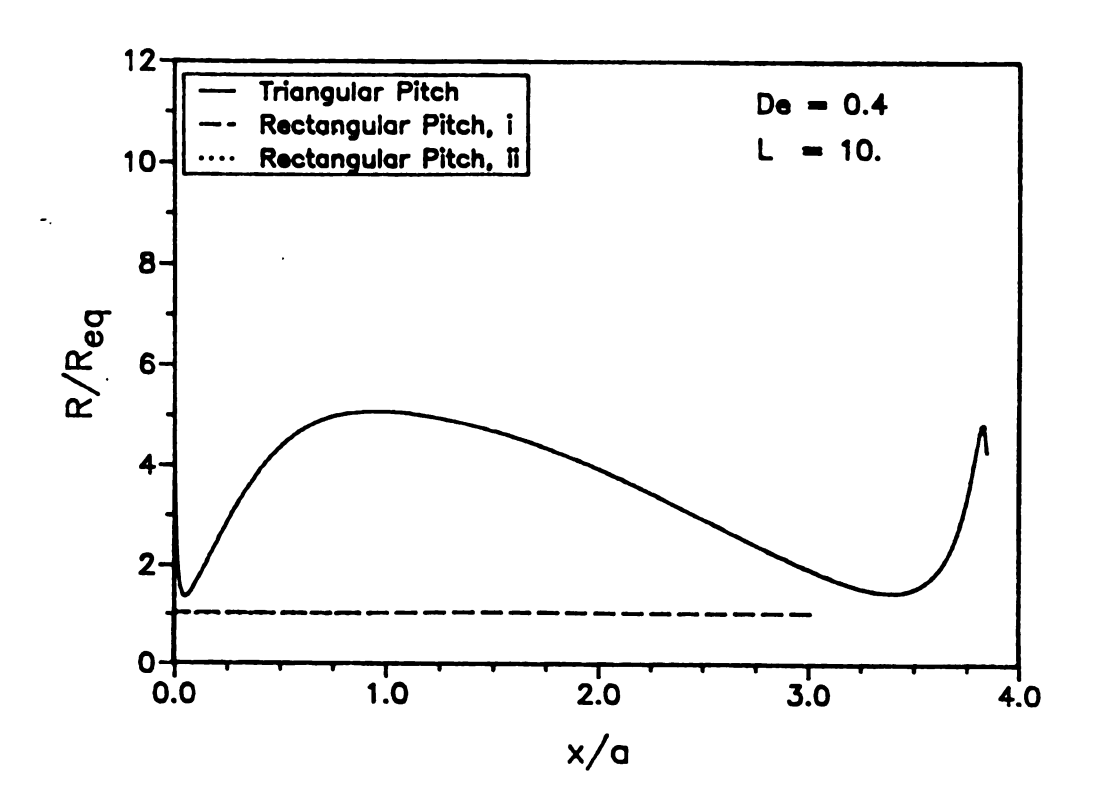


Figure 4.12 Computed stretch ratio of a polymer chain along selected streamline segments: De = 0.4.

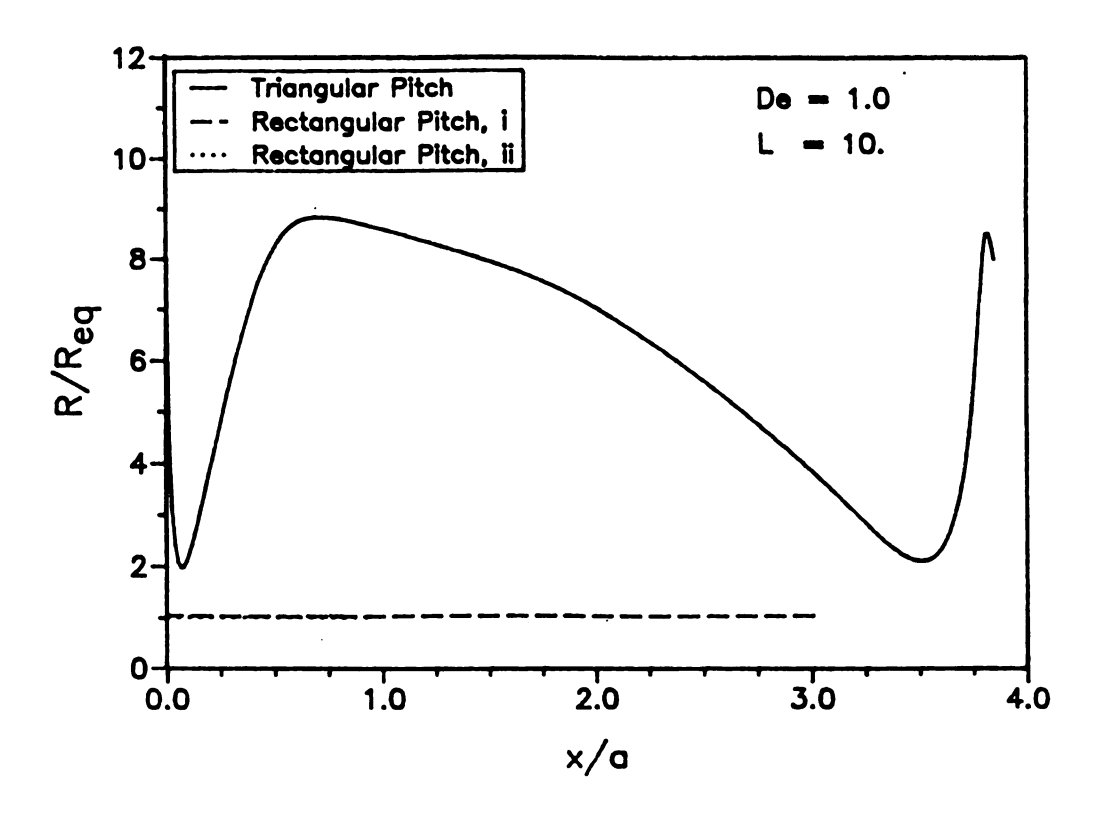


Figure 4.13 Computed stretch ratio of a polymer chain along selected streamline segments: De = 1.0.

where R² is the normalized mean end-to-end distance squared:

$$R^2 = R_1^2 + R_2^2 + R_3^2. (4.7)$$

At equilibrium

$$R^2_{eq} = \frac{1}{3}. (4.8)$$

In planar flow,

$$R_3^2 = \frac{1}{3}. {(4.9)}$$

The evolution of R_1^2 and R_2^2 along selected streamlines, where u is the only nonzero component, is described by the nondimensional differential equations (see Rallison and Hinch, 1988)

$$u\frac{dR_1^2}{dx} = 2R_1^2\frac{du}{dx} - \frac{f}{De}(R_1^2 - \frac{1}{3}), \qquad (4.10)$$

$$u\frac{dR_2^2}{dx} = -2R_2^2\frac{du}{dx} - \frac{f}{De}\left(R_2^2 - \frac{1}{3}\right). \tag{4.11}$$

The boundary conditions are periodic:

$$R_1(x=0) = R_1(x=s),$$
 (4.12)

$$R_2(x=0) = R_2(x=s),$$
 (4.13)

where 0 and s denote ends of the segment.

4.5 Conclusions

The flow of dilute solutions of polyisobutylene in polybutene transverse to unidirectional arrays of cylinders at low Reynolds numbers is sensitive to packing geometry with a fixed porosity. These liquids have a constant shear viscosity and relaxation times ranging from 0.1 to 0.2 s. The onset of elastic effects on the permeation rate or departure from Darcy's law occurs at similar values of Deborah number in the two arrays tested here. The extent of degradation of the polymer above this onset Deborah number, however, is much higher in the triangular pitch array with staggered rows than in the rectangular pitch array. Calculations of chain extension with a FENE model of the form used by Chilcott and Rallison reveal that nearly complete extension of the polymer chain occurs along streamlines joining the stagnation points in the triangular array. This is based on the fact that the maximum stretch rate within the triangular array is attained along the streamline joining the stagnation points. However, in the rectangular array, the stretch rates along the streamline joining the stagnation

points are negligible; the maximum stretch rate occurs along streamlines considerably removed from the stagnation points so that the total strain is insufficient to extend the polymer chain.

Chapter 5

VISCOSITY EFFECTS IN THE PRODUCTION OF COMPOSITE PREPREG BY HOT MELT IMPREGNATION

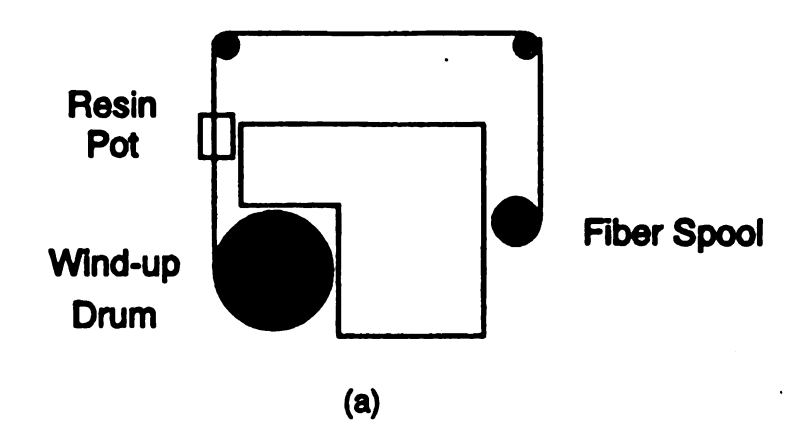
5.1 Summary

An experimental and theoretical investigation of the hot melt impregnation process is discussed. Experimental data show that when a fiber tow is pulled through a resin bath and then through a wedge shaped die, the total resin mass fraction as well as the extent of resin impregnation in the tow depend on the processing viscosity. The penetration of resin into a fiber bundle is *greater* when the resin viscosity is *higher*. This cannot be explained by capillarity, and these features are not affected by tow speeds up to 25 cm/s. A theoretical model is developed to describe the dependence of impregnation on viscosity. This model incorporates tow consolidation through both transverse compression and tension mechanisms. Good agreement with experimental observation is obtained with a viscosity dependent effective tensile modulus of the partially wetted fiber bundle.

5.2 Introduction

A key step in the manufacture of complex composite structures is the impregnation of a bundle of fibers with a liquid resin. The goal of this processing step is to fully wet all of the individual filaments which comprise the fiber tow, producing "prepreg" with a pre-determined and uniform resin mass distribution. Hot melt impregnation (HMI) is one such process (Lee et al., 1986). During hot melt impregnation, a fiber tow is unwound from a feed spool, pulled through a resin bath and then wound up on a large drum (see Figure 5.1 (a)). The actual impregnation of the fiber bundle occurs in the resin pot (see Figure 5.1 (b)) where the tow is pulled through the liquid resin, past stationary "impregnation" bars and then out through a die located at the bottom.

The stationary bars have an important role in the impregnation process. Bascom and Romans (1968) pulled a bundle of glass fibers past stationary bars submerged in epoxy resin. They observed that as the fiber bundle wound around the stationary bars, resin was squeezed into the tow while air was simultaneously squeezed out, thereby reducing the tow's void content. In a study of the HMI process, Chmielewski et al. (1988) found that when impregnation bars are employed, the resin mass fraction of the prepreg product is independent of both the processing viscosity and speed. Lee et al. (1988a) have made similar observations with an identical HMI process. These results are in contrast to those obtained when the impregnation bars are not employed. When prepregging without impregnation bars, lower prepreg resin mass fractions are obtained,



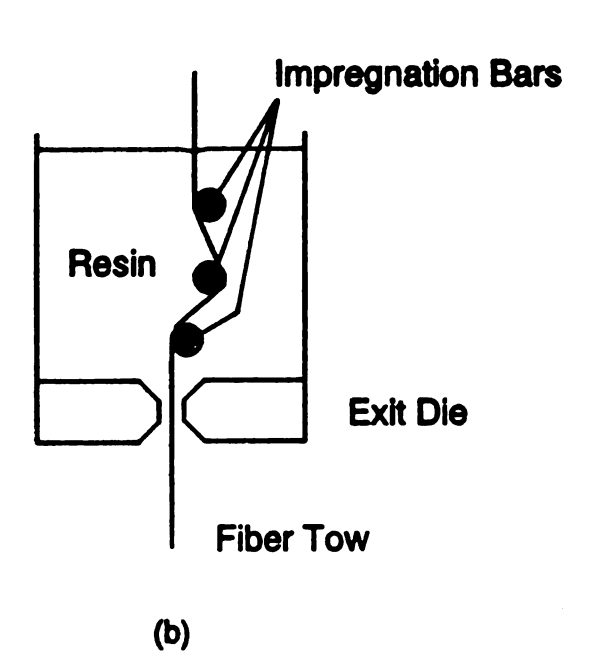


Figure 5.1 Hot melt impregnation (a) schematic of the hot melt prepregger (b) schematic of the resin pot.

and the resin mass fraction is dependent on the resin viscosity during processing. Greater resin viscosities produced prepreg with higher resin mass fractions. However, the effect of tow speed on the resin mass fraction remains insignificant (see Figure 5.2).

The impregnation bars have one further effect on the HMI process and that is to reduce the maximum tow speed at which the process can operate. Chmielewski et al. (1988) found that without the bars, speeds of 25 cm/s could be attained, but with the bars, line speeds greater than 10 cm/s result in the fiber tow fraying and incipient breakage at the die. Also, a combination of higher resin viscosities with the bars caused the tow to break at even lower speeds. Using impregnation bars, Lee et al. (1988a) also found increased tow damage and breakage as larger resin viscosities and line speeds were employed. They attribute this to increased shear stress and friction within the exit die alone. However, the above results suggest that greater drag around the impregnation bars, resulting from higher viscosities and tow speeds, promotes fraying of the fiber tow and then eventual breakage in the die.

Therefore, at fast processing rates that are typically necessary in order to produce relatively low cost materials, the HMI process is most efficiently operated without the impregnation bars. This investigation has been undertaken with the ultimate goal of increasing the HMI processing rate by removing the impregnation bars, and yet still producing quality prepreg. This can be accomplished only by understanding both the impact of processing conditions and the role of the exit die on the impregnation of a fiber bundle.

Experimental work has been done to reveal the distribution of resin within a fiber

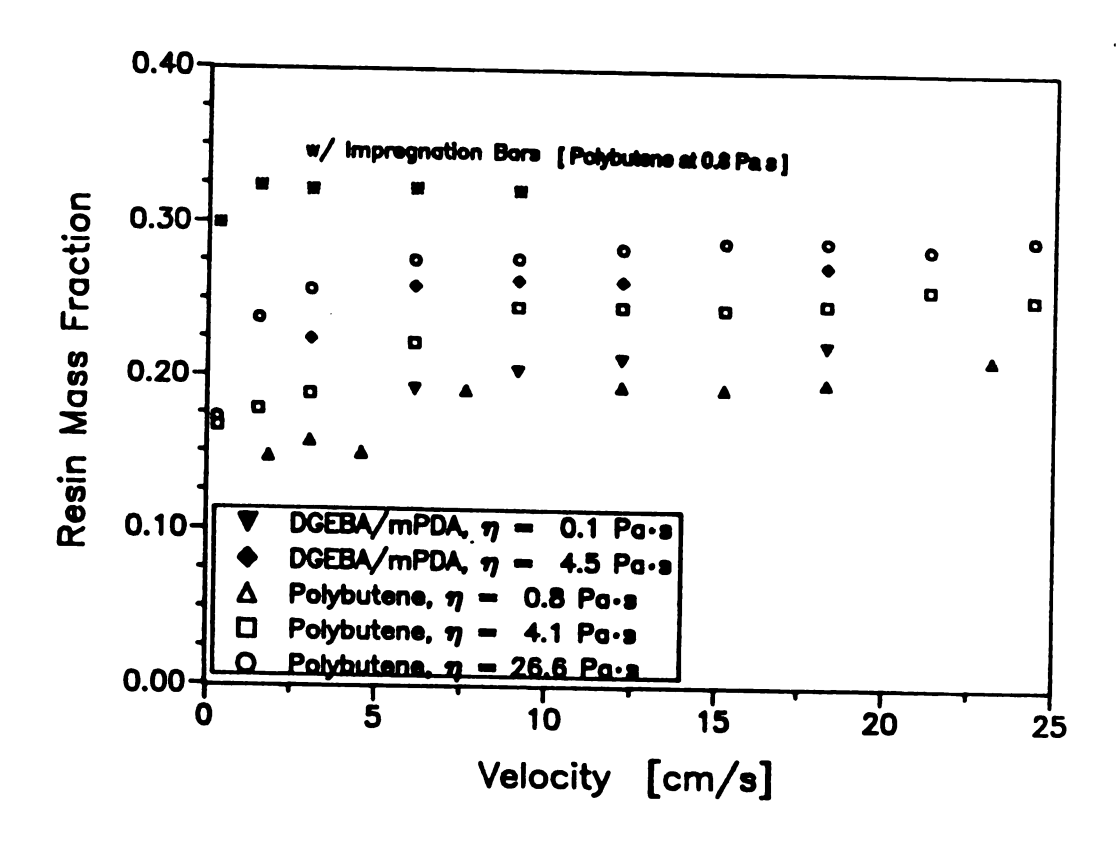


Figure 5.2 Resin mass fraction dependence on tow velocity and resin viscosity.

bundle when a tow is passed through epoxy resins of widely different viscosities. A lubrication model is developed to explore the role of the exit die in fiber impregnation. This model incorporates tow consolidation by means of a compressive force due to hydrodynamic loading and a tensile force resulting from drag on the tow as it travels through the die.

5.3 Experimental

The effect of processing conditions on the resin content of composite prepreg is studied via a bench scale hot melt prepregger (Model 30, Research Tool Corporation). Resin content measurements are made on prepreg processed at speeds ranging from 0.5 to 25 cm/s and with resin viscosities ranging from 0.1 to 26.6 Pa·s. Resin viscosities are controlled by regulating the resin pot temperature. Prepreg resin mass fraction is calculated from gravimetric measurements made on tow pieces, 20 cm long, cut from the tape exiting the resin pot. The resins used in this study are a Newtonian, high viscosity polybutene liquid (Amoco Indopol H300) and an epoxy resin system. The epoxy is diglycidyl ether of bisphenol-A (DGEBA) and it is mixed in stoichiometric proportions with m-phenylenediamine (mPDA). A 12k tow of Hercules AS4 carbon fibers constitutes the reinforcement phase.

In order to assess how the resin is distributed, between fiber bundle coating and bundle penetration, photographs of the cross section of the fiber tows impregnated with the epoxy resin were taken. Two fiber tow samples processed at 18.3 cm/s but at

different viscosities, 4.5 Pa·s and 0.1 Pa·s, were cured at room temperature for 48 hours while being held at the same tension observed during processing. Cross sections of the cured tow samples were cut and mounted in a quick setting epoxy. These samples were then polished and photographed at a magnification of 12.5x.

5.4 Resin mass fraction and distribution

The experimental results of Figure 5.2 indicate that the resin content of a prepreg tape is nearly independent of the rate at which it is processed. However, these same results show a significant viscosity effect on the resin content. As the processing viscosity is varied from 0.1 Pa ·s to 26.6 Pa ·s the prepreg resin mass fraction increases from 19 to 28 percent. Since the data presented in Figure 5.2 offer no information on the distribution of resin between the surface and the interstices of the impregnated fiber tow, photographs of the cross section of the epoxy impregnated fiber tow were taken (see Figure 5.3). In Figure 5.3, the dark areas within the tows are regions void of resin while the white portions of the tow are resin impregnated areas; at this magnification individual fibers cannot be resolved. The dark regions surrounding the fiber tows, however, are not void of resin and yet still prevent the measurement of resin coating thickness. However, a comparison of resin penetration can be made. A qualitative comparison between Figures 5.3 (a) and 5.3 (b) reveals that higher resin viscosities lead to greater penetration of resin into the fiber bundle! The void content of the fiber tape manufactured with a resin viscosity of 0.1 Pa·s is much higher (dark areas in Figure 5.3

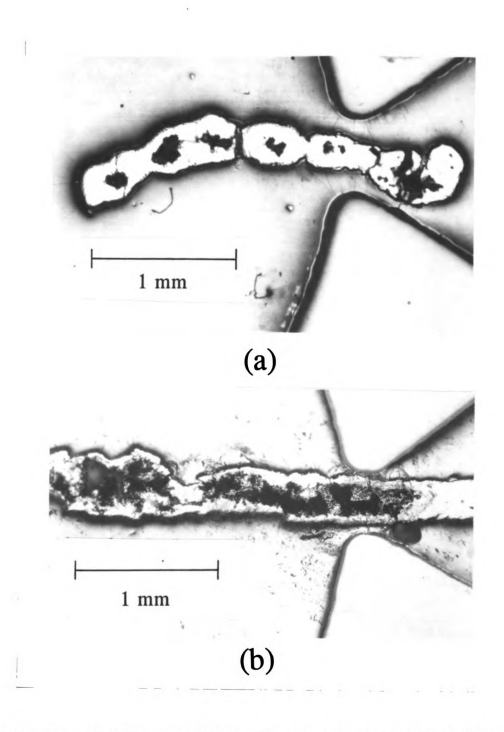


Figure 5.3 Two 12k AS4 carbon fiber tows impregnated with a DGEBA/mPDA epoxy resin system under the following processing conditions: tow velocity = 18.3 cm/s (a) resin viscosity = 4.5 Pa·s (b) resin viscosity = 0.1 Pa·s.

(b)) than that manufactured using a resin viscosity of 4.5 Pa·s (Figure 5.3 (a)), even though the capillary number of the former situation is much lower, 0.4, than the latter, 18.0. Thus, capillarity certainly cannot account for the differences in resin penetration.

5.5 Mathematical modeling

To assist in the understanding of the observed viscosity effect on prepreg quality a mathematical model is developed, describing the flow processes within the exit die. A lubrication model is used to describe the liquid flow within the die proper while Darcy's law is employed to control the penetration of liquid into the fiber tow. Because the fiber tow is not rigid but compliant, its response to external forces is also considered, and modeled as that of a non-linear spring. The elastic response of a fiber network saturated with resin is an important physical phenomena in all types of composite processes, and is used in this study to explain how larger processing viscosities result in prepreg with greater resin penetration.

5.5.1 Tow consolidation models

Fiber tow consolidation is accounted for through two mechanisms: (1) transverse compression, and (2) tension. The hydrodynamic pressure developed in the die as a result of its converging geometry will place a compressive load on the fiber bundle, resulting in higher fiber volume fractions. Likewise, the pulling force needed to move the tow through the die at a constant velocity will place a tensile stress on the fibers

causing them to straighten and consolidate, also increasing the fiber volume fraction.

Gutowski et al. (1987) have modeled compressive loadings on composite laminates by making an analogy between the deformation of a fiber in a network of fibers and beam deflection. This resulted in the following relationship for the elastic deformation of composite laminates under a compressive load, $P_c^*(x^*)$,

$$P_{c}^{*}(x^{*}) = \kappa_{c}^{*} \frac{\sqrt{\frac{V_{f}(x^{*})}{V_{o}}} - 1}{\left[\sqrt{\frac{V_{a}}{V_{f}(x^{*})}} - 1\right]}, \qquad (5.1)$$

where V_a is the available fiber volume fraction (0.907 for hexagonally packed cylinders), V_o is the inlet fiber volume fraction and κ_e^* is the spring constant. This relationship, along with the experimentally determined value of $\kappa_e^* = 158.6$ Pa for well aligned AS4 carbon fibers (Gutowski *et al.*, 1987), is used in this study.

Where the transverse consolidation mechanism provides for non-uniform fiber volume fraction profiles, a consolidation mechanism based on fiber tension is developed to provide the inlet fiber volume fraction. To develop a tension consolidation model, we assume that under a tensile force, each fiber comprising the tow will support the load equally. Furthermore, we assume that as the tensile force increases, the tow will consolidate uniformly. An iterative procedure, described in Section 5.5.3, is employed to relate the tension on the fiber tow to the inlet fiber volume fraction. A relationship, similar to Eq. 5.1, is constructed by making an analogy between fiber load bearing and

the mechanics of column buckling (Gere and Timoshenko, 1984). Figure 5.4 shows schematically a portion of a fiber located within a network of fibers. In the stress free state the fiber is buckled and makes several contacts with surrounding fibers. If a length l of this fiber is isolated between adjacent contact points and subjected to a tensile force, F_T^* , the fiber's response is to straighten. This process is modeled as if the fiber were a buckled column responding to an axial tensile load where,

$$F_T^* \propto 1^{-2}$$
 (5.2)

Using similar geometric arguments as Gutowski (1985), the relation between the tensile force acting on the fiber tow and the inlet fiber volume fraction is,

$$F_T^* = \kappa_T^* \frac{\frac{1}{V_{\min}} - \frac{1}{V_o}}{\left[\frac{1}{V_o} - \frac{1}{V_o}\right]^2} , \qquad (5.3)$$

where κ_T^* is the effective tensile modulus associated with the tensile force and V_{min} is the fiber volume fraction based on the cross sectional area of the die ($V_{min} = 0.65$ for these experiments). The term ($1/V_{min} - 1/V_o$) in the numerator has been included to preserve the conservation of fibers within the die when the fiber bundle is free of a tensile force. Figure 5.5 illustrates the relationship, given by Eq. 5.3, between the inlet fiber volume fraction and the ratio of the tow's tension to its modulus. It shows that in the limit of

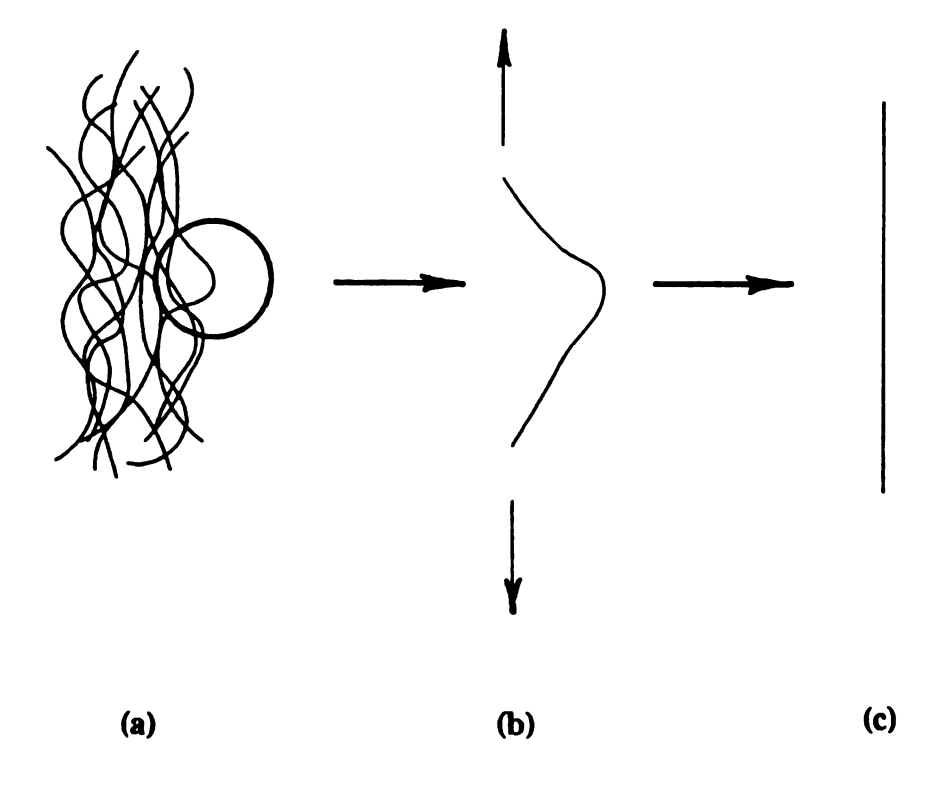


Figure 5.4 An illustration of the straightening of a portion of a bent fiber isolated from a network of fibers; (a) the buckled portion of fiber under consideration in an unstressed fiber network; (b) as the fiber network is placed under tension, the fiber portion of interest takes up some of the load; (c) the result is that the fiber straightens.

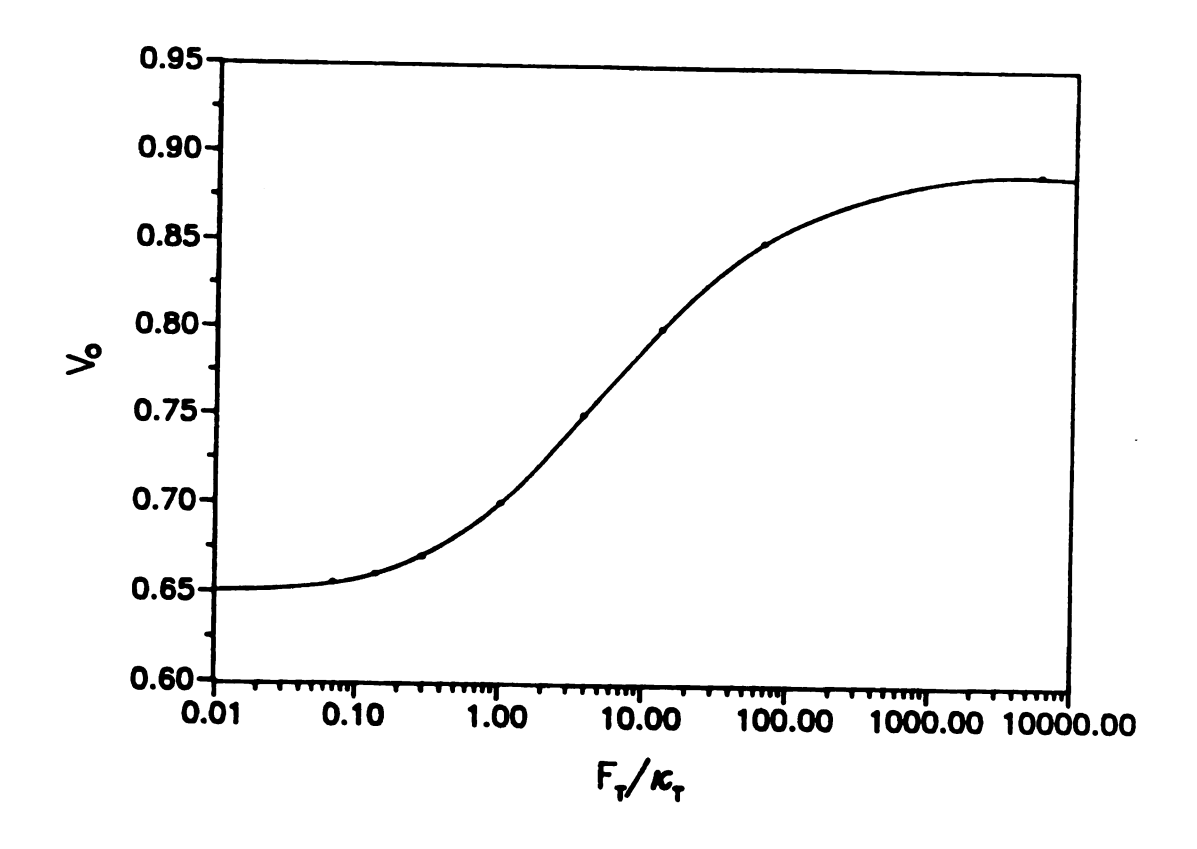


Figure 5.5 Model non-linear tow consolidation behavior as a result of tension on the fiber tow.

small forces, V_o approaches V_{min}, while in the limit of large forces, V_o approaches V_a.

5.5.2 Impregnation model

Figure 5.6 defines the class of impregnation dies studied. The wedge die geometry is characterized by the die length, L, the half gap, $\%W_2$, and the die half angle θ . The specific shape of the die is given by the distance between the die wall and the centerline of the die:

$$H + 1 = \frac{L}{\frac{1}{2}W_2} \tan(\theta) (1 - x) + 1 , \qquad (5.4)$$

where the x coordinate is scaled with L and H is scaled with $\frac{1}{2}W_2$. The remaining variables of interest are scaled in the following way:

$$P^{\circ} = P\tau_{\circ} \qquad \tau_{\circ} = \eta U_{\circ}/(\frac{1}{2}W_{2}) \qquad (5.5a,b)$$

$$u^* = uU_o$$
 $y^* = y(\frac{1}{2}W_2)$ (5.6a,b)

$$s_1^* = s_1(\frac{1}{2}W_2)$$
 $s_2^* = s_2(\frac{1}{2}W_2)$ (5.7a,b)

$$F^{\bullet} = 2F\tau_{o}W_{1}L$$
 $Q^{\bullet} = Q(\frac{1}{2}W_{2})U_{o}$ (5.8a,b)

$$\kappa_c^{\bullet} = \kappa_c \tau_o \qquad \qquad \kappa_T^{\bullet} = 2\kappa_T \tau_o W_1 L \qquad (5.9a,b)$$

Here the asterisks indicate dimensional quantities, and U_o is the tow velocity, W_I is the die width, F^o is the force needed to pull the tow at speed U_o and Q^o is the fluid phase

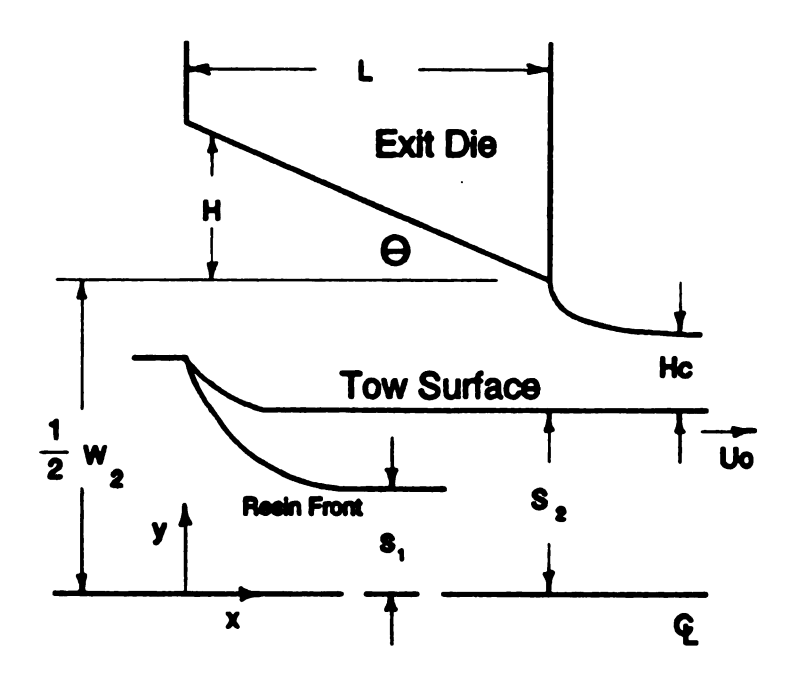


Figure 5.6 Wedge die geometry.

flow rate per unit width. τ_o is a characteristic stress and represents the wall shear stress for pure Couette flow with a uniform gap $\frac{1}{2}W_2$. A nominal value for τ_o is 237.2 Pa, based on a typical HMI line speed of 4.6 cm/s and resin viscosity of 0.41 Pa·s. The fiber tow profile is given by $s_2(x)$ and the impregnated region by $(s_2 - s_1)$.

A lubrication approximation (see Denn, 1980, for example) is used to simplify the equation of motion, yielding the following expression for the axial component of the resin velocity and the shear stress at the tow-resin interface:

$$u = 1 - \frac{y - s_2}{(H+1) - s_2} + \frac{1}{2} \frac{\frac{1}{2} W_2}{L} \frac{dP}{dx} [(y^2 - s_2^2) - (y - s_2) ((H+1) + s_2)]$$
(5.10)

$$-\tau_{xy}|_{y=s_2} = \frac{1}{(H+1)-s_2} + \frac{1}{2} \frac{\frac{1}{2}W_2}{L} \frac{dP}{dx} [(H+1)-s_2]$$
 (5.11)

These expressions are derived by satisfying the no-slip conditions at the tow surface and at the die wall. It should be noted that Beavers and Joseph (1967) propose a slip boundary condition to be used at the interface of a permeable surface. The work of Taylor (1971) and Richardson (1971), however, indicates that at the fiber volume fractions of interest here (> 50 %) this condition is unnecessary. The first two terms in Eq. 5.10 are due to Couette flow caused by the moving tow, whereas the third contribution stems from an induced Poiseuille flow due to the wedge geometry. The force needed to pull the tow through the die is calculated by:

$$F = \int_{0}^{1} -\tau_{xy}|_{y=s_{2}} dx \qquad (5.12)$$

Mass balances on the resin within the die gap and the tow yield the following results:

$$\frac{\frac{1}{2}W_2}{L}\frac{d}{dx}Q = \begin{bmatrix} -u_D, & \text{for } s_1 > 0 \\ 0, & \text{for } s_1 = 0 \end{bmatrix}$$
 (5.13)

$$\frac{\frac{1}{2}W_2}{L} \frac{d}{dx} [(s_2 - s_1) (1 - V_f)] = \begin{bmatrix} +u_D & , & \text{for } s_1 > 0 \\ 0 & , & \text{for } s_1 = 0 \end{bmatrix}$$
 (5.14)

In the above expressions, $s_1(x)$ represents the resin impregnation front within the fiber bundle, where $s_1(x) = 0$ indicates a fully impregnated tow, and $V_j(x)$ is the fiber volume fraction. The resin phase flow rate is represented by:

$$Q = \int_{a_2}^{H+1} u(x, y) \, dy \tag{5.15}$$

The normal component of the resin velocity, u_D , at the tow interface is related to the local transverse pressure drop within the tow by using Darcy's law:

$$u_{D} = K_{T} \left[\frac{P - (p_{z} - \Gamma)}{S_{2} - S_{1}} \right]$$
 (5.16)

In the above expression K_T is the transverse permeability, Γ is the resin pressure due to capillarity and p_a is the atmospheric pressure. The longitudinal flow of resin within the fiber bundle as the result of a local axial pressure gradient will be neglected. Only the case where the tow velocity is much greater than the longitudinal Darcy velocity is considered.

The Blake-Kozeny-Carman equation (Bird et al., 1960) is used to relate the transverse permeability to the fiber volume fraction:

$$K_T = \frac{(1 - V_f)^3}{V_f^2} \frac{1}{4 k(V_f)} r_f^2$$
 (5.17)

where the dependence of the Kozeny constant, $k(V_j)$, on the fiber volume fraction is based on model calculations of a Newtonian fluid flowing through an infinite array of circular cylinders (Sangani and Acrivos, 1982). The fiber radius is r_j .

The capillary pressure is given by:

$$\Gamma = \frac{2\pi\cos\left(\phi\right)}{N_{Ca}r_{f}}\tag{5.18}$$

The resin-fiber contact angle is represented by ϕ , and N_{Ce} is the capillary number:

$$N_{Ca} = \frac{\eta U_o}{\gamma_{rf}} \tag{5.19}$$

where γ_{rf} is the resin-fiber surface tension. Variables found in Eqs. 5.16-5.19 are scaled as follows:

$$u_D^* = u_D U_o$$
 $K_T^* = K_T (\frac{1}{2}W_2)^2$ (5.20a,b)

$$\Gamma^{\bullet} = \Gamma \tau_{o} \qquad \qquad \Gamma_{f}^{\bullet} = \Gamma_{f}(\frac{1}{2}W_{2}) \qquad (5.21a,b)$$

For these calculations γ_{rf} is taken to be the surface tension of DGEBA (44 dynes/cm at 60 °C) as determined by the pendant drop method (Weaver, 1982). It is more difficult to find a value for ϕ , however. Because impregnation flows are non-equilibrium processes, the dynamic contact angle, and not the static one, is more important when describing the advancing liquid flow front. Inverarity (1969) studied the wetting of glass and polymeric fibers with viscous liquids and found that the advancing contact angle is a complex function of both the fiber velocity and the fluid viscosity. We will take 35° to be the nominal value of ϕ (Lee *et al.*, 1988b), and note, that although Ahn *et al.*

(1991) found significant interfacial effects when impregnating a woven fabric reinforcement at high fiber loadings ($V_f > 0.50$), the capillary pressure had little influence on the results of these model calculations at the N_{Cs} levels studied here.

Eqs. 5.13-5.19 constitute the physical model used to find the pressure, impregnation and flow rate profiles within the die. To this end, Eqs. 5.13-5.15 are rearranged as:

$$\frac{d}{dx}P = \frac{L}{\frac{1}{2}W_2}\beta(x)\left[2Q - [(H+1) - S_2]\right]$$
 (5.22)

$$\frac{d}{dx}S = 2\frac{L}{\frac{1}{2}W_2}K_T(1-V_f)[P-(p_a-\Gamma)]$$
 (5.23)

$$Q = Q_o + \sqrt{S_o} - \sqrt{S} \tag{5.24}$$

where

$$\beta(x) = \frac{-6}{[(H+1)-s_2]^3}$$
 (5.25)

In Eq. 5.23 the effective impregnation is represented for convenience by the quantity:

$$S = [(s_2 - s_1) (1 - V_f)]^2$$
 (5.26)

Eqs. 5.22-5.24 are analyzed according to the following boundary conditions:

(i)
$$P = P_0 = 0$$
 at $x = 0$ (5.27)

(ii)
$$S = S_0 = 0$$
 at $x = 0$ (5.28)

and

(iii)
$$P = p_a = 0$$
 at $x = 1$ (5.29)

Neglecting the liquid head in the resin pot, no net pressure drop will be imposed across the die. Also, for the situations studied experimentally in this paper, $N_{Cs} > 0.4$ and the tow residence time in the liquid bath is at most three seconds. Hence, it will be assumed the tow entering the die contains no resin. This boundary condition allows for the study of the factors which affect the impregnation process within the die proper.

5.5.3 Solution procedure

These equations are solved by a semi-implicit Runga-Kutta method with variable step size (Michelsen, 1976 and Villadsen and Michelsen, 1978). At x = 0, the conditions for P and S are provided, and an initial guess for the inlet flow rate, Q_o , is obtained from the non-porous situation (Middleman, 1977). Also, initially a constant tow profile is assumed, $s_2 = s_{2o}$ for all x. A shooting strategy is employed to reach the boundary condition at x = 1. A means of updating Q_o for the ensuing iteration is obtained by integrating Eq. 5.22 over the die length and then rearranging the result.

This leads to the following integral property for Q:

$$Q_{o} = \frac{1}{\int_{0}^{1} \beta(x) dx} \left[\int_{0}^{1} \beta(x) (\sqrt{S} - \sqrt{S_{o}}) dx + \frac{1}{2} \int_{0}^{1} \beta(x) [(H+1) - S_{2}] dx \right]$$
(5.30)

The calculation strategy entails three nested iteration loops in order to find the pressure, impregnation, flow rate and tow profiles. During the inner iteration loop, a constant tow profile $s_2(x)$ is assumed and Eqs. 5.22-5.24 are repeatedly solved to find the correct inlet flow rate. The pressure profile resulting from this calculation is then used to evaluate the transverse consolidation. Eq. 5.1 utilizes the local hydrodynamic pressure in the die to calculate the local fiber volume fraction. The revised tow profile, $s_2(x)$, is found by recognizing that the cross sectional area of the tow fibers are conserved:

$$s_2(x) = s_1(x) + \frac{V_o}{V_f(x)} (s_{2o} - s_1(x))$$
 (5.31)

Subsequently, this updated tow profile is used to find new pressure, impregnation and flow rate profiles.

In the outermost iteration loop, the fiber tension is determined by Eqs. 5.11 and 5.12, and Eq. 5.3 is used to amend the inlet fiber volume fraction, V_o . Then a revised

inlet tow position is found by again recognizing that the cross sectional area of the fibers passing through the die is conserved:

$$s_{2o} = \frac{V_{\min}}{V_o} \tag{5.32}$$

5.6 Calculation results and discussion

Figures 5.7 (a), (b) and (c) show several pressure, impregnation and flow rate profiles based on the following dimensionless parameters:

$$\theta = 15^{\circ}$$
 $L/(\frac{1}{2}W_2) = 69.2$ (5.33a,b)

$$r_{r}/(\frac{1}{2}W_{2}) = 0.05$$
 $V_{o} = 0.76$ (5.34a,b)

$$V_a = 0.90$$
 $\kappa_c = 0.67$ (5.35a,b)

These parameters correspond to the design and operating conditions used in the experiments of Figures 5.2 and 5.3. (Although the correct shape of the experimental exit die is a wedge followed by a short rectangular slit region, previous calculations indicate that the rectangular region has little effect on the computed profiles.) The actual die dimensions and fiber radius are:

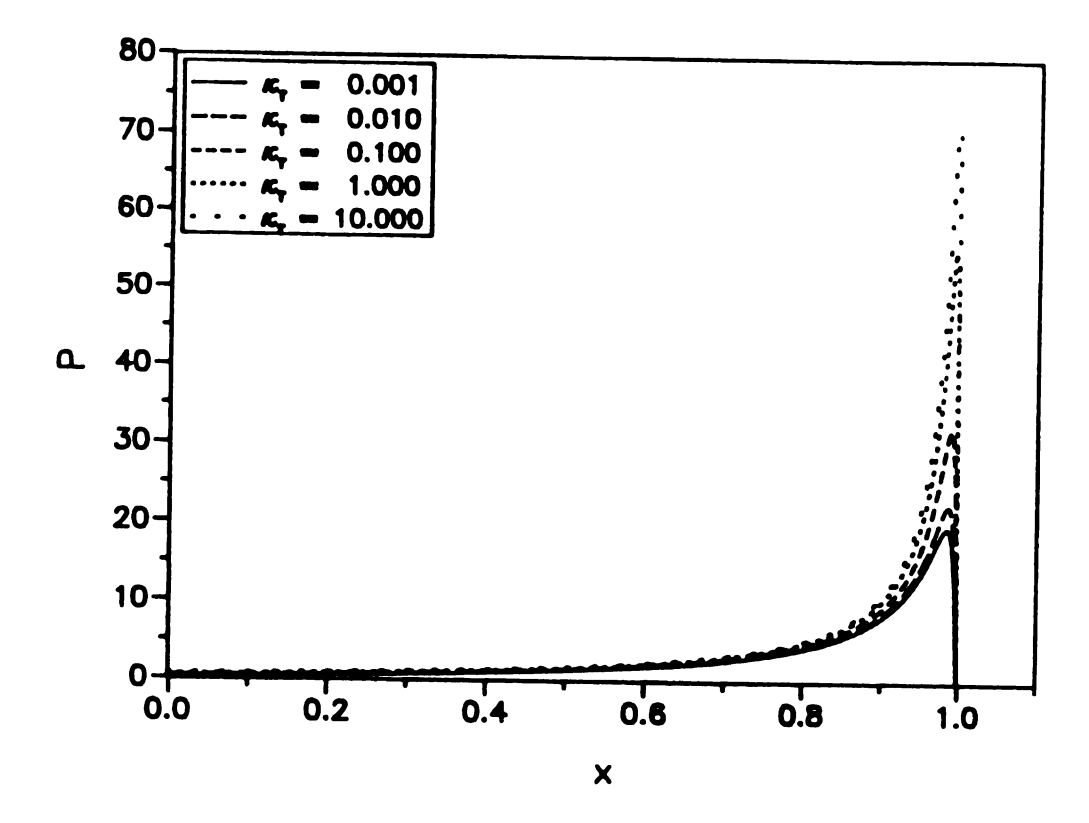


Figure 5.7 (a) Calculated pressure profiles for several different values of the effective tensile modulus.

$$W_2 = 0.0159 \text{ cm}$$
 $L = 0.550 \text{ cm}$ (5.36a,b)

$$W_1 = 0.5588 \text{ cm}$$
 $r_f = 3.9 \times 10^4 \text{ cm}$ (5.37a,b)

Figure 5.7 (a) shows that the peak pressure is strongly dependent on the fiber bundle's effective tensile modulus. As κ_T is increased from 0.001 to 10.0 the peak pressure increases from 20 to 70 times the characteristic stress. Over this range of κ_T the calculated dimensionless tensile force on the fiber tow changes from 0.60 to 0.87 (8.7 to 12.7 mN or 2.2 to 3.2 psi for a 12k fiber tow moving at 4.6 cm/s through a 0.41 Pa·s viscosity resin). Thus, as κ_T is increased by 4 orders of magnitude the ratio F_T/κ_T decreases nearly the same amount and, as is shown in Figure 5.5, the inlet fiber volume fraction decreases. This leads to smaller clearances between the tow and the die (Eq. 5.32). And, similar to the non-porous lubrication flows (Middleman, 1977), the peak pressure in the die is sensitive to this gap, where smaller gaps result in larger pressures.

The pressure profiles of Figure 5.7 (a) also show that the greatest contribution of the pressure loading on the tow occurs in the last 15 percent of the die. As a result, tow consolidation due to the transverse loading has an insignificant effect on the calculated resin mass fraction of the tow. For example, for the situation where the peak pressure is the greatest, $\kappa_T = 10.0$, the outlet fiber volume fraction is less than 8 percent greater than the inlet value.

On the other hand, the impregnation profiles of Figure 5.7 (b) show that the

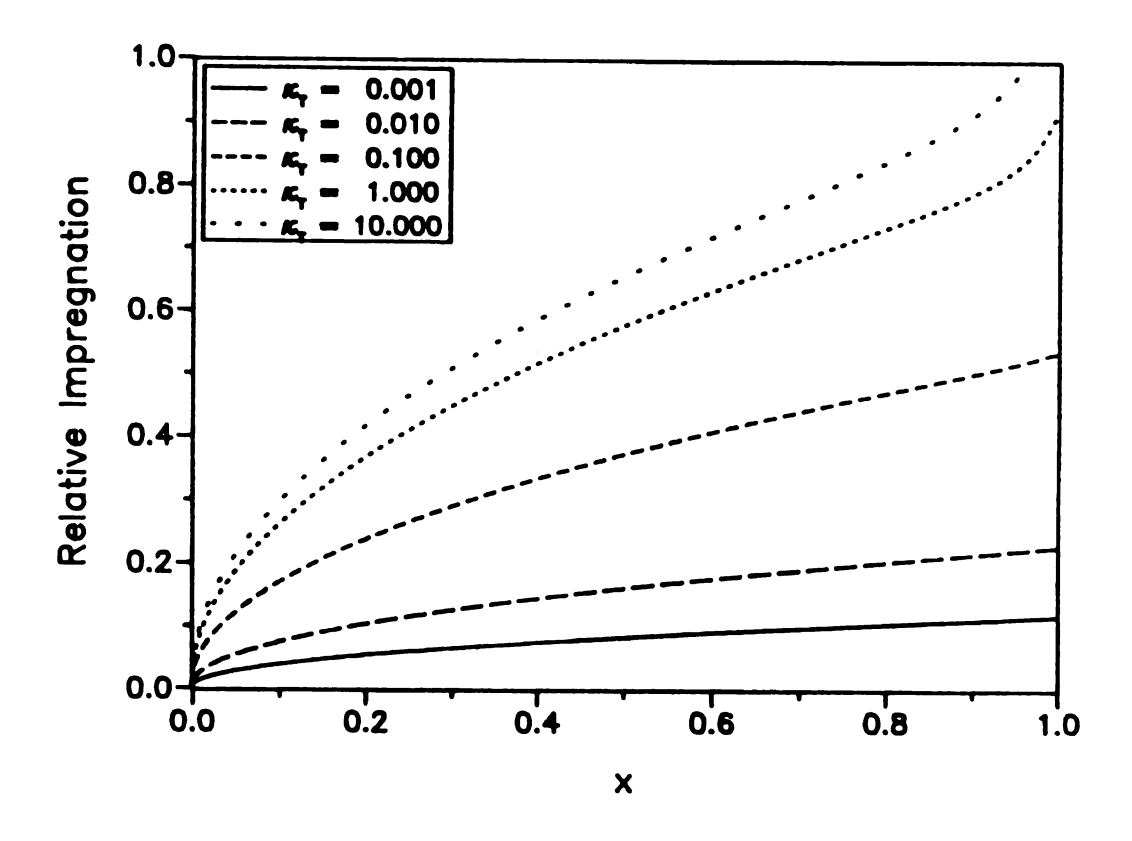


Figure 5.7 (b) Calculated impregnation profiles for several different values of the effective tensile modulus.

calculated fiber tow penetration is sensitive to fiber tension effects. The increase in tow impregnation with κ_T at each location along the die can be explained by again noting the decrease in V_o with increases in κ_T . As the fiber volume fraction decreases, both the transverse permeability of the tow and the hydrodynamic pressure in the die will increase. According to Darcy's law (Eq. 5.16), this will result in higher resin penetration rates.

Figure 5.7 (c) presents the dimensionless resin phase flow rate profiles. At each location along the die the flow rate decreases with increasing κ_T , opposite to the trend in Figure 5.7 (b), in order to preserve the mass balance. The decrease in Q along the length of the die for each value of κ_T reflects the loss of fluid from the resin phase to the tow. However, at x = 0.97 for the $\kappa_T = 10.0$ curve, the flow rate profile changes from a decreasing function of x to an increasing function. At this location, the tow is fully impregnated and yet still is being consolidated by the hydrodynamic pressure. The tow consolidation causes fluid to move from the fiber bundle into the resin phase, resulting in an increase in Q.

Figure 5.8 (a) shows model calculation results on how the resin coating and resin impregnation depend on the effective tensile modulus. These results are combined in Figure 5.8 (b) which presents the predicted resin mass fraction versus the effective tensile modulus. Varying the modulus from 0.06 to 10 results in an increase in the predicted resin mass fractions from approximately 20 to 27 percent. This is similar to the mass fraction changes observed experimentally by varying the resin viscosity from 0.1 Pa·s to 26.6 Pa·s (Figure 5.2). Moreover, Figure 5.8 (a) shows that this increase

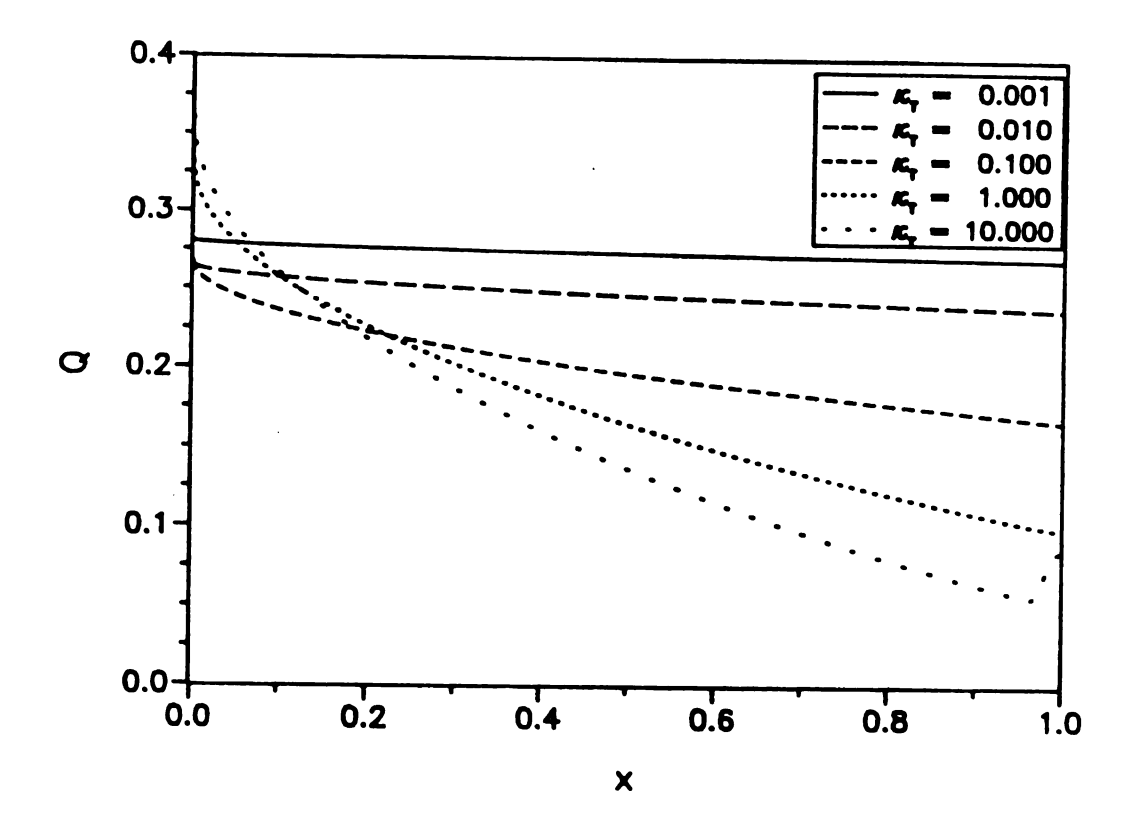


Figure 5.7 (c) Calculated flow rate profiles for several different values of the effective tensile modulus.

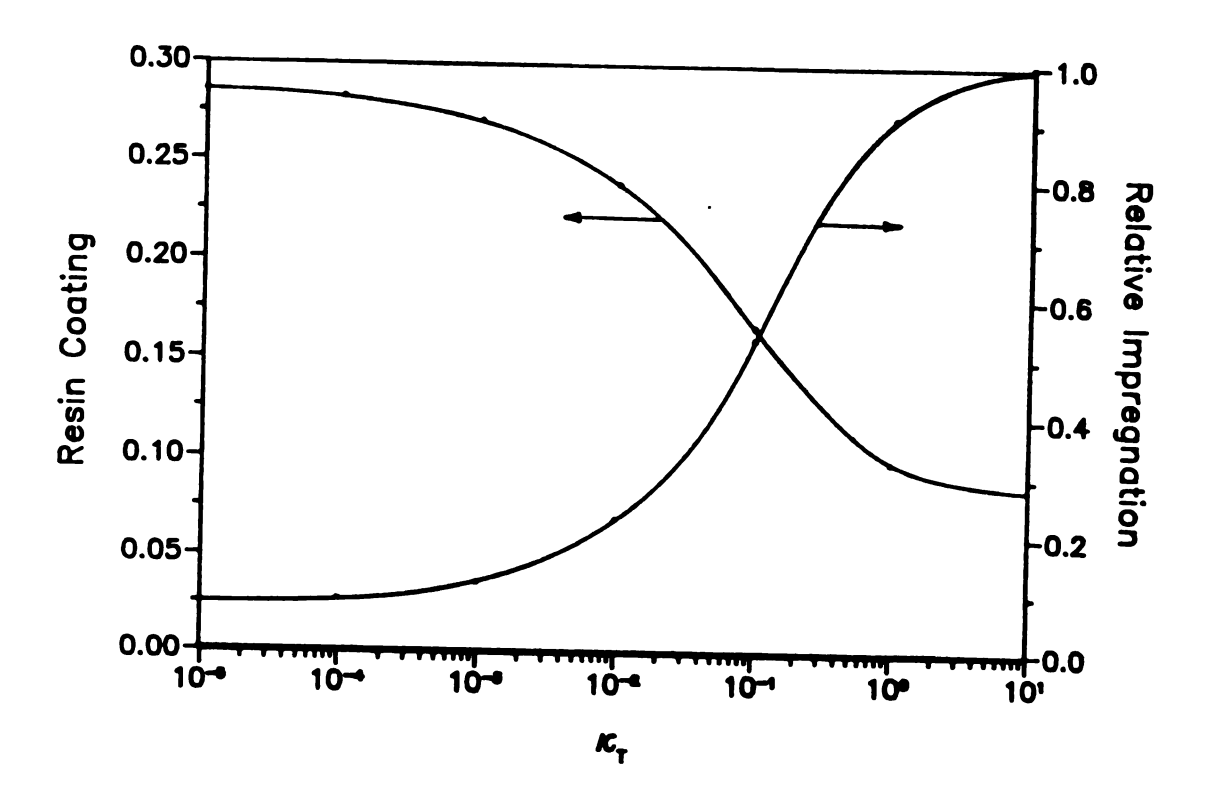


Figure 5.8 (a) Calculated resin distribution in a model fiber tow.

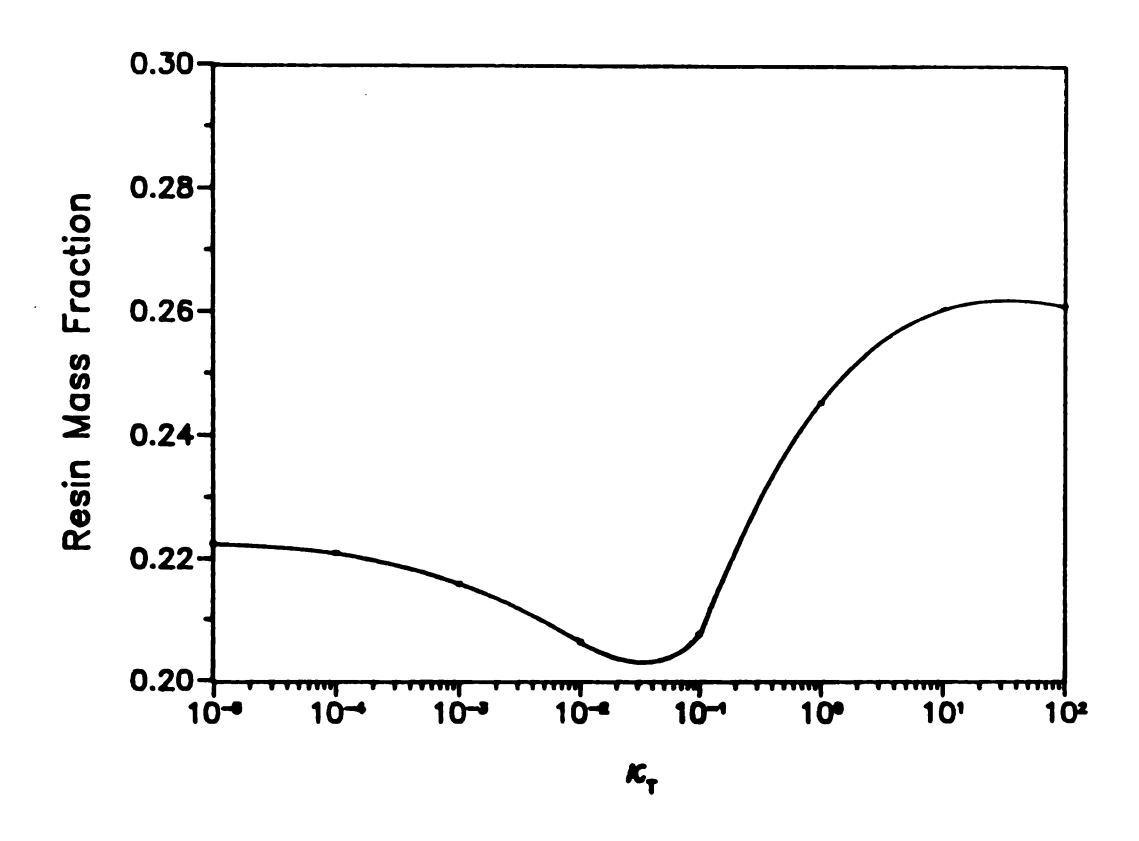


Figure 5.8 (b) Calculated resin mass fraction of a model fiber tow.

is a result of greater impregnation of the fiber tow. Again, this same effect is seen experimentally when the viscosity is increased (Figure 5.3).

The simplest model relating the effective fiber tow tensile modulus to the viscosity can be constructed by a mixing rule:

$$\kappa_r = V_f \cdot G_F + (1 - V_f) \cdot G_P$$
 (5.38)

where G_F and G_R are the partially wetted fiber tensile modulus and resin tensile modulus respectively. The resin modulus should be approximately proportional to the resin viscosity and, based on the experimental observations, the resin volume fraction will be an increasing function of the viscosity. The experimental results suggest that the effective tensile modulus of a partially wetted fiber tow varies with viscosity in the manner shown in Figure 5.9.

5.7 Conclusions

The effect of processing conditions on the resin mass fraction of prepreg tape produced by hot melt impregnation without the assistance of impregnation bars is studied. Experiments performed with polybutene and epoxy resin show, not only an increase in the prepreg resin content with increasing resin viscosity, but also greater penetration of resin into the fiber tow with larger processing viscosities. These observations cannot be explained by capillarity. A lubrication model of a wedge shaped impregnation die is

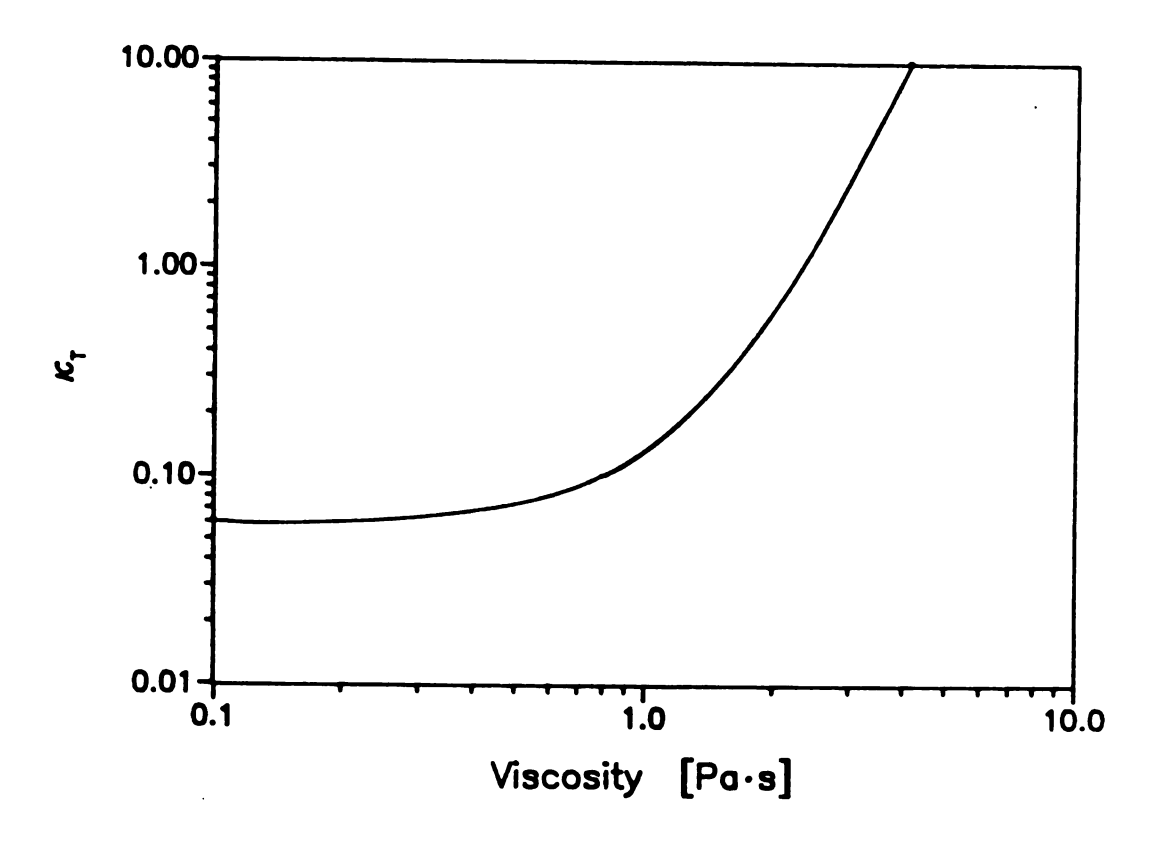


Figure 5.9 Relationship between the partially impregnated resin tow tensile modulus and the resin viscosity.

developed which incorporates fiber tow consolidation through a fiber tension mechanism. This model is able to predict the experimental observations with a tensile modulus that increases with resin viscosity, in a partially impregnated fiber tow.

Chapter 6

CONCLUSIONS AND RECOMMENDATIONS

6.1 Conclusions

The flow of viscous and viscoelastic liquids transverse to periodic arrays of circular cylinders is studied. Two array geometries, square and hexagonal, are examined; each having a void fraction of 70 percent. The elastic fluids include several non-shear thinning dilute polymer solutions composed of a wide range of molecular weight polyisobutylenes (0.9 to 6 million) dissolved at a concentration of 0.20 wt. % in a purely viscous polybutene solvent. These fluids are standard type *Boger* fluids. In addition, a shear thinning 2 wt. % polyisobutylene in decalin solution is studied.

At a void fraction of 70 percent Stokes flow simulations indicate little difference in the flow resistance between periodic square and hexagonal arrays. Using purely viscous liquids, these predictions are confirmed here for Reynolds numbers less than 0.30.

In this study particular attention is devoted to the influence macromolecular conformation on the enhanced pressure drop across the arrays. The Boger liquids used in this study are formulated to produce solutions with different levels of relative

	 		_

macromolecular extensibility. Being theta systems, the square of the degree of polymer extensibility associated with each of these solutions is proportional to their molecular weight. This is consistent with extensional viscosity measurements made by fiber spinning.

The initial departure from Darcy's law for the non-shear thinning solutions is due to enhancement in flow resistance and occurs at Deborah numbers of 0.80 and 0.35 for the square and hexagonal arrays respectively. These onset values are independent of molecular weight. Thus, the influence of molecular weight on the onset of elastic effects can only be accounted for through the solution's relaxation time. The differences in the onset Deborah numbers between the two array types are the result of different degrees of stretch rates occurring at a constant superficial velocity. By redefining the Deborah number in terms of the maximum array extension rate, as determined by the Stokes flow field, instead of the average strain rate, the onset Deborah number in both arrays collapse to approximately 1. This Deborah number corresponds to the coil-to-stretch transition, where a macromolecule under goes an abrupt transition from a coiled state to an elongated uncoiled state. This provides evidence that extensional flow effects determine the onset of elastic effects and dominate the flow processes at high Deborah numbers (De > 1).

At a constant Deborah number above the onset, the flow resistance is greater for higher molecular weights, and is consistently higher for the hexagonal array than the square array. At large values of Deborah number the relative flow resistances in both arrays become independent of Deborah number. The magnitude of these asymptotic

values are proportional to the molecular weight. Differences in the relative flow resistance at De > 1 when plotted versus the Deborah number indicate that the solution's relaxation time alone is not sufficient for parameterizing the enhanced pressure drop. The influence of the relative polymer extensibilities of each solution must also be taken into account. The asymptotic flow resistance - molecular weight relationship is consistent with the extensional viscosity measurements since the transverse cylinder array flows are dominated by extensional flow effects at high Deborah numbers. Thus, the experimental results follow the expected trend of the asymptotic flow resistance with molecular weight for theta systems.

Measurements of the extent of polymer degradation for non-shear thinning elastic fluids in rectangular and hexagonal arrays are also studied. The extent of degradation in both arrays is characterized by large reductions in the polymer relaxation time after the fluid passes several times through the arrays. At a comparable number of tests, the amount of degradation observed in the hexagonal array is much more severe than in the rectangular array. Further evidence that molecular extension in the hexagonal array is greater than that in the rectangular array is given by chain extension calculations based on the Stokes flow field.

The initial departure from Darcy's law for a shear thinning solution passing through a cylinder array is a reduction in the flow resistance. This is eventually followed by an enhancement as the Deborah number is increased, and occurs at Deborah numbers of 4.2 and 3.0 for the square and hexagonal array respectively. These data illustrate another important feature of fluid rheology on the transverse flow past cylinder arrays.

The flow dynamics are dominated by shear effects at low to moderate Deborah numbers which result in a reduced pressure drop across the array for shear thinning fluids. At high Deborah numbers the extensional effects become important, however.

The flow kinematics in both arrays is elucidated by laser Doppler velocimetry and streak photography. These techniques reveal a flow transition from steady to unsteady motion at Deborah numbers corresponding to the onset of enhanced pressure drop for the non-shear thinning elastic fluids. These results, along with the failure of current steady state flow calculations to predict the large experimentally measured flow resistances, imply that proper mathematical modeling of these type of flows must take into consideration the viscoelastic transition from steady to unsteady flow.

Finally the effect of shear viscosity on the permeation of a viscous liquid through a compliant array of cylinders is studied. This is accomplished by an experimental and theoretical investigation of the hot melt impregnation process. It has been found that by pulling a fiber tow through a viscous resin, and then through a wedge shaped die, the amount of material impregnating the tow is a function of the resin viscosity; the higher the resin viscosity, the better the penetration of resin into the fiber tow. A mathematical model, incorporating two fiber bundle consolidation mechanisms, results in good agreement with experiments with a viscosity dependent partially wetted tow modulus.

6.2 Recommendations

This study is a first step in understanding the flow of viscoelastic liquids flowing transverse to arrays of cylinders. Its motivation has been to identify and solve some of the problems associated with processing composite materials containing a viscoelastic component. Continuing on toward this goal, the next phase of this study should include conducting crossflow experiments with model arrays at smaller void fractions (most composite materials have void fractions of 30 to 40 percent rather than 70 percent). Next, the hot melt impregnation study of Chapter 5 presents interesting and counter-intuitive results in that higher resin viscosities lead to better impregnated fiber tows. This may be the result of tow consolidation effects caused by the tensile load placed on the fibers. An experimental study relating the fiber tension to prepreg quality is suggested. This should accompany consolidation experiments using model cylinder arrays and both viscous and viscoelastic liquids.

Finally, the unsteadiness of the viscoelastic flows has not sufficiently been explored. The implication that theoretical study of viscoelastic fluids flowing transverse to cylinder arrays must involve unsteady state calculations should make further study of the phenomena a high priority of non-Newtonian fluid machinists. The investigation of the unsteadiness should begin with the analysis of the fluctuating downstream pressure signals for high Deborah number flows. Next, the problems encountered with the LDV system (specifically the poor signal quality) must be resolved. Suggestions for modifying

the LDV set-up to obtain quantitative information about the flow unsteadiness include the following items. The use of new optics to reduce the size of the measuring volume. This would reduce the number of scattering particles in the measuring volume and reduce the fringe spacing, assisting in the measurement of low velocities. Furthermore, the cylinder arrays and windows should be made of optical glass to reduce unwanted light scattering. Also, the index of refraction should be matched between the test liquid and cylinder arrays in order to be able to map the velocity in the entire flow field without being hindered by reflections from curved surfaces. Lastly, a frequency analyzer is needed to obtain the power spectrum of the unsteady flows.

APPENDIX	

Appendix A

WEDGE DIE/FIBER IMPREGNATION FORTRAN PROGRAM

A.1 Flowchart

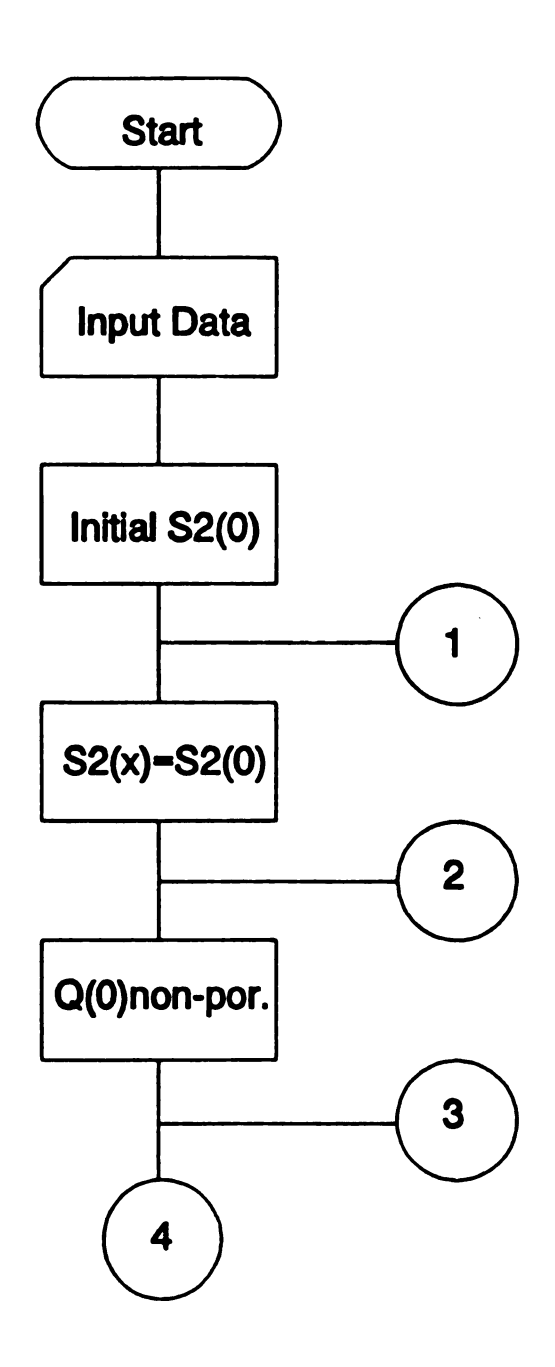


Figure A.1 Schematic of the computer algorithm.

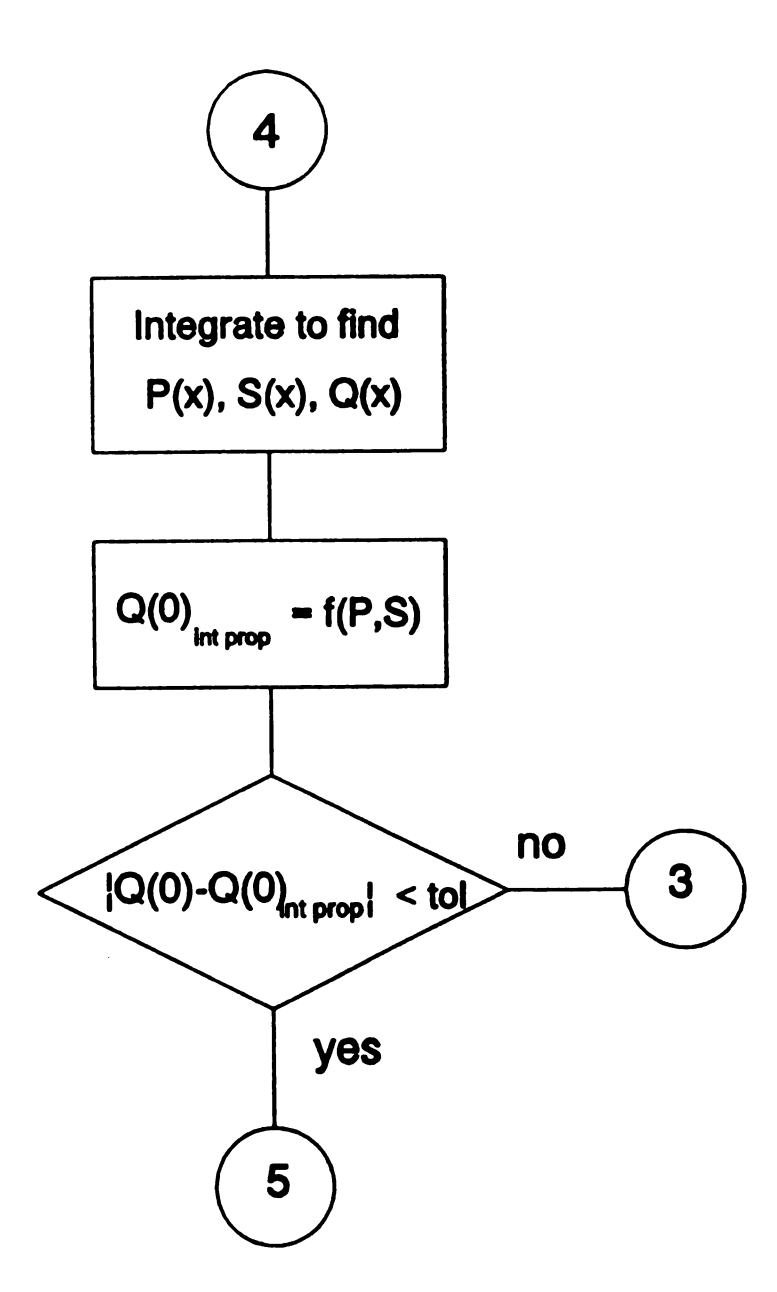


Figure A.1 Schematic of computer algorithm (continued).

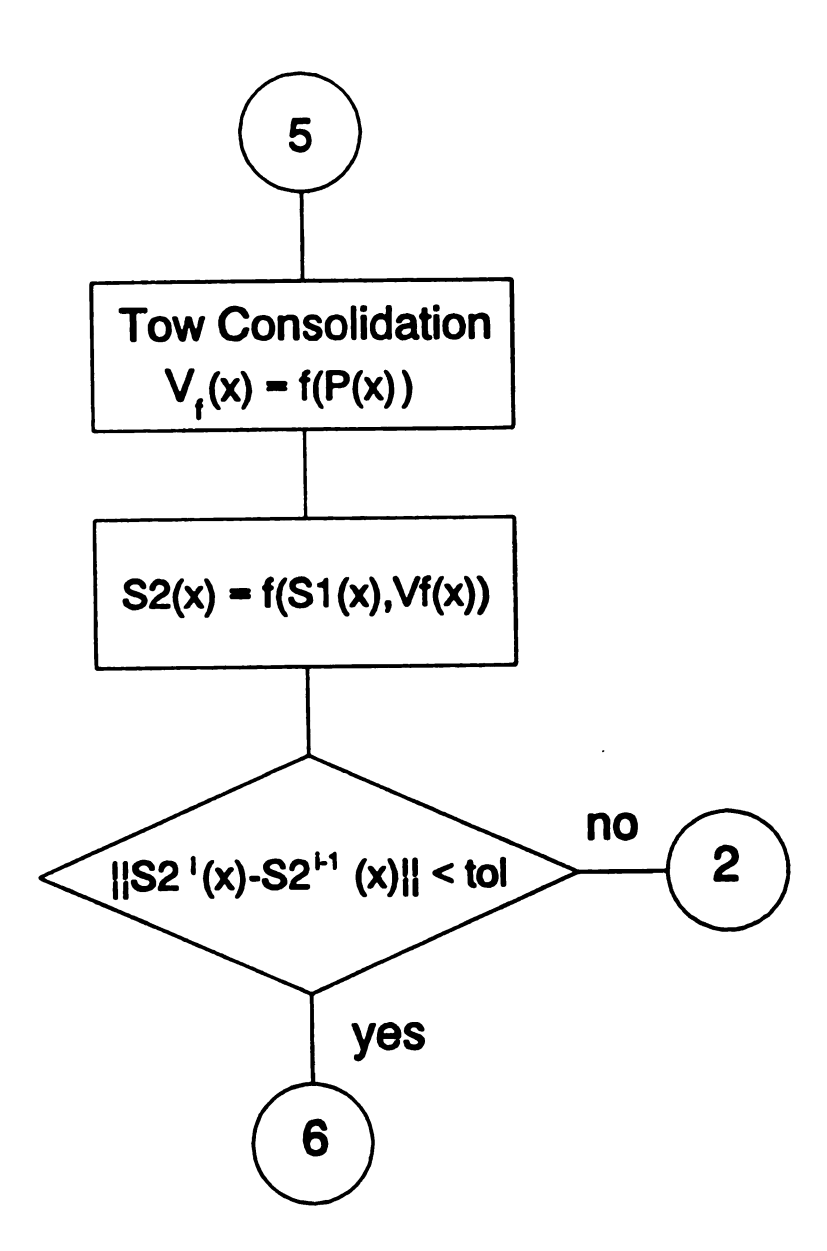


Figure A.1 Schematic of computer algorithm (continued).

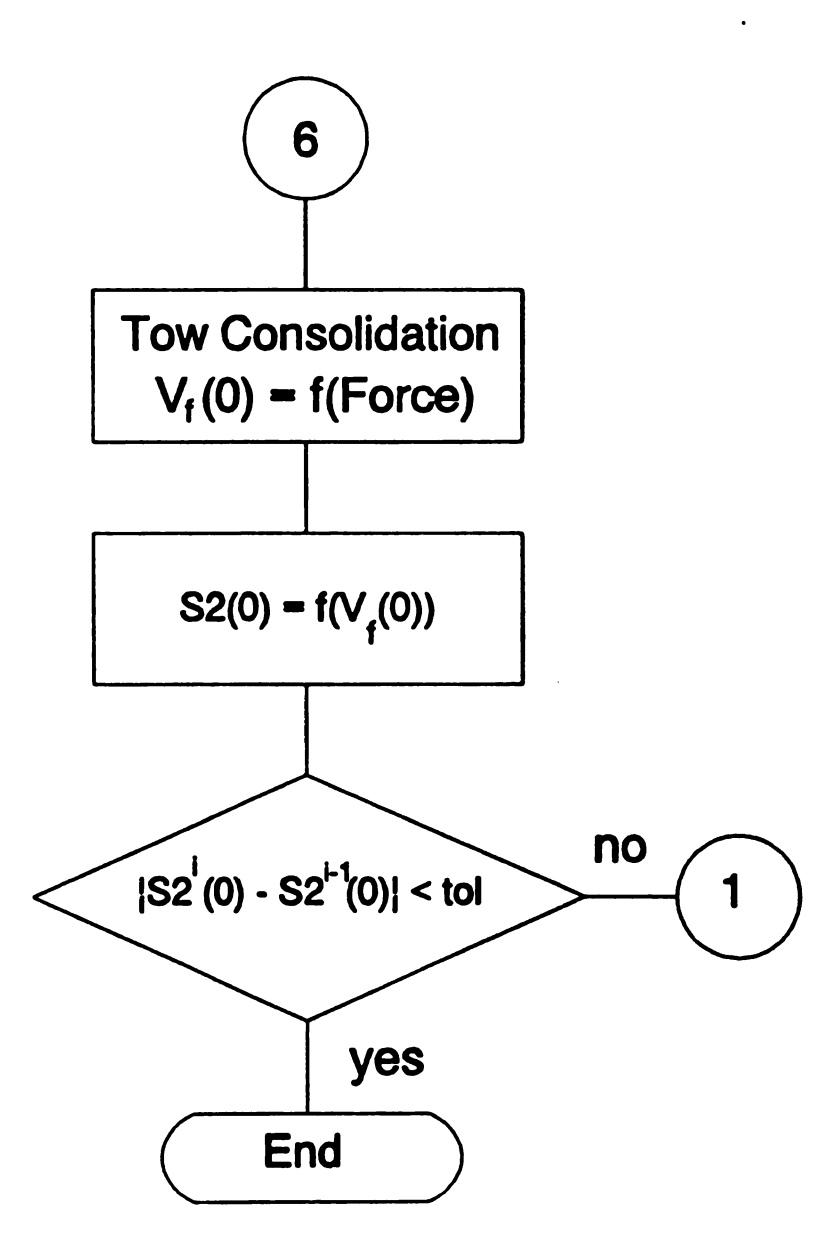


Figure A.1 Schematic of computer algorithm (continued).

A.2 Subprogram Summary

Routine	Function
1. PREPREG	Main Program
2. AJACOB	Calculate the Jacobian of the equation set
3. BETA	Miscellaneous functions
4. BJACOB	Modification of the Jacobian
5. CONSLP	Consolidation of fiber tow due to hydrodynamic pressure
6. CONSLT	Consolidation of fiber tow due to fiber tension
7. CSFIT	Cubic spline fit of tow profile and fiber volume fraction profile
8. DFDX	Derivative of equation set
9. DWALL	Slope of die wall
10. ERROR	Maximum difference between full and half steps during integration
11. FLOW1	Inlet flow bounds for initial guess of Q(0)
12. FLOW2	Integral property for the update of Q(0)
13. FORCE	Calculate force needed to pull tow

Function

Routine

14. FUNCT Equation set 15. KOZ Calculate the Kozeny constant 16. Kt Calculate the transverse permeability by the Blake-Kozeny-Carman equation 17. MATINV Invert 2 by 2 matrix 18. MATMULT 2 b y 2 matrix multiplication Semi-implicit Runga-Kutta 19. RUNGKUT integration 20. Fs2 Value of the fiber tow boundary position at location x 21. SEVAL Cubis spline intepolation 22. SIGMA Non-linear spring law describing tow during transverse consolidation 23. SIMPSON Integation by Simpson's rule 24. SPLINE Cubic spline fit 25. START Euler scheme to start integration 26. STEP Calculate next step size 27. FV Value of the fiber volume fraction at location x Calculate the location of 28. WALL the die wall

A.3 Program

```
C
        prepreg
        updated: 02 May 1991
C
C
        craig chmielewski
        summary: lubrication model of a Newtonian fluid impregnating
C
                 a continuous fiber tow as it is being pulled through
                 an exit die. Darcy's law models the impregnation and
C
C
                 the tow is modeled as a non-linear elastic network.
        implicit integer (i,j,n)
        implicit double precision (A-H, K-M, O-Z)
        parameter (inc=50001)
        dimension P(inc), Q(inc), S(inc), s2(inc), V(inc), x(inc)
        dimension err(2), y(2), y0(2), y1(2), y2(2)
        common c, DELTAP, GAMMA, kappaP, kappaT, Patm
        common Pin, Q0, rf, S0, s20, theta, V0, Va, Vt
        common/ERROR/ Etol
        common/CSPL/ xx(inc), S22(inc), VV(inc)
        common/CSPLs2/ Bs2(inc), Cs2(inc), Ds2(inc), ndats2
        common/CSPLV/ BV(inc), CV(inc), DV(inc), ndatV
        external CONSLP, CONSLT, CSFIT, ERROR, FLOW1, FLOW2
        external FORCE, Fs2, FV, RUNGKUT, START, STEP
        RADIAN(deg) = deg*pi/180.
C
        **** input dimensionless parameters ****
        open (unit=1,file='in.put',status='old')
           read(1,*) theta, c
           read(1,*) rf, Vt, Va
           read(1,*) kappaP, kappaT
           read(1,*) Ca, phi
           read(1,*) Pin, Pout, Patm, pct
           read(1,*) rhor, rhof
           read(1,*) Ctol, Etol, Qtol, Ttol
        close (unit=1)
        **** misc parameters ****
C
               = 4.*DATAN(1.D+000)
        pi
        theta = RADIAN(theta)
               = RADIAN(phi)
        phi
        GAMMA = 2.*pi*DCOS(phi)/(Ca*rf)
        DELTAP = Pout - Pin
        **** initial tow-die clearance: s20 = 2.*rf *****
C
        s20 = 1. - 2.*rf
        V0 = Vt/s20
```

```
iterT = 0
    5 iterT = iterT + 1
       write(*,999) iterT
        s10 = s20*(1. - pct/100.)
        S0 = DSQRT((s20-s10)*(1.-v0))
С
       ***** initial s2 and V *****
       inc0 = 10
        do 10, i=1, inc0 + 1
          x(i) = (i-1)/DFLOAT(inc0)
          s2(i) = s20
    10
           V(i) = V0
         n = inc0 + 1
         iterC = 0
    20
        call CSFIT(n,x,s2,V)
        iterC = iterC + 1
        write(*,1000) iterC
        ***** initial flow rate guess *****
 С
         call FLOW1 (Qlb, Qub)
         Q0 = Q1b
         iterQ - 1
        RES - 1.
        write(*,1010)
    30
        if (DABS(RES) .gt. Qtol) then
 С
         **** boundary conditions ****
           n
           x(n) = 0.D+000
           P(n)
                 - Pin
           S (n)
                 - S0
           Q(n)
                 = Q0
           s2(n) = s20
           V(n) = V0
           dx
               - 1./1000.
 C
        **** start integration ****
           do 35, i=2, 3
              x(i) = x(i-1)
              P(i) = P(i-1)
              S(i) = S(i-1)
              call START(dx,x(i),P(i),S(i),Q(i))
              s2(i) = Fs2(x(i))
    35
              V(i) = FV(x(i))
```

```
***** main *****
С
                 - 3
           x0
                 = x(n)
           y0(1) = P(n)
           y0(2) = S(n)
   40
           if (x0 .lt. 1.) then
        ***** init full step calc *****
C
              do 50, i=1, 2
   50
                 y(i) = y0(i)
              call RUNGKUT (x0, dx, y)
              do 60, i=1, 2
   60
                 y1(i) = y(i)
        **** half step calc ****
C
              qq = 1.
   70
               if (qq .ge. 1.) then
                  do 80, i=1, 2
                    y(i) = y0(i)
   80
                  x1 - x0
                  dx = 0.5*dx
                 do 100, i=1, 2
                     call RUNGKUT(x1, dx, y)
                     if (i .eq. 1) then
                        do 90, j=1, 2
   90
                           y^2(j) = y(j)
                     else
                     endif
  100
                     x1 = x1 + dx
                  if (y(1) .eq. 0.D+000 .or. y(2) .eq. 0.D+000) then
                     err(1) = 0.0D+000
                     err(2) = 0.0D+000
                            = 2.5D-001
                     PP
                  else
                     call ERROR(y1,y,err,qq)
                  endif
                  if (dx .1t. 1./FLOAT(inc-1)) qq = 2.5D-001
                 do 110, i=1, 2
  110
                     y1(i) = y2(i)
                  goto 70
              else
              endif
```

```
C
        **** reinitialize ****
              dx = 2.*dx
               x0 = x0 + dx
               do 120, i=1, 2
  120
                 y0(i) = y(i) + 1./7.*err(i)
               if (y0(1) .lt. 0.D+000) y0(1) = 0.D+000
        **** adjust step size ****
C
               call STEP (qq, dx)
C
        **** final step: adjust step to die exit ****
               if (x0+dx .gt. 1.) dx = 1.-x0
        **** full impregnation limitation ****
C
               if (DSQRT(S(n)) \cdot ge \cdot s2(n)*(1.-V(n))) then
                 y0(2) = (Fs2(x0)*(1.-FV(x0)))**2
               else
               endif
                     = n + 1
              n
              x(n)
                     = x0
              P(n)
                     - y0(1)
               S(n)
                     = y0(2)
              Q(n)
                    = Q0 + DSQRT(S0) - DSQRT(S(n))
               s2(n) = Fs2(x(n))
              V(n) = FV(x(n))
              goto 40
           else
              call FLOW2 (n, x, S, RES)
              write(*,1020) iterQ, Q0, RES
           endif
C
        ***** convergence (regula falsi) to proper Q0 *****
           if (iterQ .eq. 1) then
              A - Q0
              FA - RES
              Q0 - Qub
           elseif (iterQ .eq. 2) then
              B = Q0
              FB - RES
              Q0 = (A*FB - B*FA)/(FB - FA)
           elseif (FA*RES .lt. 0.) then
              B = Q0
              FB - RES
              Q0 = (A*FB - B*FA)/(FB - FA)
```

```
else
              A - Q0
              FA - RES
              Q0 = (A*FB - B*FA)/(FB - FA)
           endif
           iterQ = iterQ + 1
           goto 30
        else
        endif
        **** tow consolidation by pressure ****
C
        do 130, i=2, n
           if (P(i) .gt. P(i-1)) then
              Xmax = x(1)
              Pmax = P(i)
              call CONSLP (P(i), S(i), s2(i), V(i))
              s2(i) = s2(i-1)
              V(i) = V(i-1)
           endif
  130
        continue
        if (iterC .lt. 10) then
           do 140, i=2, n
              conerr = DABS((Fs2(x(i))-s2(i))/s2(i))
              if (conerr .gt. Ctol) goto 20
  140
           continue
        else
        endif
        **** calc force ****
C
        print*, ' '
        print*, 's20= ', s20
       print*, 'V0 = ', V0
print*, '
        call FORCE (n,x,P,S,forc,load)
C
        ***** tow consolidation by tension ****
        s200 = s20
        call CONSLT(forc)
        print*, 's20=', s20
        print*, 'V0 = ', V0
        print*, ' '
        if (DABS(s200-s20)/s20 .ge. Ttol) goto 5
        **** calc coating thickness ****
C
        coat = Q(n)
```

```
**** calc fiber vol fract ****
C
       Vf = s20*V0/(s2(n) + coat)
        **** calc fiber mass fract ****
С
        denratio = rhor/rhof
       Mf = s20*V0/(s20*V0 + (DSQRT(S(n)) + coat)*denratio)
        **************
C
        open (unit=1, file='out.dat', status='new')
        open (unit=2, file='P.dat', status='new')
        open(unit=3,file='Q.dat',status='new')
        open (unit=4, file='impreg.dat', status='new')
        open (unit=5, file='s2.dat', status='new')
        open (unit=6, file='V.dat', status='new')
          write(1,1030) 'theta (deg)
                                                  ', theta*180./pi
          write(1,1030) 'L/(1/2*W2)
                                                  ', c
                                                  ', rf
          write(1,1030) 'rf/(1/2*W2)
          write(1,1030) 'Vf init
                                                   , Vt
          write(1,1030) 'kappaP*(1/2*W2)/(eta*U0)', kappaP
          write(1,1030) 'kappaT*(1/2*W2)/(eta*U0)', kappaT
          write(1,1030) 'Ca = (eta*U0)/gamma
          write(1,1030) 'Contact ang. (deg)
                                                 ', phi*180./pi
          write(1,1040)
           jaize - 50
           istep = 1
           if (n/jsize .ne. 0) jstep = n/jsize
           do 150, i=1, n, jstep
             pctimpg = DSQRT(S(i))/(s2(i)*(1.-V(i)))
              write (1,1050) i, x(i), P(i), Q(i), pctimpg, s2(i), V(i)
             write(2,1090) x(i), P(i)
             write(3,1090) x(i), Q(i)
             write(4,1090) x(i), pctimpg
             write(5,1090) x(i), s2(i)
  150
             write(6,1090) x(i), V(i)
           if (i-jstep .ne. n) then
             pctimpg = DSQRT(S(n))/(s2(n)*(1.-V(n)))
             write (1,1050) n, x(n), P(n), Q(n), pctimpg, s2(n), V(n)
             write(2,1090) x(n), P(n)
             write(3,1090) x(n), Q(n)
             write(4,1090) x(n), pctimpg
             write(5,1090) x(n), s2(n)
             write(6,1090) x(n), V(n)
           else
           endif
```

```
write(1,1060) 'Pin
                                               ', Pin
           write(1,1070) 'Pmax
                                               ', Pmax
           write(1,1070) 'Xmax
                                               ', Xmax
           write(1,1080) 'Q (x = 0)
                                               ', Q0
                                               ', Q1b
           write(1,1070) 'Q Lower Bound
                                               ', Qub
           write(1,1070) 'Q Upper Bound
           write(1,1080) 'Force
                                               ', forc
           write(1,1070) 'Load
                                                , load
                                               ', coat
           write(1,1080) 'Coat Thickness
           write(1,1080) 'Fiber Vol Fract
                                               ', Vf
                                               ', Mf
           write(1,1070) 'Fiber Mass Fract
           write(1,1070) 'Resin Mass Fract ', 1.0D+000 - Mf
        close (unit=1)
        close (unit=2)
        close (unit=3)
        close (unit=4)
        close (unit=5)
        close (unit-6)
  999
        format(/lx,'Tension Consolidation Iter.:',16)
1000
        format (/3x, 'Pressure Consolidation Iter.:', 16)
        format (/T6, 'iterQ', T18, 'Q(0)', T31, 'F(Q(0))'/)
1010
1020
        format (1x, 18, 2D15.5)
1030
        format (T15, A24, T40, '=', T45, E11.4)
1040
        format(/T4,'Pt',T13,'x',T24,'P',T35,'Q',T43,'% IMPG',
               T56,'s2',T68,'V'/)
 1050
        format (1x, I5, T10, F6.4, 5F11.4)
1060
        format (///T20, A19, T40, '=', T45, F9.4)
1070
        format (T20, A19, T40, '=', T45, F9.4)
1080
        format (/T20, A19, T40, '=', T45, F9.4)
1090
        format (2F10.5)
        end
        **** sub: jacobian ****
C
        subroutine AJACOB(x,y,AJ)
        implicit double precision (A-Z)
        dimension AJ(2,2), y(2)
        common c, DELTAP, GAMMA, kappaP, kappaT, Patm
        common Pin, Q0, rf, S0, s20, theta, V0, Va, Vt
        external BETA, FV, Kt
        V = FV(x)
        call BETA(x,B1,B2,B3)
        AJ(1,1) = 0.D+000
        AJ(1,2) = -c*B3/DSQRT(y(2))
        AJ(2,1) = 2.*c*Kt(V)*(1.-V)
        AJ(2,2) = 0.D+000
        return
        end
```

```
**** sub: misc functs ****
С
        subroutine BETA(x, BETA1, BETA2, BETA3)
        implicit double precision (A-Z)
        external Fs2, WALL
        s2 = Fs2(x)
        H = WALL(x) + 1.D+000
        BETA1 = 1./3.*H**3 - s2**2*H + 2./3.*s2**3
        BETA2 = 1./2.*(H - s2)**2
        BETA3 = -6./(H-s2)**3
        return
        end
        **** sub: modified jacobian ****
C
        subroutine BJACOB(AJ, dx, BJ)
        implicit double precision (A-Z)
        dimension AJ(2,2), BJ(2,2)
        a = 4.35866524D-001
        BJ(1,1) = 1.D+000
        BJ(1,2) = -1.*dx*a*AJ(1,2)
        BJ(2,1) = -1.*dx*a*AJ(2,1)
        BJ(2,2) = 1.D+000
        return
        end
        **** sub: regula falsi - pressure consolidation ****
C
        subroutine CONSLP (P,S,s2,V)
        implicit double precision (A-Z)
        common c, DELTAP, GAMMA, kappaP, kappaT, Patm
        common Pin, Q0, rf, S0, s20, theta, V0, Va, Vt
        RES(Vf) = (DSQRT(Va/Vf) - 1.)**4 - kappaP/P*(DSQRT(Vf/V0) - 1.)
        s1 = s2 - DSQRT(S)/(1. - V)
C
        **** note: tol <= (DSQRT(Va/V) - 1.) **4 *****
        tol = 1.D-010
        aa - V0
        bb - Va
        cc = V0
```

```
10
        if (DABS(RES(cc)) .ge. tol) then
           cc = (aa*RES (bb) -bb*RES (aa)) / (RES (bb) -RES (aa))
           if (RES(aa)*RES(cc) .lt. 0.D+000) then
              bb = cc
           else
               aa = cc
           endif
           goto 10
        else
        endif
        V - cc
        s2 = s1 + V0/V*(s20 - s1)
        return
        end
        **** sub: regula falsi - tension consolidation ****
C
        subroutine CONSLT(forc)
        implicit double precision (A-Z)
        common c, DELTAP, GAMMA, kappaP, kappaT, Patm
        common Pin, Q0, rf, S0, s20, theta, V0, Va, Vt
        RES (Vf) = (1./Vf - 1./Va)**2 - kappaT/forc*(1./Vt - 1./Vf)
        ***** note: tol <= (1./V - 1./Va)**2 *****
C
        tol = 1.D-010
        aa - Vt
        bb = Va
        cc - Vt
   10
        if (DABS(RES(cc)) .ge. tol) then
           cc = (aa*RES (bb) -bb*RES (aa)) / (RES (bb) -RES (aa))
           if (RES(aa)*RES(cc) .1t. 0.D+000) then
              bb = cc
           else
              aa = cc
           endif
           goto 10
        else
        endif
        V0 - cc
        s20 = Vt/V0
        return
        end
```

```
C
          ***** sub: cubic spline fit of s2 and V *****
          subroutine CSFIT(n,x,s2,V)
          implicit integer (i,n)
          implicit double precision (A-H, J-M, O-Z)
          parameter (inc=50001)
         dimension s2(inc), V(inc), x(inc)
         common/CSPL/ xx(inc), S22(inc), VV(inc)
         common/CSPLs2/ Bs2(inc), Cs2(inc), Ds2(inc), ndats2
         common/CSPLV/ BV(inc), CV(inc), DV(inc), ndatV
         external SPLINE
         do 10, i=1, n
            xx(i) = x(i)
            s22(i) = s2(i)
    10
            VV(i) = V(i)
         ndats2 = n
         ndatV = n
         call SPLINE(ndats2,xx,s22,Bs2,Cs2,Ds2)
         call SPLINE(ndatV, xx, VV, BV, CV, DV)
         return
         end
C
        **** sub: dfi/dx ****
        subroutine DFDX(dx,x,f,y,df)
        implicit double precision (A-Z)
        dimension df(2), f(2), y(2)
        common c, DELTAP, GAMMA, kappaP, kappaT, Patm
        common Pin, Q0, rf, S0, s20, theta, V0, Va, Vt
        external BETA, DWALL, Fs2, FV, Kt, WALL
        V = FV(x)
       s2 = Fs2(x)
       H = WALL(x) + 1.
       call BETA(x,B1,B2,B3)
        **** approx derivatives: ds2/dx, dV/dx, dB3/dx, dKt/dx *****
       s22 = Fs2(x+dx)
       V2 = FV(x+dx)
       ds2 = (s22-s2)/dx
       dV = (V2-V)/dx
       dKt = (Kt(V2)-Kt(V))/dx
       dB3 = B2*B3**2*(DWALL(x) - ds2)
       term1 = f(1)/B3*dB3
       term2 = -c*B3*(f(2)/DSQRT(y(2)) + DWALL(x) - ds2)
```

C

```
df(1) = term1 + term2
        terml = 2.*c*Kt(V)*(1.-V)*f(1)
        term2 = -2.*c*Kt(V)*(y(1)-(Patm-GAMMA))*dV
        term3 = 2.*c*(1.-V)*(y(1)-(Patm-GAMMA))*dKt
        df(2) = term1 + term2 + term3
        return
        end
        **** fcn: derivative of wall boundary ****
С
C
                             WEDGE
        double precision function DWALL(x)
        implicit double precision (A-Z)
        common c, DELTAP, GAMMA, kappaP, kappaT, Patm
        common Pin, Q0, rf, S0, s20, theta, V0, Va, Vt
        DWALL = -c*DTAN(theta)
        return
        end
        **** sub: max diff between full and half steps ***
C
        subroutine ERROR (y1, y2, err, q)
        implicit integer (i)
        implicit double precision (A-H, J-Z)
        dimension err(2), tol(2), y1(2), y2(2)
        common/ERROR/ Etol
        do 10, i=1, 2
   10
           tol(i) = y2(i)
        do 20, i=1, 2
           err(i) = y2(i) - y1(i)
   20
        q = DMAX1 (DABS (err(1)/tol(1)), DABS (err(2)/tol(2)))
        q = q/Etol
        return
        end
        **** sub: flow1 (inlet flow bounds) *****
C
        subroutine FLOW1 (Qlb, Qub)
        implicit integer (i)
        implicit double precision (A-H, J-Z)
        parameter (inc=10000)
        dimension F1(inc+1), F2(inc+1), F3(inc+1)
        common c, DELTAP, GAMMA, kappaP, kappaT, Patm
        common Pin, Q0, rf, S0, s20, theta, V0, Va, Vt
        external BETA, Fs2, FV, SIMPSON
```

```
do 10, i=1, inc+1
           x = (i-1)/DFLOAT(inc)
           s2 - Fs2(x)
          V = FV(x)
           call BETA(x,B1,B2,B3)
           F1(i) = B3
           F2(i) = 1./B2
                 = (s2*(1.-V))**2
   10
           F3(i) = B3*(DSQRT(S) - DSQRT(S0))
        call SIMPSON(inc,F1,F1int)
        call SIMPSON(inc,F2,F2int)
        call SIMPSON(inc,F3,F3int)
        Qlb = 1./Flint*(0.5*DELTAP/c - 3./2.*F2int)
        Qub = 1./Flint*(0.5*DELTAP/c - 3./2.*F2int + F3int)
        return
        end
C
        **** sub: integral property to find Q0 ****
        subroutine FLOW2 (n,x,S,RES)
        implicit integer (i,n)
        implicit double precision (A-H, J-M, O-Z)
        parameter (inc=10000, ispl=50001)
        dimension F1 (inc+1), F2 (inc+1), F3 (inc+1)
        dimension S(ispl), x(ispl)
        dimension BS(ispl), CS(ispl), DS(ispl)
        common c, DELTAP, GAMMA, kappaP, kappaT, Patm
        common Pin, Q0, rf, S0, s20, theta, V0, Va, Vt
        external BETA, Fs2, FV, SPLINE, SEVAL, SIMPSON
        call SPLINE (n, x, S, BS, CS, DS)
        do 10, i=1, inc+1
           x1 = (i-1)/DFLOAT(inc)
           SS = SEVAL(n,x1,x,S,BS,CS,DS)
           s2 = Fs2(x1)
           V = FV(x1)
           call BETA(x1,B1,B2,B3)
           F1(i) = B3
           F2(i) = 1./B2
   10
           F3(i) = B3*(DSQRT(SS) - DSQRT(SO))
        call SIMPSON (inc, F1, F1int)
        call SIMPSON(inc,F2,F2int)
        call SIMPSON(inc,F3,F3int)
        RES = Q0 - 1./Flint*(0.5*DELTAP/c - 3./2.*F2int + F3int)
        return
        end
```

```
C
        **** sub: calc tow force and die load ****
        subroutine FORCE(n,x,P,S,forc,load)
        implicit integer (i,n)
        implicit double precision (A-H, J-M, O-Z)
        parameter (inc=10000, ispl=50001)
        dimension dP(ispl), PP(ispl), F1(inc+1), F2(inc+1)
        dimension P(ispl), S(ispl), x(ispl), F(2), y(2)
        dimension BdP(ispl), CdP(ispl), DdP(ispl)
        dimension BPP(ispl), CPP(ispl), DPP(ispl)
        common c, DELTAP, GAMMA, kappaP, kappaT, Patm
        common Pin, Q0, rf, S0, s20, theta, V0, Va, Vt
        external BETA, Fs2, SPLINE, SEVAL, SIMPSON, WALL
        do 10, i=1, n
           y(1) = P(i)
           y(2) = S(1)
           call FUNCT(x(i),y,f)
   10
           dP(i) = f(1)
        call SPLINE(n, x, dP, BdP, CdP, DdP)
        call SPLINE(n,x,P,BPP,CPP,DPP)
        do 20, i=1, inc+1
                 = (i-1)/DFLOAT(inc)
           x1
           dPdx = SEVAL(n,x1,x,dP,BdP,CdP,DdP)
           PP(i) = SEVAL(n, x1, x, P, BPP, CPP, DPP)
                 = Fs2(x1)
           s2
           H
                 = WALL(x1) + 1.
           F1(i) = 1./(H - s2)
           call BETA(x1,B1,B2,B3)
   20
           F2(i) = 1./c*dPdx*B2*F1(i)
        call SIMPSON(inc,F1,Flint)
        call SIMPSON(inc, F2, F2int)
        call SIMPSON(inc, PP, load)
        forc = Flint + F2int
        load = load
        return
        end
        **** sub: eqn set ****
C
        subroutine FUNCT(x,y,f)
        implicit double precision (A-Z)
        dimension f(2), y(2)
        common c, DELTAP, GAMMA, kappaP, kappaT, Patm
        common Pin, Q0, rf, S0, s20, theta, V0, Va, Vt
        external BETA, Fs2, FV, Kt, WALL
        s2
             = Fs2(x)
        V
             = FV(x)
             = WALL(x) + 1.
        H
        call BETA(x,B1,B2,B3)
```

```
Q = Q0 + DSQRT(S0) - DSQRT(y(2))
        f(1) = c*B3*(2.*Q - (H-s2))
        f(2) = 2.*c*Kt(V)*(1.-V)*(y(1) - (Patm - GAMMA))
        return
        end
        **** fcn: Kozeny constant ****
C
        double precision function KOZ(V)
        implicit double precision (A-Z)
        B1 = 1.068136D-008
        B2 = 2.501025D+001
        B3 - 7.743506D+000
        KOZ = B1*DEXP(B2*V) + B3
        return
        end
       ***** fcn: permeability *****
С
       double precision function Kt(V)
        implicit double precision (A-Z)
        common c, DELTAP, GAMMA, kappaP, kappaT, Patm
        common Pin, Q0, rf, S0, s20, theta, V0, Va, Vt
        external KOZ
        Kt = (1. - V)**3/V**2*1./(4.*KOZ(V))*rf**2
        return
        end
       **** sub: inverse of dim 2 matrix ****
C
       subroutine MATINV(A, AINV)
        implicit double precision (A-Z)
        dimension A(2,2), AINV(2,2)
        detA = A(1,1)*A(2,2) - A(1,2)*A(2,1)
        detinv = 1./detA
        Ainv(1,1) = detinv*A(2,2)
        Ainv(1,2) = -detinv*A(1,2)
        Ainv(2,1) = -detinv*A(2,1)
        Ainv(2,2) = detinv*A(1,1)
        return
        end
```

```
**** sub: matrix mult ****
C
        subroutine MATMULT(N, A, x, y)
        implicit integer (i, j, N)
        implicit double precision (A-H, K-M, O-Z)
        dimension A(N,N), x(N), y(N)
        do 20, i=1, N
           y(i) = 0.D+000
           do 10, j=1, N
              y(i) = A(i,j)*x(j) + y(i)
   10
           continue
   20
        continue
        return
        end
        **** sub: 3rd order semi-implicit Runga-Kutta ****
C
        subroutine RUNGKUT(x,dx,y)
        implicit integer (i)
        implicit double precision (A-H, J-Z)
        dimension AJ(2,2), BJ(2,2), BJINV(2,2)
        dimension df(2), f(2), k1(2), k2(2), k3(2), y(2), y1(2)
        common c, DELTAP, GAMMA, kappaP, kappaT, Patm
        common Pin, Q0, rf, S0, s20, theta, V0, Va, Vt
        external AJACOB, BJACOB, DFDX, FUNCT, MATINV, MATMULT
            - 4.358665240D-001
        b2 = 7.500000000D-001
        b31 = -6.302020900D-001
        b32 = -2.423378910D-001
        R1 = 1.037609497D+000
        R2 - 8.349304840D-001
        call AJACOB(x,y,AJ)
        call BJACOB (AJ, dx, BJ)
        call MATINV(BJ, BJINV)
        call FUNCT(x,y,f)
        call DFDX(dx,x,f,y,df)
        do 10, i=1, 2
   10
           f(i) = f(i) + dx*a*df(i)
        CALL MATMULT (2, BJINV, f, k1)
        x1 = x + b2*dx
        do 20, i=1, 2
           y1(i) = y(i) + b2*k1(i)*dx
           if (y1(i) .1t. 0.D+000) y1(i) = 0.D+000
   20
        continue
        call FUNCT(x1,y1,f)
```

```
do 30, i=1, 2
           f(i) = f(i) + dx*a*df(i)
   30
        CALL MATMULT (2, BJINV, f, k2)
        do 40, i=1, 2
           term1 = k1(i)*dx + a*df(i)*dx**2
           term2 = k2(i)*dx + a*df(i)*dx**2
   40
           f(i) = b31*term1 + b32*term2
        CALL MATMULT (2, BJINV, f, k3)
        do 50, i=1, 2
   50
           y(i) = y(i) + R1*k1(i)*dx + R2*k2(i)*dx + k3(i)
        if (y(1) .1t. 0.D+000) y(1) = 0.D+000
        return
        end
        ***** fcn: determine S2 at x *****
C
        double precision function Fs2(x)
        implicit integer (i,j,n)
        implicit double precision (A-H, K-M, O-Z)
        parameter (inc=50001)
        common/CSPL/ xx(inc), s22(inc), VV(inc)
        common/CSPLs2/ Bs2(inc), Cs2(inc), Ds2(inc), ndats2
        external SEVAL
        Fs2 = SEVAL(ndats2,x,xx,s22,Bs2,Cs2,Ds2)
        return
        end
        seval
                G. Forsythe, M. Malcolm, and C. Moler
        from:
                Computer Methods for Mathematical Computations
                Prentice-Hall, 1977.
        **** cubic spline interpolation - function ****
        double precision function SEVAL(N,u,x,y,B,C,D)
        implicit integer (i-k,N)
        implicit double precision (A-H, L-M, O-Z)
        dimension x(N), y(N), B(N), C(N), D(N)
        DATA 1/1/
        if (i .ge. n) i = 1
           if (u .lt. x(i)) goto 10
              if (u .le. x(i+1)) goto 30
   10
           i - 1
           j - N+1
   20
        k = (1+j)/2
```

C

C

C

C

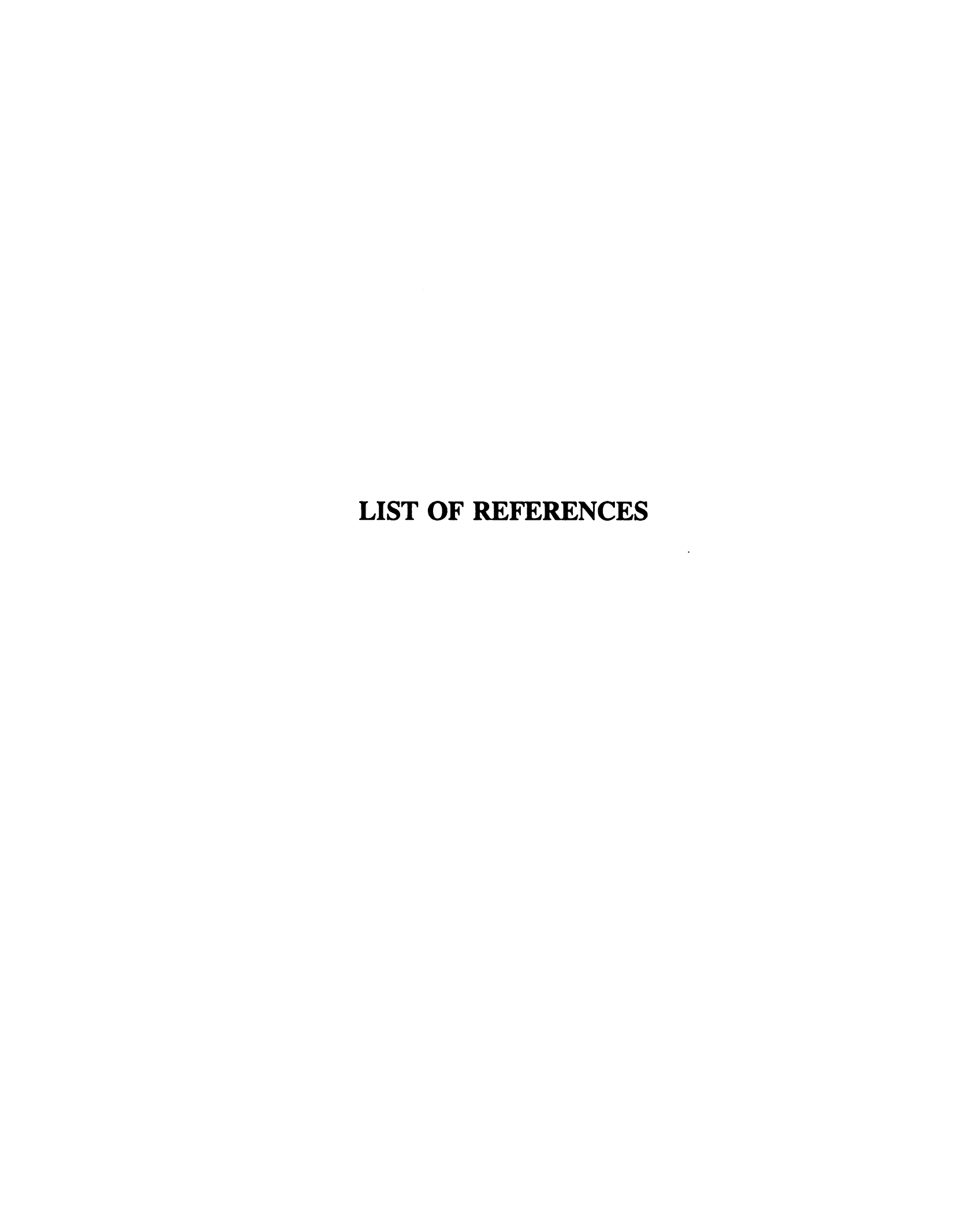
```
if (u . lt. x(k)) j = k
           if (u . ge. x(k)) i = k
              if (j .gt. i+1) goto 20
        dx = u - x(i)
   30
        SEVAL = y(i) + DX*(B(i) + DX*(C(i) + DX*D(i)))
        return
        end
        **** fcn: non-linear spring ****
C
        double precision function sigma(V)
        implicit double precision (A-Z)
        common c, DELTAP, GAMMA, kappaP, kappaT, Patm
        common Pin, Q0, rf, S0, s20, theta, V0, Va, Vt
        sigma = kappaP*(DSQRT(V/V0) - 1.)/(DSQRT(Va/V) - 1.)**4
        return
        end
C
        **** sub: integration - Simpson's rule ****
         subroutine SIMPSON(inc,f,simp)
         implicit integer (i)
         implicit double precision (A-H, J-Z)
         dimension f(inc+1)
              - 1./inc
         dx
         simp0 = f(1) + f(inc+1)
         simp1 = 0.D+000
         simp2 = 0.D+000
         do 10, i=2, inc, 2
   10
            simpl = simpl + f(i)
         do 20, i=3, inc-1, 2
   20
            simp2 = simp2 + f(i)
         simp = dx/3.*(simp0 + 4.*simp1 + 2.*simp2)
         return
         end
        spline
C
                G. Forsythe, M. Malcolm, and C. Moler
C
        from:
                Computer Methods for Mathematical Computations
C
C
                Prentice-Hall, 1977.
        ***** cubic spline interpolation *****
C
```

```
subroutine SPLINE(N,x,y,B,C,D)
      implicit integer (i,N)
      implicit double precision (A-H, J-M, O-Z)
      dimension x(N), y(N), B(N), C(N), D(N)
      NM1 = N-1
      if (N .lt. 2) return
      if (N .1t. 3) goto 50
        D(1) = x(2) - x(1)
         C(2) = (y(2)-y(1))/D(1)
         do 10, i=2, NM1
            D(i) = x(i+1) - x(i)
                 = 2.*(D(i-1) + D(i))
            B(1)
            C(i+1) = (y(i+1) - y(i))/D(i)
                 = C(i+1) - C(i)
10
            C(i)
         B(1) = -D(1)
         B(N) = -D(N-1)
         C(1) = 0.
         C(N) = 0.
         if (N .eq. 3) goto 15
            C(1) = C(3)/(x(4)-x(2)) - C(2)/(x(3)-x(1))
            C(N) = C(N-1)/(x(N)-x(N-2)) - C(N-2)/(x(N-1)-x(N-3))
            C(1) = C(1)*D(1)**2/(x(4)-x(1))
            C(N) = -C(N)*D(N-1)**2/(x(N)-x(N-3))
 15
         do 20, i=2, N
            T = D(i-1)/B(i-1)
            B(i) = B(i) - T*D(i-1)
 20
            C(i) = C(i) - T*C(i-1)
         C(N) = C(N)/B(N)
         do 30, ib = 1, NM1
            i = N - ib
 30
            C(i) = (C(i) - D(i)*C(i+1))/B(i)
         B(N) = (y(N)-y(NM1))/D(NM1) + D(NM1)*(C(NM1) + 2.*C(N))
         do 40, i=1, NM1
            B(i) = (y(i+1) - y(i))/D(i) - D(i)*(C(i+1) + 2.*C(i))
            D(i) = (C(i+1) - C(i))/D(i)
 40
            C(i) = 3.*C(i)
         C(N) = 3.*C(N)
         D(N) = D(N-1)
         return
      B(1) = (y(2) - y(1))/(x(2) - x(1))
 50
      C(1) = 0.
      D(1) = 0.
      B(2) = B(1)
      C(2) = 0.
      D(2) = 0.
      return
      end
```

```
**** sub: start integration (Euler method) *****
 c
         subroutine START (dx,x,P,S,Q)
         implicit double precision (A-Z)
         dimension f(2), y(2)
         common c, DELTAP, GAMMA, kappaP, kappaT, Patm
         common Pin, Q0, rf, S0, s20, theta, V0, Va, Vt
         external FUNCT
         y(1) = P
         y(2) - s
         call FUNCT(x,y,f)
         x = x + dx
         P = P + dx*f(1)
         S = S + dx * f(2)
         Q = Q0 + DSQRT(S0) - DSQRT(S)
         return
         end
         **** sub: step size adjustment ****
C
        subroutine STEP (q, dx)
        implicit integer (i)
        implicit double precision (A-H, J-Z)
        dx = dx*DMIN1((4.*q)**(-.25),3.D+000)
        return
        end
 C
         **** fcn: determine V at x ****
         double precision function FV(x)
         implicit integer (i,j,n)
         implicit double precision (A-H,K-M,O-Z)
         parameter (inc=50001)
         common/CSPL/ xx(inc), s22(inc), VV(inc)
         common/CSPLV/ BV(inc), CV(inc), DV(inc), ndatV
         external SEVAL
         FV = SEVAL (ndatV, x, xx, VV, BV, CV, DV)
         return
         end
```

A.4 Example input data file

```
2.000000D+000, 6.926950D+001
4.899200D-002, 6.428700D-001, 9.070000D-001
6.676200D-001, 1.000000D-003
4.145100D-001, 3.000000D+001
0.00000D+000, 0.00000D+000, 0.00000D+000, 0.00000D+000
1.137000D+000, 1.800000D+000
1.000000D-004, 1.00000D-005, 1.00000D-010, 1.00000D-003
theta
          , C
          , Vt
rf
                        , Va
          , kappaT
kappaP
           , phi
           , Pout
                        , Patm
Pin
                                       , pct
           , rhof
rhor
Ctol
          , Etol
                                       , Ttol
                        , Qtol,
```



LIST OF REFERENCES

- Adams, K.L., B. Miller and L. Rebenfeld, "Forced In-Plane Flow of an Epoxy Resin in Fibrous Networks," *Polym. Eng. Sci.* 26, 1434-1441 (1986).
- Adams, K.L. and L. Rebenfeld, "Permeability Characteristics of Multilayer Fiber Reinforcements. Part I: Experimental Observations," *Polym. Eng. Sci.* 12, 179-185 (1991a).
- Adams, K.L. and L. Rebenfeld, "Permeability Characteristics of Multilayer Fiber Reinforcements. Part II: Theoretical Model," *Polym. Eng. Sci.* 12, 186-190 (1991b).
- Ahn, K.J., J.C. Sefaris and J.C. Berg, "Simultaneous Measurements of Permeability and Capillary Pressure of Thermosetting Matrices in Woven Fabric Reinforcements," *Polym. Compos.*, 12, 146-152 (1991).
- Ambari, A., C. Deslouis and B. Tribollet, "Coil-Stretch Transition of Macromolecules in Laminar Flow Around a Small Cylinder," *Chem. Eng. Commun.* 29, 63-78 (1984).
- Bascom, W.D. and J.B. Romans, "Microvoids in Glass-Resin Composites," I & E C Prod. Res. Dev. 7, 172-178 (1968).
- Beavers, G.S. and D.D. Joseph, "Boundary Conditions at a Naturally Permeable Wall," *J. Fluid Mech.* 30, 197-207 (1967).
- Biller, P., H.C. Öttinger and F. Petruccione, "Consistantly Averaged Hydrodynamic Interaction for Dumbbell Models in Elongational Flow," J. Chem. Phys. 85, 1672-1675 (1986).
- Bird, R.B., W.E. Stewart and E.N. Lightfoot, *Transport Phenomena*, Wiley, NY (1960).
- Bird, R.B., C.F. Curtiss, O. Hassager and R.C. Armstrong, Dynamics of Polymeric Liquids, Volume 2. Kinetic Theory, Wiley, NY (1987).
- Boger, D.V., "A Highly Elastic Constant-Viscosity Fluid," J. Non-Newt. Fluid Mech. 3, 87-91 (1977/1978).

Burdette, S.R., P.J. Coates, R.C. Armstrong and R.A. Brown, "Calculations of Viscoelastic Flow through an Axisymmetric Corrugated Tube Using the Explicitly Elliptic Momentum Equation Formulation (EEME)" J. Non-Newt. Fluid Mech. 33, 1-23 (1989).

Chai, M.S. and Y.I. Yeow, "Modelling of Fluid M1 Using Multiple-Relaxation-Time Constitutive Equations," J. Non-Newt. Fluid Mech. 35, 459-470 (1990).

Chilcott, M.D. and J.M. Rallison, "Creeping Flow of Dilute Polymer Solutions Past Cylinders and Spheres," J. Non-Newt. Fluid Mech. 29, 381-432 (1988).

Chmielewski, C., K.L. Nichols and K. Jayaraman, "A Comparison of the Drag Coefficients of Spheres Translating in Corn-Syrup-Based and Polybutene-Based Boger Fluids," J. Non-Newt. Fluid Mech. 35, 37-49 (1990a).

Chmielewski, C., C.A. Petty and K. Jayaraman, "Crossflow of Elastic Liquids through Arrays of Cylinders," J. Non-Newt. Fluid Mech. 35, 309-325 (1990b).

Chmielewski, C., K. Jayaraman and C.A. Petty, "A Theoretical and Experimental Study of Resin Impregnation into Fiber Bundles Using a Wedge-Slit Die," Presentation at ASC 3rd Tech. Conf., Seattle, Sept. 1988.

Cressely, R. and R. Hocquart, "Biréfringence D'écoulement Localisée Induite à L'arrière D'obstacles," Optica Acta 27, 699-711 (1980).

Christiansen, R.L. and R.B. Bird, "Dilute Solution Rheology: Experimental Results and Finitely Extensible Non-Linear Elastic Dumbbell Theory," J. Non-Newt. Fluid Mech. 3, 161-177 (1977/1978).

Christopher, R.H. and S. Middleman, "Power Law Flow through a Packed Tube," *I&EC Fund.* 4, 422-426 (1965).

Dabir, B., "Mean Velocity Measurements in a 3"-Hydrocyclone using Laser Doppler Anemometry," Ph.D. Dissertation, Dept. of Chem. Eng, Michigan State University (1983).

Darcy, H.P.G., Les fontaines publiques de la villa de Dijon, Victor Dalmont, Paris (1856).

Denn, M.M., Process Fluid Mechanics, Prentice-Hall, NJ (1980).

Dodson, A.G., P. Townsend and K. Walters, "On the Flow of Newtonian and Non-Newtonian Liquids through Corrugated Pipes" *Rheol. Acta* 10, 508-516 (1971).

Durst, F., R. Haas and B.U. Kacmazar, "Flows of Dilute Hydrolyzed Polyacrylamide Solutionis in Porous Media under Various Solvent Conditions," J. Appl. Polym. Sci. 26, 3125-3149 (1981).

Forsythe, G. M. Malcolm and C. Moler, Computer Methods for Matheatical Computations, Prentice-Hall, 1977.

Gere, J.M. and S.P. Timoshenko, *Mechanics of Materials*, PWS Publishers, Boston (1984).

Ghoniem, S.A., "Extensional Flow of Polymer Solutions through Porous Media," *Rheol. Acta* 24, 588-595 (1985).

Gutowski, T.G., Z. Cai, S. Bauer, D. Boucher, J. Kingery and S. Wineman, "Consolidation Experiments for Laminate Composites," *J. Compos. Mater.* 21, 650-669 (1987).

Gutowski, T.G., "A Resin Flow/Fiber Deformation Model for Composites," SAMPE Quarterly 16, 58-64 (1985).

Hudson, N.E., J. Ferguson and P. Mackie, "The Measurement of the Elongational Viscosity of Polymer Solutions Using a Viscometer of Novel Design," *Trans. Soc. Rheol.* 18, 541-562 (1974).

Inverarity, G., "Dynamic Wetting of Glass Fibre and Polymer Fibre," British Polymer J. 1, 245-251 (1969).

James, D.F. and D.R. McLaren, "The Laminar Flow of Dilute Polymer Solutions through Porous Media," J. Fluid Mech. 70, 733-752 (1975).

James, D.F., N. Phan-Thien, M.M.K. Khan, A.N. Beris and S. Pilitsis, "Flow of Test Fluid M1 in Corrugated Tubes" J. Non-Newt. Fluid Mech. 35, 405-412 (1990).

Kulicke, W.M. and R. Haas, "Flow Behavior of Dilute Polyacrylamide Solutions through Porous Media. 1. Influence of Chain Length, Concentration, and Thermodynamic Quality of the Solvent," *Ind. Eng. Chem. Fund.* 23, 308-315 (1984).

Larson, R.E. and J.J.L. Higdon, "Microscopic Flow Near the Surface of Two-Dimensional Porous Media. Part 1. Axial Flow," J. Fluid Mech. 166, 449-472 (1986).

Larson, R.E. and J.J.L. Higdon, "Microscopic Flow Near the Surface of Two-Dimensional Porous Media. Part 2. Transverse Flow," J. Fluid Mech. 178, 119-136 (1987).

- Lawler, J.V., S.J. Muller, R.A. Brown and R.C. Armstrong, "Laser Dopler Velocimetry Measurements of Velocity Fields and Transitions in Viscoelastic Fluids," *J. Non-Newt. Fluid Mech.* 20, 51-92 (1986).
- Lee, W.J., J.C. Sefaris and D.C. Bonner, "Prepreg Processing Science," SAMPE Quarterly 17, 58-68 (1986).
- Lee, W., J. Seferis and L. Bravenec, "Hot Melt Prepreg Processing of Advanced Composites: A Comparison of Methods," SPE ANTEC Tech. Papers 34, 1602-1607 (1988a).
- Lee, W.J., J.C. Seferis and J.C. Berg, "Characterizing High Performance Composite Processability with Dynamic Fiber Wettability Measurements," *Polym. Compos.* 9, 36-41 (1988b).
- Mackay, M.E. and Ch.J.S. Petrie, "Estimates of Apparent Elongational Viscosity Using the Fibre Spinning and "Pure" Methods," *Rheol. Acta.* 28, 281-293 (1989).
- Manero, O. and B. Mena, "On the Slow Flow of Viscoelastic Liquids Past a Circular Cylinder," J. Non-Newt. Fluid Mech. 9, 379-387 (1981).
- Marshall, R.J. and A.B. Metzner, "Flow of Viscoelastic Fluids through Porous Media," Ind. Eng. Chem. Fund. 6, 393-400 (1967).
- McKinley, G.H., W.P. Raiford, R.A. Brown, and R.C. Armstrong, "Nonlinear Dynamics of Viscoelastic Flow in Axisymmetric Abrupt Contractions," *J. Fluid Mech.* 223, 411-456 (1991).
- Mena, B. and B. Caswell, "Slow Flow of an Elastic-Viscous Fluid Past an Immersed Body," Chem. Eng. J. 8, 125-134 (1974).
- Michelsen, M.L., "An Efficient General Purpose Method for the Integration of Stiff Ordinary Differential Equations," AIChE J. 22, 594-597 (1976).
- Middleman, S., Fundamentals of Polymer Processing, McGraw-Hill, NY (1977).
- Müller, A.J., J.A. Odell and J.P. Tatham, "Stagnation-Point Extensional Flow Behavior of M1," J. Non-Newt. Fluid Mech. 35, 231-250 (1990).
- Nguyen, H. and D.V. Boger, "The Kinematics and Stability of Die Entry Flows," J. Non-Newt. Fluid Mech. 5, 353-368 (1979).
- Pilitsis, S. and A.N. Beris, "Calculations of Steady-State Viscoelastic low in an Undulating Tube," J. Non-Newt. Fluid Mech. 31, 231-287 (1989).

Pilitsis, S. and A.N. Beris, "Viscoelastic Flow in an Undulating Tube. Part II. Effects of High Viscoelasticity, Large Amplitude of Undulation and Inertia," J. Non-Newt. Fluid Mech. 39, 375-405 (1991).

Prilutski, G., R.K. Gupta, T. Sridhar and M.E. Ryan, "Model Viscoelastic Liquids," J. Non-Newt. Fluid Mech. 12, 233-241 (1983).

Rallison, J.M. and E.J. Hinch, "Do We Undestand the Physics in the Constitutive Equation?," J. Non-Newt. Fluid Mech. 29, 37-55 (1988).

Richardson, S., "A Model for the Boundary Condition of a Porous Material. Part 2," J. Fluid Mech. 49, 327-336 (1971).

Sadowski, T.J. and R.B. Bird, "Non-Newtonian Flow through Porous Media. I. Theoretical," *Trans. Soc. Rheol.* 9, 243-250 (1965a).

Sadowski, T.J. and R.B. Bird, "Non-Newtonian Flow through Porous Media. II. Experimental," *Trans. Soc. Rheol.* 9, 251-271 (1965b).

Sangani, A.S. and A. Acrivos, "Slow Flow Past Periodic Arrays of Cylinders with Application to Heat Transfer," *Int. J. Multiphase Flow* 3, 193-206 (1982).

Sangani, A.S. and C. Yao, "Transport Processes in Random Arrays of Cylinders. II. Viscous Flow," *Phys. Fluids* 31, 2435-2444 (1988).

Sridhar, T., "An Overview of the Project M1," J. Non-Newt. Fluid Mech. 35, 85-92 (1990).

Sridhar, T., R.K. Gupta, D.V. Boger and R. Binnington, "Steady Spinning of the Oldroyd Fluid B. II: Experimental Results," J. Non-Newt. Fluid Mech. 21, 115-126 (1986).

Taylor, G.I., "A Model for the Boundary Condition of a Porous Material. Part 1," J. Fluid Mech. 49, 319-326 (1971).

Villadsen, J. and M. Michelsen, Solution of Differential Equation Models by Polynomial Approximation, Prentice-Hall, NJ (1978).

Walters, K., "The Second-Normal-Stress Difference Project," *IUPAC MACRO 83*, Plenary and Invited Lectures Part 2, Bucharest, Romainia, 227-237 (1983).

Weaver, F., "Epoxy Adhesive Surface Energies Via the Pendant Drop Method," Tech. Report AFWAL-TR-82-4179, Air Force Wright Aeronautical Laboratories, OH, Dec. 1982.

Yeh, Y. and H.Z. Cummins, "Localized Fluid Flow Measurements with an He-Ne Laser Spectrometer," Appl. Phys. Lett. 4, 176-178 (1964).

MICHIGAN STATE UNIV. LIBRARIES
31293007943412